Ultrafast dynamics in solids

TOPICAL REVIEW

Ultrafast dynamics in solids

K H Bennemann

Institute for Theoretical Physics, Freie Universität Berlin, Arnimallee 14, D-14195 Berlin, Germany

E-mail: khb@physik.fu-berlin.de

Abstract
The ultrafast response of metals and semiconductors to electronic excitations
is analysed. Time resolved two-photon emission and non-linear optics allow
us to study the relaxation of systems at non-equilibrium. Representative results
for the spin dependent relaxation of excited electrons in transition metals, in
ferromagnetic metals such as Ni, Co, Fe and in high T_c superconductors are
given. Also ultrafast dynamics of semiconductors such as Si, Ge and C is
analysed. In particular, in covalently bonded solids, electronic excitations
from the valence to the conduction band cause a change of the bond character
and thus strong changes of various properties and induce coherent phonons,
ablation, ultrafast melting and phase transitions at non-equilibrium. The
ultrafast relaxation processes are controlled by energy and angular momentum
conservation, of course, and this is particularly important for magnetism at non-
equilibrium. The time dependence of the magnetic relaxation in nanostructures
reflects in a characteristic way the atomic structure. The ultrafast Coulomb
explosion of clusters in intense electric fields may serve as a demonstration of
non-equilibrium dynamics resulting from electric field induced solid–plasma
transition. Dynamics in small clusters can test the validity of concepts used in
thermodynamics. Optically controlled electronic population dynamics may be
expected to be relevant for ultrafast switching devices and recording.

(Some figures in this article are in colour only in the electronic version)

Contents

1. Introduction

The study of non-equilibrium physics is fundamentally important and may also offer many new technological applications. The timescales of physical processes in systems at non-equilibrium are of central interest. In general, excited electrons relax very quickly to equilibrium states. In solids [1], metals and covalently bonded systems such as Si, Ge, C [2–4], the excited electrons establish due to their interactions within a time ranging from about 10 to 100 fs or more a temperature $T_e(t)$ which is larger than the lattice temperature $T_{latt}(t)$. Then, $T_e(t)$ approaches again the lattice temperature, $T_e \to_t T_{latt}$, and this might last up to a few picoseconds. The thermalization of excited electrons and lattice atomic structure, typically in a few picoseconds, results from electron–phonon coupling. This quite general scenario is illustrated in figure 1 [1].

Clearly, time resolved analysis of fundamental physical processes is promising as regards a better understanding of non-equilibrium transport, relaxation, magnetization changes, bond formation and ultrafast switches, for example. In ferromagnetic metals such as Ni, Co and Fe with Curie temperature T_C, one expects the exchange interaction and the magnetization M to respond to the non-equilibrium distribution of electrons and to the increase of temperature $T_e(t)$. Thus,

$$M = M\{T_e(t), t, \ldots\} \underset{t}{\to} 0, \qquad T_e \to T_c, \tag{1}$$

during a time controlled by the interactions achieving angular momentum conservation. Here, frequently spin–orbit coupling may play the key role.

In figure 2, the response of the magnetization to $T_e(t)$ is illustrated [1, 5]. Photons excite s and d electrons into states above the Fermi energy ϵ_F. No spin flips occur. Since states are s–d hybridized, electric dipole selection rules have to include this. Using the Hubbard Hamiltonian for the dynamics of the itinerant electrons, the magnetism responds due to the interplay of the hopping integral t_{ij}, the intra-atomic Coulomb interaction U and the exchange coupling $J < U$. Note that, for given photon energy $\hbar\omega$, one gets different numbers of spin up and down hot electrons due to difference between the initial DOS $N_\sigma(\epsilon)$. Furthermore, the electron distribution $\{n_\sigma(\omega) + n_{-\sigma}(\omega)\}$ might change over time somewhat faster than $\{n_\sigma(\omega) - n_{-\sigma}(\omega)\}$. Note that circularly polarized light excites electrons out of the Fermi sea spin selectively.
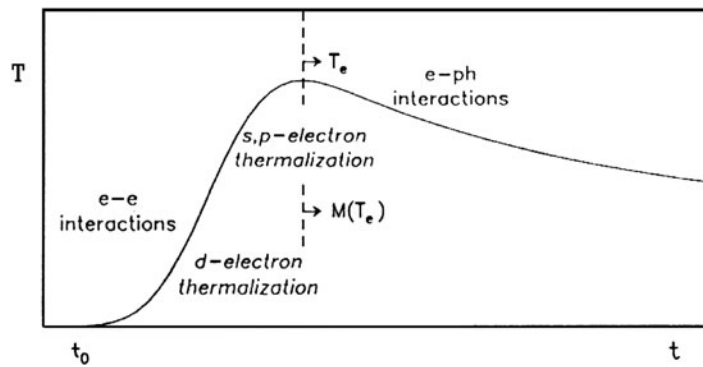
Figure 1. An illustration of the electron dynamics of hot electrons; t_0 is the time when excitation and subsequent relaxation and thermalization of excited electrons begins. The time dependence of the electron temperature T_e is controlled by electron–electron and electron–lattice interactions. First d and then s electrons thermalize. The maximal temperature T_e^{max} reflects the interplay of the energy distribution over the progressively thermalizing electrons and energy transfer of the lattice.
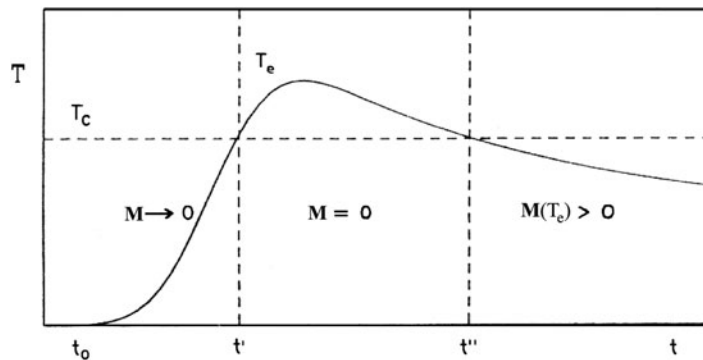
Figure 2. An illustration of the time dependent magnetization, $M(t)$, due to hot electrons. $M(t)$ responds to $T_e(t)$. The resultant fast spin dynamics occurs such that angular momentum is conserved. The above scenario is expected for ferromagnetic (antiferromagnetic) metals, for example. For times between t' and t'', the excited warm electrons lose their spin order and then $M(T_e(t)) \to 0$. T_c is the spin ordering temperature.

In figure 3, we illustrate optically induced excitations in ferromagnetic metals such as Ni and Fe.

Of particular interest are bond changes resulting from electronic excitations. For example, excitations

$$s^2p^2 \xrightarrow{t} sp^3, \qquad sp^3 \xrightarrow{t} s^2p^2 \tag{2}$$

as expected in C, Si, Ge, GeAs etc cause ultrafast structural changes [2–4]. This might be of interest for non-thermal ultrafast lattice changes and subsequent melting accompanied by a metallic phase. Also the transition

$$\text{crystalline} \rightleftarrows \text{amorphous}$$
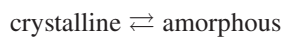
and the transition

$$\text{graphite} \rightleftarrows \text{diamond}$$
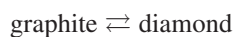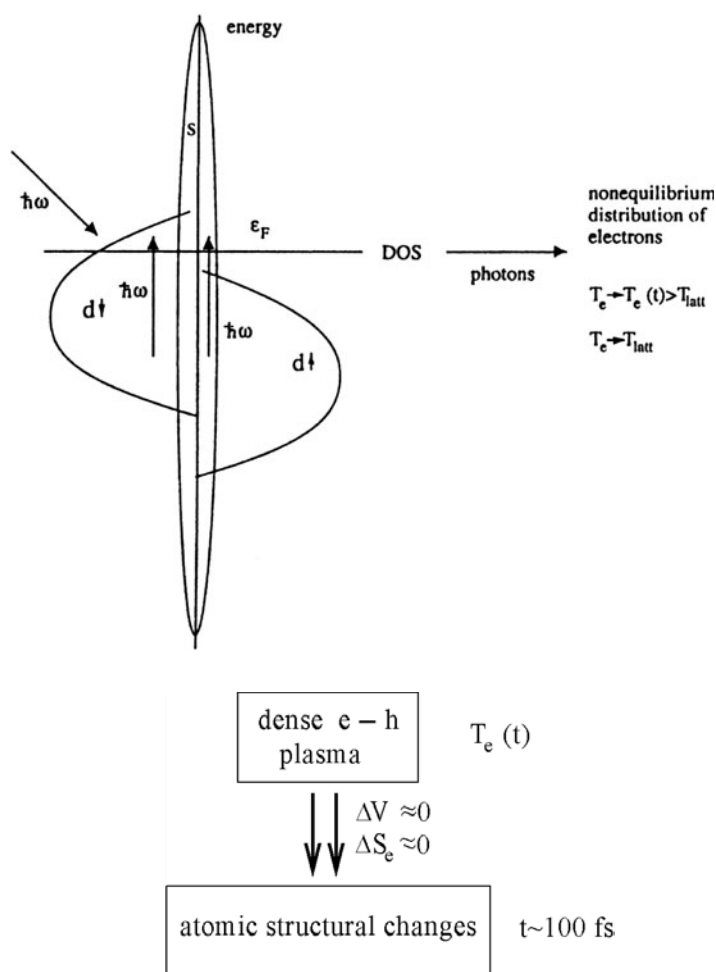
Figure 3. A schematic illustration of electronic excitations in ferromagnetic Ni including mainly spin polarized d states. Note that the density of states (DOS) might change due to the excitations.
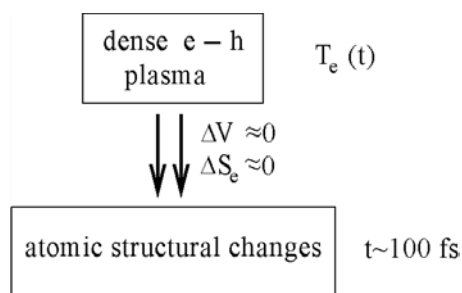
Figure 4. In contrast to thermal melting at T_m occurring during times of the order of ps, a dense e–hole plasma due to many optically induced electronic excitations from the valence band with sp^3 type orbitals to the conduction band with s, p states causes an ultrafast structural change and melting within 100 fs or a few hundred femtoseconds. This is typically characterized by no volume changes ($\Delta V \approx 0$) and by a constant entropy of the e–h plasma ($\Delta S_e \approx 0$).

at non-equilibrium are of utmost interest [1]. Note that the transition crystal $\rightleftarrows$ amorphous may involve the excitation of a special lattice excitation and will require a special shape of the exciting laser pulse. The transition graphite $\rightleftarrows$ covalent crystal involves change of the bond character. Non-thermal ultrafast melting is illustrated in figure 4 [2, 3].

In sp^3 bonded covalent crystals many excitations decrease the gap Δ between the valence and conduction band. Then, for $\Delta \rightarrow 0$ one expects metallicity.

In superconductors, electronic excitations involve the breaking up of Cooper pairs and subsequent recombination. Photon absorption may also involve additional excitations due to antiferromagnetism and structural changes. This sheds light on the Cooper pairing mechanism and is of particular interest as regards superconductivity in high T_c cuprates, heavy fermion metals and magnetic compounds such as UGe_2.

In figure 5 we illustrate the dynamics expected in superconductors [6]. For example, phase fluctuations of Cooper pairs are reflected by frequency (ω) dependent measurements of
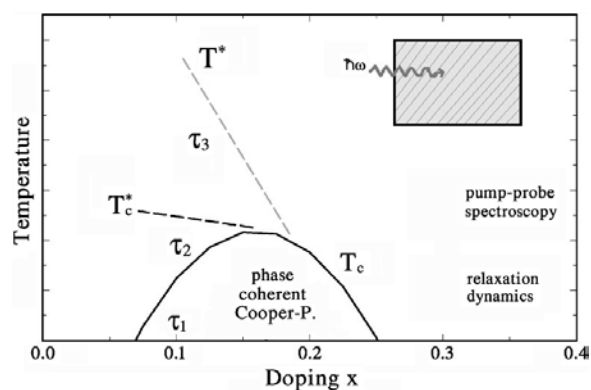
Figure 5. An illustration of fast electron dynamics (fs → ps) in superconductors. Excitations result from photon absorption. The phase diagram relates to high T_c cuprates involving different timescales τ_1, τ_2 and τ_3 for characteristic processes reflecting Cooper pair dynamics, antiferromagnetism and a pseudogap. At T^* a pseudogap and at T_c^* phase incoherent Cooper pairing appear.
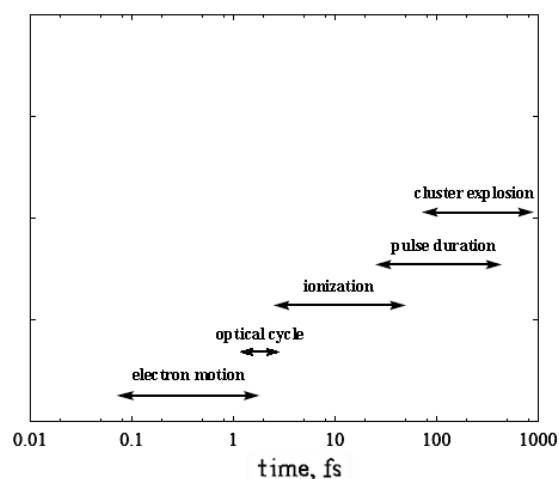
Figure 6. An illustration of various characteristic times involved during cluster Coulomb explosion. The intense electric field creates first, within femtoseconds, a dense gas of hot electrons. These then transfer the absorbed energy very quickly to the ionized cluster atoms.

the Meissner effect: for times $t \lesssim \omega_{fl}^{-1}$, where ω_{fl} denotes the mean fluctuation frequency, one expects behaviour as for phase coherent Cooper pairs ($t \sim \omega^{-1}$).

The optically induced transition from solids at equilibrium to a dense plasma with many hot electrons, thermalizing rapidly within femtoseconds, and a warm lattice ($T_{latt}(t) \ll T_e(t)$) is of quite general interest. In particular, the ultrafast Coulomb explosion of clusters involving ions with unusually large ionic charges is remarkable [1, 8]. Clusters are also suited for studying dimensional effects in non-equilibrium behaviour and behaviour of matter in very strong electric fields.

As illustrated in figure 6, one expects for clusters, on general grounds, that the light energy is first absorbed by electrons. This causes ultrafast (in times of the order of femtoseconds) creation of a very hot electron gas maintained for some time by the ions whose kinetic energy increases rapidly due to fast energy transfer from the hot electrons to the ions. Of course, some hot electrons get emitted, but the remaining ones will be able to screen, for some time, the ions—best, those at the centre of the cluster. The continuing increase of the kinetic energy

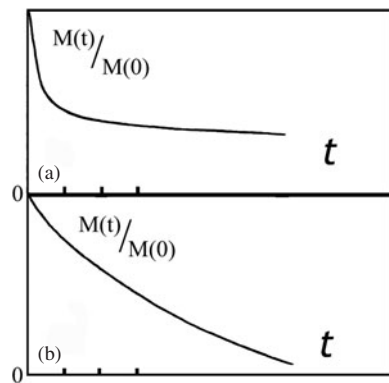**Figure 7.** Typical slow long time relaxation behaviour of the magnetization in nanostructures, as an example, after an external magnetic field is turned off. One expects the relaxation times to reflect characteristically the atomic structure and the magnetic interactions, of course. We illustrate the behaviour of a film consisting of (a) magnetic islands which couple strongly and (b) nearly isolated islands whose relaxation is mainly controlled by the magnetic anisotropy and for which, thus, $M(t) \rightarrow_t 0$ at equilibrium.

of the ions and the reduced screening at the cluster surface will cause emission of those ions whose repulsive Coulomb energy overcomes the binding. One expects the spectrum of the ionic charges to be very revealing as regards the physics behind the Coulomb explosion of clusters. The scenario for matter in strong electric fields is summarized in figure 6. The hot electrons transfer their energy very quickly to the ions. The ions continuously gain more kinetic energy and positive charge. At about 100 fs, increasingly more ions get emitted when their Coulomb repulsion (E_b) overcomes the binding E_b ($E_C > E_b$). This occurs first at the cluster surface. Such a scenario is expected in general for matter in strong electric fields. Electronic relaxation processes may be accompanied by light emission bursts.

For nanostructures, the dependence of the magnetic relaxation on the atomic structure is of basic interest and also of interest as regards magnetic recording [7]; see figure 7 for an illustration. Thin nanostructured magnetic films exhibit different relaxations depending on the coupling between the magnetic islands in the film and the geometrical pattern of the atomic structure.

Of particular interest are relaxation phenomena due to hot electrons in optically excited nanostructures. Then, much faster spin relaxation might occur and probably also fast switching between high and low spin states, magnetization reversal etc. Switching between high spin and low spin states induced optically or by other perturbation offers interesting perspectives for applications.

Optical manipulation of multiple-film systems, where the exchange coupling between the films is changed upon electronic excitations, seems very interesting. For example, the magnetic structure $\uparrow\downarrow\uparrow\downarrow \cdots$ of layered films may change in the presence of hot electrons. These may also affect the magnetization reversal and hysteresis in external magnetic fields. Hot electrons also change the magnetic reorientation transition at surfaces of transition metals etc. Since the exchange interaction J depends on the atomic interlayer distance d, $J = J(d)$ and $d = d(T_e(t))$, one expects at the surface corresponding and characteristic changes of the magnetization ($M = M\{J(d), \ldots\}, d = d\{T_e(t)\}$).

Another interesting physical arrangement consists of tunnel junctions with quantum dots or molecules as the tunnel medium. Here the tunnelling may be blocked by excited electrons. Excitations and subsequent relaxation will yield ultrafast pulsating tunnel currents.
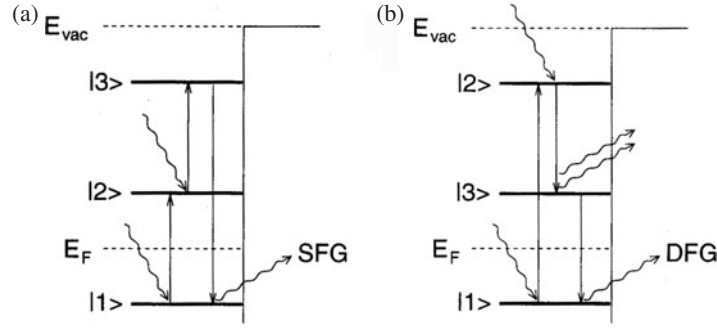
Figure 8. An illustration of the non-linear optics. Simplified representations of (a) sum frequency generation (SFG), where two photons of frequencies ω_1 and ω_2 are absorbed by electrons in states $|1\rangle$ and $|2\rangle$ and a single photon of frequency $\omega_1 + \omega_2$ is emitted, and (b) difference frequency generation (DFG), due to induced emission of a photon with frequency $|\omega_1 - \omega_2|$. The two photons may be provided by one or two laser pulses. E_F is the Fermi energy and E_{vac} is the vacuum energy.

These are some typical examples of non-equilibrium physics and time resolved processes. Pump and probe spectroscopy features such as two-photon photoemission (2PPE), non-linear optics (SHG—second-harmonic generation) and magneto-optics (the Kerr effect) constitute successful tools for studying time resolved behaviour; see the illustration in figure 8 [1, 9]. In particular, the non-linear optical response reflects sensitively symmetry changes and thus structural changes and phase transitions [10]. Note that 2PPE and SHG are intimately related processes. Using polarized light, circularly polarized light in particular, one may excite electrons spin selectively.

In the next section we present the basic theory for time resolved studies and present in section 3 characteristic results for various processes. In section 4 we summarize the analysis and discuss some interesting open problems.

2. Theory

2.1. Electronic excitations

To calculate the non-equilibrium state, one may use non-equilibrium Green functions $\mathcal{G}_\sigma(x, x')$, Keldysh or Baym–Kadanoff type ones, and determine thus the electronic energy spectrum $\epsilon_{i\sigma}\{n_{l\sigma}(t), \ldots\}$ of the states $|i\sigma\rangle$. The occupation numbers

$$n_i\{\ldots, t\} \tag{3}$$

characterize the non-equilibrium state and depend on time. Then, the free energy functional $F\{n_{i\sigma}(t), \ldots\}$ determines the non-equilibrium properties. Frequently one may use this to simplify the analysis:

$$n_{i\sigma}(t) = \int d\epsilon \, N_{i\sigma}(\epsilon, t) \, f_\sigma(\epsilon, t), \tag{4}$$

where $N_{i\sigma}(\epsilon, t)$ is the local density of states at site i and for spins σ and $f_\sigma(\epsilon, t)$ the Fermi distribution function for the electrons. The ansatz [9]

$$f_\sigma = f_\sigma^0 + \delta f_\sigma(\epsilon, t) \tag{5}$$

yields approximately ($\delta f \ll f^0$)

$$\delta f_\sigma(\epsilon, t) \simeq \delta f_\sigma(\epsilon, 0) e^{-t/\tau_\sigma}. \tag{6}$$

Here, f_σ^0 relates to equilibrium and $\tau_\sigma(\epsilon_i)$ is the lifetime of the excited electron in state $\epsilon_{i\sigma}$. Using many-body theory, this lifetime is calculated from the electron self-energy $\sum_\sigma(\omega, t)$.

For excitations not too far away from the Fermi energy ϵ_F one gets within Fermi liquid theory

$$\tau_{\mathbf{k}\sigma} = \tau_{k\sigma}^0 \epsilon_F/(\epsilon_{k\sigma} - \epsilon_F)^2 \tag{7}$$

with

$$\tau^0 \simeq (64/\pi^2\sqrt{3\pi})\sqrt{\frac{m}{e^2 n}} \tag{8}$$

$(\tau^0 \approx 128/\sqrt{3}\pi^2\omega_p)$. Here, n is the number of electrons per atom and ω_p the plasmon frequency. In accordance with Fermi's golden rule one may also use the expression $(\epsilon \sim \epsilon_F)$

$$\tau_{k\sigma} \sim 1/N_\sigma(\epsilon). \tag{9}$$

Note that the lifetimes are generally wavevector ($\mathbf{k}$) dependent and are expected to be smaller for electrons in bands with large densities of states. For transition metals for example one expects lifetimes as short as femtoseconds. In ferromagnetic metals the lifetimes are also spin dependent.

In the case of very strong interactions amongst the electrons, like in cuprates or heavy fermions, non-Fermi liquid behaviour might be present. Then, $\tau^{-1} \sim \text{Im} \sum_\sigma(\omega) \sim \omega$ and consequently [6]

$$\tau_{\mathbf{k}\sigma}(\omega) \sim \omega^{-1}. \tag{10}$$

2.2. Thermalization of a dense hot electron system

Clearly, one expects the excited electrons to establish very quickly—within a time of the order of $t \propto U^{-1}$—a temperature $T_e(t)$, due to the Coulomb interactions U. Note that the system of hot electrons is not at equilibrium with the lattice atoms and $T_e(t) > T_{latt}(t)$. First, $T_e(t)$ increases with time and then decreases again due to electron–phonon coupling and $T_e(t) \to T_{latt}(t)$ for longer times, of the order of picoseconds. The key quantity $T_e(t)$ for the non-equilibrium behaviour may be determined using the master equation. Thus, one gets approximately [5, 11]

$$c_e(T_e)\frac{\partial T_e}{\partial t} = -g_{e-ph}(T_e - T_{latt}) + \frac{\partial}{\partial t}\int d\epsilon \, \epsilon \, N(\epsilon)\delta f + P(t) + \cdots \tag{11}$$

and

$$c_{latt}(t)\frac{\partial T_{latt}}{\partial t} = -g_{e-ph}(T_{latt} - T_e) + \cdots. \tag{12}$$

Here, $c_e = \partial E/\partial T$ is the electronic specific heat for the non-equilibrium state, c_{latt} the corresponding lattice specific heat and $P(t)$ describes the exciting laser pulse including its polarization. At times $t \leqslant t_0$ before the laser induced excitations of electrons, one assumes $T_e = T_{latt} = T_0$. Equations (11) and (12) give results which are illustrated in figure 1 [5].

Note that the energy transfer from the hot electrons to the colder lattice is controlled by the electron–lattice coupling g_{e-ph} and occurs during a time $t \leqslant E_{e-latt}^{-1} \sim g_{e-ph}$ ($t \sim$ ps). E_{e-latt} is the coupling energy. The thermalization of the hot electrons might spread in time, since s, p, d, f electrons experience different interactions.

2.3. Spins at non-equilibrium

The thermalization of electron spins and magnetic moments μ_i occurs during a time of the order of

$$t \sim \frac{1}{zJ\mu^2} \sim T_{\mathrm{C}}^{-1}, \tag{13}$$

if angular momentum can be transferred (via spin–orbit coupling, for example) during this time. Here, J is the exchange interaction, μ the magnitude of the magnetic moments, z the number of nearest neighbour magnetic moments and T_{C} the Curie temperature. In general, $M\{T_{\mathrm{e}}(t)\} \to 0$ due to hot electrons and $T_{\mathrm{e}} > T_{\mathrm{C}}$ during times $t \gtrsim t_{\mathrm{c}}$, where t_{c} is the time needed to achieve angular momentum conservation. Note that magneto-optics (Kerr effect, hysteresis loops etc) is expected to reflect $M(t) \to 0$ sensitively, due to hot electrons.

In the case of itinerant electrons one may use the master or Liouville equation for the spin density operator ρ_σ and thus

$$\frac{\mathrm{d}}{\mathrm{d}t}\rho_\sigma = \frac{1}{\mathrm{i}\hbar}[H, \rho_\sigma] + R\{\rho_\sigma\}. \tag{14}$$

This equation may be used to calculate the change of magnetization at non-equilibrium. Here, H is the (Hubbard) Hamiltonian and the functional $R\{\rho_\sigma\}$ is a formal representation of relaxation mechanisms (due to spin–orbit scattering, for example). From equation (14), or from Green function theory, one determines

$$M(t) \sim \sum_k \{n_{k\uparrow}(t) - n_{k\downarrow}(t)\} \tag{15}$$

(k = the sum over all band states $|k\sigma\rangle$). One may use for example the Hubbard Hamiltonian to calculate $n_{k\sigma}$. For metals one gets typically due to hot electrons an increase of T_{e} during a time of the order of 10–100 fs or more and, due to the increase of the electronic temperature, possibly $M \to 0$. The latter is controlled by angular momentum conservation. Consequently, $M \to 0$ may require a time of the order of $t \sim V_{\mathrm{so}}^{-1}$, if spin–orbit coupling controls the angular momentum transfer. Here, V_{so} is the spin–orbit coupling energy. As a consequence it might happen that the response of $M\{T_{\mathrm{e}}(t), t\}$ to hot electrons (to $T_{\mathrm{e}}(t)$) is time delayed and slower. If sufficient time for angular momentum transfer is given, then approximately

$$M(t) \simeq M(T_{\mathrm{e}}(t), \ldots).$$

For an ensemble of local spins described by the Heisenberg Hamiltonian one may calculate at non-equilibrium, in addition to $T_{\mathrm{e}}(t)$ relating to the itinerant electrons (conduction electrons) and $T_{\mathrm{latt}}(t)$, a spin temperature $T_{\mathrm{s}}(t)$ from the master equation

$$c_{\mathrm{s}}\frac{\partial T_{\mathrm{s}}}{\partial t} = -g_{\mathrm{s-e}}(T_{\mathrm{s}} - T_{\mathrm{e}}) - g_{\mathrm{s-latt}}(T_{\mathrm{s}} - T_{\mathrm{latt}}) + \cdots. \tag{16}$$

Here, c_{s} is the specific heat of the spins and $g_{\mathrm{s-e}}$ and $g_{\mathrm{s-latt}}$ are coupling constants [12]. (Note that treating electrons, spins and the lattice as separate systems adds to equation (11) the term $\{-g_{\mathrm{e-s}}(T_{\mathrm{e}} - T_{\mathrm{s}})\}$ and to equation (12) the term $\{-g_{\mathrm{s-latt}}(T_{\mathrm{latt}} - T_{\mathrm{s}})\}$.)

The change of the magnetization due to hot electrons and $T_{\mathrm{s}}(t)$ is calculated from

$$\frac{\mathrm{d}\boldsymbol{S}_i}{\mathrm{d}t} = -\frac{2J(t)}{\hbar}\sum_{j\neq i}(\boldsymbol{S}_i \times \boldsymbol{S}_j) + \boldsymbol{R}, \tag{17}$$

where j relates to nn spins of spin i and $\boldsymbol{R}$ to relaxation processes due to the spin–orbit coupling, for example. Thus, the magnetization at non-equilibrium ($\langle S_z \rangle = M$) at time t is given approximately by

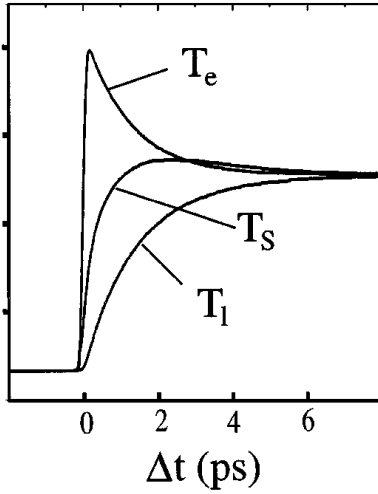$$M(t) \simeq M(T_{\mathrm{s}}(t)). \tag{18}$$

Figure 9. An illustration of the characteristic temperatures for a system of spins (T_s), itinerant electrons (T_e) and a lattice (T_l).

Note that the exchange coupling $J(T_e, \ldots)$ might change at non-equilibrium, as well as the magnitude of the spins S_i. The behaviour of $T_e(t)$, $T_s(t)$ and $T_{latt}(t)$ is schematically indicated in figure 9 [12].

Layered and covalently bonded solids at non-equilibrium are of particular interest, since electronic excitations involving bond changes

$$\text{sp}^3 \underset{t}{\to} \text{s, p} \tag{19}$$

are accompanied by dramatic changes of physical properties [2, 4]. This can be seen from the response of covalent solids such as Si, Ge, C, diamond, GaAs to laser irradiation. The excited electrons (hot electron–hole plasma) resulting from transitions from the valence to the conduction band cause a fast change of lattice symmetry and subsequent melting within 100–500 fs and cause also drastically changed optical properties (luminescence, absorption etc).

In Si and Ge, for example, intense laser light causes many $\text{sp}^3 \to \text{s, p}$ transitions. The resulting dense gas of hot electrons thermalizes quickly, within femtoseconds. Then, these hot electrons have a temperature $T_e(t)$ and are not at equilibrium with the lattice ($T_e > T_{latt}$). Only after times of the order of a few picoseconds are both systems at equilibrium again ($T_e \to T_{latt}$ for times $t \gtrsim 2$ ps). At shorter times the hot electrons will not significantly exchange heat (Q) with the lattice (atoms). Hence, this state is approximately characterized by (see figure 4)

$$\Delta Q \sim \Delta S_e \simeq 0, \qquad \Delta V \simeq 0 \tag{20}$$

and $\Delta U_e + \Delta W \simeq 0$ [2, 3]. Here, S_e is the electronic entropy, V to the volume of the system (solid), ΔU_e to the change of the internal electronic energy and ΔW to the work executed on the lattice atoms. The pressure resulting from the hot electrons occupying the s, p states of the conduction band will induce fast lattice distortions. In accordance with $\Delta V \simeq 0$ these will be dominantly transverse acoustic (TA) and longitudinal optical (LO) phonon like.

One expects that for such a non-equilibrium state the open diamond structure will become more compact and GaAs more centrosymmetric, for example. The band gap Δ_b between the conduction and valence band decreases due to the hot electrons. For $\Delta_b \to 0$ one gets metallic properties. This scenario occurs during a time of the order of 50–500 fs due to the fast electronic processes and the interatomic interactions.

This physical picture applies also to the laser induced ablation of semiconductors, the transitions diamond $\to$ graphite ($\text{sp}^3 \to \text{s}^2\text{p}^2$), crystal $\rightleftarrows$ Peierls distortion,

amorphous $\rightleftarrows$ crystalline, layered graphite $\rightarrow$ liquid state and the possible transition $C_n \rightarrow$ diamond at non-equilibrium. Note that these transitions and their speed may be somewhat controlled by choosing an optimal shape (duration, polarization etc) of the exciting laser pulse.

For a quantitative analysis with the most important control parameters electronic entropy $S_e(T_e)$ and electron temperature T_e, or equivalently the fraction ξ of hot electrons in the conduction band ($T_e \leftrightarrow \xi$), we use the binding energy

$$E_b(\boldsymbol{R}, T_e) = \int d\epsilon \, \epsilon \, N(\epsilon, T_e) f(\epsilon, T_e) + E_r. \tag{21}$$

Here, $\boldsymbol{R}(\xi) = \boldsymbol{R}_0(0) + \delta \boldsymbol{R}(\xi)$ (the atomic positions) and E_r relate to the (repulsive Born–Mayer type) atomic interactions. The density of states $N(\epsilon, T_e)$ may be determined using a tight-binding Hamiltonian, for example. $f(\epsilon, T_e)$ denotes the non-equilibrium Fermi distribution function and is approximately given by determining the chemical potential $\mu(T_e)$ from

$$\int d\epsilon \, N(\epsilon) f(\epsilon) = z_v, \tag{22}$$

with z_v being the number of valence electrons per atom, and the electronic temperature $T_e(t)$ from

$$S_e\{T_e\} = \text{constant} \tag{23}$$

($S_e \simeq k \int d\epsilon \, N(\epsilon)[f \ln f + \cdots]$) or from

$$\xi = \frac{1}{z_v} \int_{vb} d\epsilon \, N(\epsilon)(1 - f(\epsilon)). \tag{24}$$

Describing the induced distortions (for simplicity) by

$$\boldsymbol{R}(\xi) = R_0(0) + \delta_{LO} e_L + \delta_{TA} e_T \tag{25}$$

(e_L, e_T are unit vectors relating to longitudinal and transverse distortions for example), the dynamics of these distortions are (approximately) determined by [2, 3]

$$M\ddot{\delta}_i = -\frac{\partial}{\partial \delta_i} E_b(\delta_i, T_e) \tag{26}$$

($i = $ LO, TA). The induced lattice dynamics occurs during times of the order of $t \propto d_0^2 \sqrt{M}$, where d_0 is the average bond length. Note that equation (26) may also be used to make calculations for coherent phonons induced by hot electrons.

Using this theory, the transition from the semiconducting to the metallic phase is given by

$$\Delta_b(\delta_{TA}, \delta_{LO}, T_e) = 0. \tag{27}$$

Figure 10 shows the behaviour of E_b at non-equilibrium. The shift of the minimum in E_b from $\delta = 0$ to a finite value of δ signals a change of the lattice structure.

This completes then a simplified theory for covalent semiconductors at non-equilibrium. It applies also to other systems with a gap such as ionic crystals, Peierls distorted lattices and clusters such as Hg_n with an s–p gap. At surfaces, the theory will describe intense emission of atoms upon laser irradiation (ablation).

The theory needs to be extended to allow for volume changes (see for example graphitization of diamond with $\Delta V \neq 0$), to include relaxation of the excited electrons and to describe the response to laser pulses which last for some time and during which, for example, the volume (atomic density) is changing [1–4]. The basic physics described by the theory is illustrated in figure 11. We use the potential energy surface (PES) for a characterization. Note that for a laser pulse with finite duration time the properties of the system will change during irradiation. Then in particular the structural changes occurring affect the absorptivity in a time
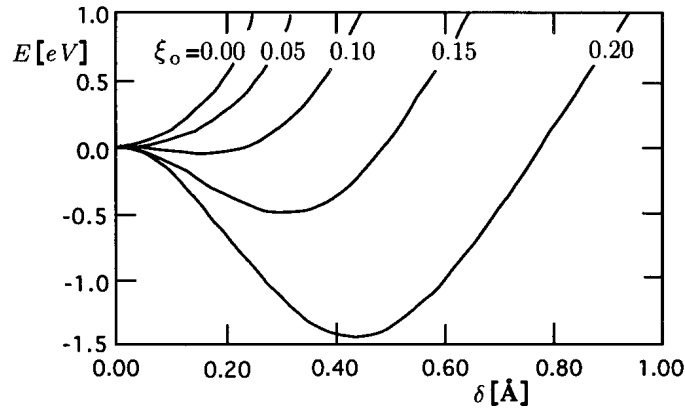
Figure 10. The dependence of the binding energy E_b for Si on the fraction ξ_0 of excited valence electrons and average atomic displacement δ. This illustrates the response of the atomic structure to electronic excitations. ($\xi_0 = \xi(\delta = 0)$.) The minima at $\delta > 0$ indicate a changed structure.
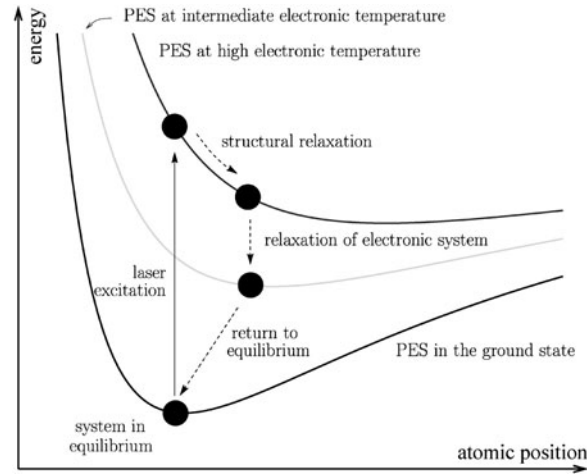

Figure 11. An illustration of the potential energy surface (PES) including relaxation after optical excitation of a covalent solid. The different relaxation processes occur simultaneously, yet on different timescales. Note that strong excitations often lead to structural changes, so no return to the initial equilibrium structure may occur.

dependent fashion, for example [13]. This will be important for the behaviour of systems in strong laser fields.

For the extension of the theory, we employ molecular dynamics (MD) analysis to determine the atomic structure and take the electronic degrees of freedom into account [1, 4]. Hence we use the Hamiltonian

$$H = H_e + \sum_{i<j} V(r_{ij}). \tag{28}$$

atomic positions
$$\{\mathbf{r}_k(t)\}$$

Hamiltonian $\xrightarrow{\text{diagonalization}}$ energy spectrum
$$H(\{r_{ij}(t)\}) \qquad\qquad \{\epsilon_m(\{r_{ij}(t)\})\}$$

new cycle
for time $\Phi(\{r_{ij}(t)\}, \{n(\epsilon_m, t)\})$ potential
$t + \Delta t$ energy
surface

$$\{\mathbf{r}_k(t + \Delta t)\} \xleftarrow[\textbf{dynamics}]{\textbf{molecular}} \{\mathbf{f}_k(\{r_{ij}(t)\}, t)\}$$
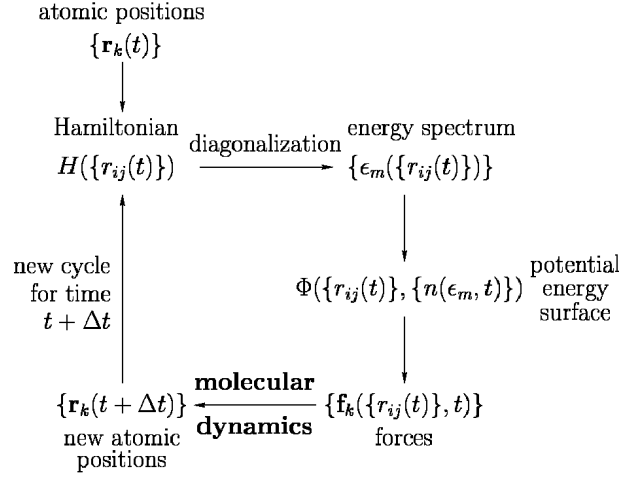new atomic   forces
positions

Figure 12. The molecular dynamics calculational scheme for the determination of changes of the atomic structure in response to electronic excitation. An explicitly time dependent PES is obtained on the basis of an electronic Hamiltonian and with the help of a time dependent non-equilibrium electronic occupation. This PES yields forces for the molecular dynamics. Then, these are used to determine the relaxation of the atomic structure.

Here, the potential V describes the repulsive interaction between the ion cores and H_e the behaviour of the electrons. Using a tight-binding Hamiltonian, one has ($H_e = H_{TB}$)

$$H_e = \sum_{i\alpha} \epsilon_{i\alpha}^0 n_{i\alpha} + \sum t_{ij}^{\alpha\beta} c_{i\alpha}^+ c_{j\beta} + \cdots, \tag{29}$$

with on-site energies $\epsilon_{i\alpha}^0$ and occupations $n_{i\alpha}$ at a site i and for electronic states $|\alpha\rangle$. The hopping integrals $t_{ij}^{\alpha\beta}$ are distance dependent. The creation ($c_{i\alpha}^\dagger$) and annihilation ($c_{j\beta}$) operators are given as usual.

From this Hamiltonian, one calculates using molecular dynamics the electron occupation numbers $n_{i\alpha}(t)$ at non-equilibrium and the time dependent PES. This is illustrated in figure 12. For details, see Jeschke, for example [1, 4, 13]. The PES is given by

$$\Phi(\{r_{ij}(t)\}, t) = \sum_{i,\alpha} \epsilon_{i\alpha} n_{i\alpha}(t) + \frac{1}{2} \sum_{\substack{i,j \\ (i \neq j)}} V(r_{ij}). \tag{30}$$

Here, $\epsilon_i(\{r_{ij}(t)\}) = \langle i|H_e|i\rangle$.

The adiabatic principle for the electron–atom system justifies using for the atoms the Lagrangian

$$L = \sum_i \frac{m_i}{2} \dot{r}_i^T \dot{r}_i - \Phi(\{r_{ij}\}, t), \tag{31}$$

where T means transposition. One gets then the equations of motion for the atoms from the Euler–Lagrange equations

$$\frac{d}{dt} \frac{\partial L}{\partial \dot{r}_k} = \frac{\partial L}{\partial r_k} \qquad (k = 1, \ldots, N). \tag{32}$$

Thus,

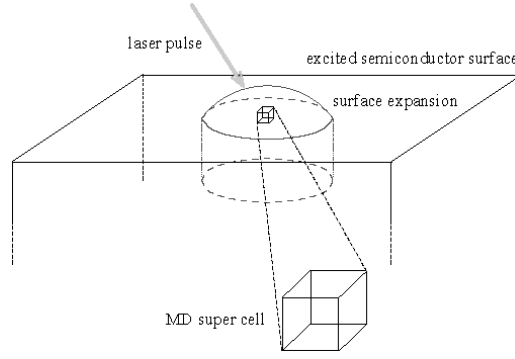$$m_k \ddot{r}_k = -\frac{\partial \Phi}{\partial r_k}. \tag{33}$$

Figure 13. Modelling of part of a bulk solid with a small MD supercell. The laser excited surface region expands into the vacuum and thus shape and size changes are permitted for the MD supercell. The cell has periodic boundary conditions in all directions, simulating a small region of translational invariance.

Note that the Lagrangian contains the effects of the electrons via the many-body potential Φ. The forces $f_k = -\nabla_k \, \Phi(\{r_{kl}\}, t)$ acting on the atoms are calculated using the Hellmann–Feynman theorem. Thus,

$$f_k(\{r_{ij}(t)\}, t) = -\sum_m n(\epsilon_m, t)\langle m|\nabla_k H_{\text{TB}}|m\rangle - \tfrac{1}{2}\sum_{\substack{i,j \\ (i\neq j)}} \nabla_k V(r_{ij}), \qquad (34)$$

where m relates to states characterized before by i, α and H_{TB} is the tight-binding approximation for H_{e}.

Using the Verlet algorithm, one may calculate $r(t + \tau)$ from $r(t)$ and $\dot{r}(t + \tau)$ from $\dot{r}(t)$. The dynamics of the system is given by the time dependence of the occupation $n(\epsilon_m, t)$ [1, 4, 13]. These may be determined from Keldysh type Green functions or from a Liouville–von Neumann equation for the density matrix [14] or from a Boltzmann type approach [9]. Approximately, one has at each time step Δt of a MD calculation (for details see [1])

$$\frac{\mathrm{d}n(\epsilon_m, t)}{\mathrm{d}t} = \int_{-\infty}^{\infty} \mathrm{d}\omega \, P(\omega, t - \Delta t) \, \{[n(\epsilon_m - \hbar\omega, t - \Delta t) - n(\epsilon_m, t - \Delta t)]$$

$$- [n(\epsilon_m, t - \Delta t) - n(\epsilon_m + \hbar\omega, t - \Delta t)]\} - \frac{n(\epsilon_m, t) - n^0(\epsilon_m)}{\tau_{\text{e}}}. \qquad (35)$$

Here, n^0 is the equilibrium Fermi–Dirac distribution and τ_{e} the electron thermalization time. $P(\omega, t)$ is the laser pulse intensity function. It may also absorb the transition matrix element for transitions $\epsilon \pm \hbar\omega \rightarrow \epsilon_m$.

The temperature $T_{\text{e}}(t)$ of the hot electrons may be determined using equation (11) or, approximately, from [1, 4]

$$\frac{\mathrm{d}T_{\text{e}}(t)}{\mathrm{d}t} = -\frac{T_{\text{e}}(t) - T_{\text{latt}}(t)}{\tau_2} + \cdots, \qquad (36)$$

where the relaxation time τ_2 resulting from the electron–lattice coupling describes the change of $T_{\text{e}}(t)$ after thermalization of the hot electrons due to electron–electron interaction. T_{latt} is the lattice temperature at time t (calculated as the average kinetic energy of the atoms over a time range around t). One may add a term in equation (36) due to diffusion of hot electrons into colder areas of the system.
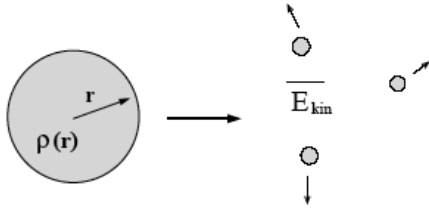
Figure 14. A simple model of the Coulomb explosion of the spherically symmetric charged cluster with the charge profile $\rho(r)$. Highly ionized atoms are emitted. Their kinetic energy and charge depend on the cluster size.

In order to apply the MD method to systems at non-equilibrium assuming constant pressure, but allowing for volume changes, one modifies the Lagrangian to [1, 4, 8, 11]

$$\mathcal{L} = L + K - P\Omega, \tag{37}$$

where K is the kinetic energy of the supercell chosen for the MD calculations. Ω is the volume of the supercell and P the external pressure. Then the equations of motion for the atoms are given again by equation (32) if L is replaced by $\mathcal{L}$.

In figure 13 we illustrate the modelling of the solid for the MD analysis. A supercell represents the solid upon applying appropriate periodic boundary conditions.

This MD analysis has been successfully used by Garcia *et al* for various problems such as graphitization of diamond due to hot electrons, ablation and absorption of covalent solids in strong electric fields and ultrafast melting of covalent crystals due to hot electrons [1]. For details, see in particular the thesis of Jeschke [1]. Note that if non-adiabatic behaviour plays a role, the method needs further modification.

2.4. Clusters at non-equilibrium: Coulomb explosion

The behaviour of clusters in intense electric fields is of fundamental interest. The interaction of strong femtosecond laser pulses with clusters, chains of molecules, nanostructures gives rise to fascinating phenomena: emission of x-rays, hot electron photoemission, electron stripping of atoms yielding highly charged ions and subsequent explosion. These are ultrafast processes occurring during times of the order of femtoseconds. As expected on general grounds, the excited (hot) electrons will cause, depending on the size of the system, a strongly inhomogeneous electric charge distribution and highly charged ions; see studies by Grigorenko *et al* [1, 8].

The scenario for the cluster explosion in an intense electric field illustrated in figure 14 consists of

(1) creation of a dense hot electron gas in the cluster region within a few femtoseconds,
(2) during the excitations, the cluster expanding on an ultrafast timescale and this changing the light absorption which may become resonant causing further emission of electrons,
(3) an ultrafast transfer of energy from the electrons to the ions causing, after 20–60 fs, ions with large kinetic energy and increasing ionization and thus explosion of the cluster.

As a theory for clusters in strong electric fields one may use the previous theory of Garcia *et al*. The Hamiltonian is given by [8]

$$H = H_{\mathrm{e}} + H_{\mathrm{ion}} + H_{\mathrm{field}}, \tag{38}$$

with H_{ion} relating to the ions and H_{field} to the coupling of the electrons to the external electric field $\mathcal{E}$. The electronic part of H is given by

$$H_{\mathrm{e}} = -\frac{\hbar^2}{2m}\nabla^2 + H_{\mathrm{e-e}} + H_{\mathrm{xc}}. \tag{39}$$

Here, $H_{\text{e-e}}$ is the Coulomb interaction between electrons and H_{xc} to the exchange–correlation potential and $H_{\text{e-ion}}$ results from the ion–electron coupling. Then, as before (assuming that H_{ion} dominates and there is a spatially uniform electric field) one gets

$$M\ddot{R}_i = -\nabla_i H_{\text{ion}}(\rho_{\text{e}}, \{R_k\}, t), \tag{40}$$

where H_{ion} is the Hamiltonian of the ions with positions R_i and ρ_{e} is the electron density calculated from the Schrödinger equation for H_{e}; see equation (39). Note that if $H_{\text{e}} = H_{\text{e}}(\rho_{\text{e}}, \{R_{ij}\}, t)$, then H_{e} must be included in equation (40). H_{ion} is given by

$$H_{\text{ion}} = \sum_{i=1}^{N} \frac{P_i^2}{2M} + \frac{1}{2} \sum_{i \neq j}^{N} \frac{Q_i^2}{R_{ij}} + H_{\text{e-ion}} - \sum_{i=1}^{N} Q_i \mathcal{E}(t) \sin(\omega t) R_i. \tag{41}$$

The terms in equation (41) are the kinetic energy of the ions, the Coulomb energy of the ions, the electron–ion coupling and the interaction of the ions with the external electric field $\mathcal{E}$, respectively. For simplicity, we assume the same charge Q for all ions and no screening of the Coulomb interaction. Depending on the cluster size and temperature, screening and ionic charge variation could play a role in reality.

Possibly in very strong electric fields and for a very hot plasma one may treat the cluster (and atomic chains) as a one-dimensional system in the direction of the electric field and as consisting of hot electrons with the common wavefunction Ψ. This simplifies the problem. It is remarkable that such a simplified theory may already yield essential features of the behaviour of clusters in strong electric fields; see studies by Grigorenko *et al* [1, 8].

2.5. Time dependent photon spectroscopy

Time resolved optics techniques [10, 14, 15] such as photoemission and higher harmonic light generation (SHG etc) and magneto-optics (Kerr effect) provide excellent tools for analysing the non-equilibrium behaviour of matter. In general, pump and probe analysis, including XAS (x-ray absorption spectroscopy), is an excellent tool for analysing temporal and spatial dependences:

2.5.1. Photoemission. In *single-photon electron emission* the time resolved photoelectron yield is given using response theory by [14]

$$j^{\text{PPE}}(t, \mathbf{k}\sigma) \sim \sum_q \int dt_1 \int dt_2\, \chi_{ij}(\mathbf{q}, \mathbf{k}\sigma, t + t_2 - t_1)\mathcal{E}_i(\mathbf{q}, t_1)\mathcal{E}_j(-\mathbf{q}, t_2), \tag{42}$$

with the response function

$$\chi_{ij}^{\text{PPE}}(t) = \frac{e^2}{\hbar^2} \frac{\gamma}{\Gamma} \sum_{1,2} M_{12}^i(q_z) M_{21}^j(-q_z) f(\epsilon_1) \exp\left(i\frac{\epsilon_1 - \epsilon_2}{\hbar}t - \Gamma_2 t\right). \tag{43}$$

Here, state 2 is the excited state occupied by the electrons after photon absorption in state 1 ($|\mathbf{k}, \sigma\rangle$) and z is the direction perpendicular to the surface. γ is the transition matrix element describing the escape of the photoelectrons and M is the dipole matrix element for the transition $1 \to 2$. $f(\epsilon_1)$ is the Fermi–Dirac distribution function. $\tau_2 \equiv \Gamma^{-1}$ is the lifetime of the excited electrons.

Clearly, 2PPE involving time delayed absorption of photons is best suited for probing the dynamics at non-equilibrium. Time resolved 2PPE is used to study directly the time dependent occupation of excited, non-equilibrium states and thus the lifetimes $\tau_{\mathbf{k}\sigma}(\epsilon)$ of excited electrons. The electron yield j^{2PPE} after absorption of two photons is given by [14]

$$j^{\text{2PPE}} \sim \int dt_1 \int dt_2 \int dt_3 \int dt_4\, \chi_{ijkl}^{\text{2PPE}}(t_1, \ldots) \mathcal{E}_i(t_1)\, \mathcal{E}_j(t_2)\, \mathcal{E}_k(t_3)\, \mathcal{E}_l(t_4) + \cdots, \tag{44}$$
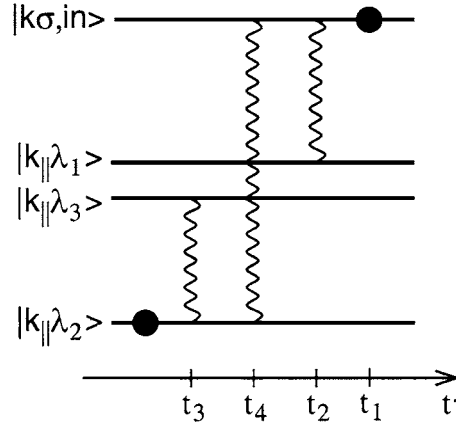
Figure 15. An interpretation of one of the processes contributing to 2PPE. An electron is excited from a pure state $|\mathbf{k}_\parallel \lambda_2\rangle$ in the Fermi sea to a pure state $|\mathbf{k}\sigma, \text{in}\rangle$ above E_{vac} by four interactions with the electric field at the times t_i. Note that the photoelectron current is proportional to the fourth power of the electric field and thus to the intensity *squared*, as expected for *two-photon* photoemission. The heavy wavy lines denote superpositions of states $|\mathbf{k}_\parallel \lambda_2\rangle$ and $|\mathbf{k}_\parallel \lambda_3\rangle$, $|\mathbf{k}_\parallel \lambda_2\rangle$ and $|\mathbf{k}\sigma, \text{in}\rangle$ etc, while the black dots represent electrons in pure eigenstates.

where the two photons are absorbed at times t_1 and t_2 (for illustration see figures 8 and 15). Note that the yield is proportional to the fourth power of the electric field, since the 2PPE is proportional to the intensity squared of single-photon photoemission; see equation (42) for j^{PPE}. The response function χ^{2PPE} in equation (44) is given by

$$
\chi_{ijkl}^{\text{2PPE}}(t) = \frac{e^4}{\hbar^4} \frac{\gamma}{\Gamma} \sum_{1,2,3} M_{k\sigma 1}^i M_{12}^j M_{23}^k M_{3k\sigma}^l
$$
$$
\times \Big\{ \Theta(t_1 - t_2)\Theta(t_2 - t_3)\Theta(t_3 - t_4) f(\epsilon_3) e^{-i\delta_{1k}(t_1-t_2)} e^{-i\delta_{2k}(t_2-t_3)} e^{-i\delta_{3k}(t_3-t_4)}
$$
$$
- \Theta(t_1 - t_2)\Theta(t_2 - t_4)\Theta(t_4 - t_3)\big(f(\epsilon_3) - f(\epsilon_2)\big)
$$
$$
\times e^{-i\delta_{1k}(t_1-t_2)} e^{-i\delta_{2k}(t_2-t_4)} e^{-i\delta_{23}(t_4-t_3)} + \cdots \Big\}. \tag{45}
$$

Here, γ and Γ are the escape probability and relaxation rate of the photoelectron, respectively. The various terms in $\{\cdots\}$ correspond to different temporal orders of interactions with the electric field; for details see Timm and Bennemann [14]. The photoelectron escapes from the state $|\mathbf{k}, \sigma\rangle$ with the probability γ. The second term in equation (45) is illustrated in figure 15, as an example. In equation (45) we use the complex transition energy

$$
\delta_{\alpha\beta} = (\epsilon_\alpha - \epsilon_\beta)/\hbar - i\Gamma_{\alpha\beta}, \tag{46}
$$

with dephasing rates

$$
\Gamma_{\alpha\beta} = (\tau_\alpha^{-1} + \tau_\beta^{-1})/2 + \Gamma_{\alpha\beta}'. \tag{47}
$$

τ_α is the lifetime of an electron in the state α, $\Gamma_{\alpha\beta}'$ describes additional dephasing with respect to the first term in equation (47). In figure 15 we characterize a typical contribution to the 2PPE. Closer inspection of the illustration clarifies the quantum mechanical interferences which are expected on general grounds.

Note that equation (45) contains all the dynamics reflected by the 2PPE and, in particular, interesting interference effects due to the interplay of the electric field with the polarization field resulting from the hot electrons which have absorbed one photon.

In ferromagnets the photoelectron yield reflects the spin polarization of the Fermi sea. Thus, one gets a spin polarized photoelectron yield

$$j^{2\text{PPE}} = j^{2\text{PPE}}(M(t), t, \ldots). \tag{48}$$

The numbers of excited electrons with spin up and down are different in the intermediate states occupied after one photon absorption. Also, circularly polarized light excites electrons spin selectively and thus yields a spin polarized 2PPE photocurrent.

2.5.2. Time dependent non-linear optics. As becomes clear from figure 8, the non-linear optics involving two photon absorptions and subsequent emission of a photon (SFG) is intimately related to 2PPE [14]. Response theory gives for the induced second-order polarization (see Hübner *et al* [10, 14, 16]) the expression

$$P_i^{(2)}(t) = \frac{1}{(2\pi)^2} \int dt_1 \int dt_2 \, \chi_{ijl}^{(2)}(t - t_1, t_1 - t_2) \, \mathcal{E}_j(t_1) \, \mathcal{E}_1(t_2). \tag{49}$$

Here, $\chi_{ijl}^{(2)}$ denotes the non-linear susceptibility and involves for example three dipole transition matrix elements; it is hence non-zero only if inversion symmetry is broken [10]. The two photons are absorbed at the times t_1 and t_2 and thus $t_1 - t_2$ characterizes the delay of the second photon absorption. Of course, the intensity of SFG emitted light is given by

$$I^{(2)} \propto \int dt \left[P^{(2)}(t) \right]^2 \tag{50}$$

if one averages over the time dependence of the emitted light. For simplicity, we have dropped indices and the Fresnel like factors in the equations. Note, however, that these are, for many problems, important. Note that equation (50) describes interesting interference effects due to $P^{(2)}$ and the external electric field $\mathcal{E}(t)$.

For studying magnetism and in particular magnetization changes $\delta M(t)$ due to hot electrons and $T_e(t)$, it is important to note that as regards the magnetization dependence the non-linear susceptibility $\chi^{(2)}\{M\}$ can be decomposed into [10, 15, 16]

$$\chi_{ijl}^{(2)}\{M\} = \chi_{ijl,\text{even}}^{(2)}\{M\} + \chi_{ijl,\text{odd}}^{(2)}\{M\}. \tag{51}$$

Here, $\chi_{ijl,\text{even}}^{(2)}$ is even in M and $\chi_{ijl,\text{odd}}^{(2)}$ odd in M. We have

$$\chi_{ijl,\text{odd}}^{(2)} \sim M + \cdots. \tag{52}$$

From this one expects SHG to yield for intensities ($\delta^- \sim \{I(M) - I(-M)\}$)

$$I(M) - I(-M) \underset{t}{\rightarrow} M + \cdots. \tag{53}$$

Note that changes in M require transfer of angular momentum and can only occur if angular momentum is conserved. This may involve transfer of angular momentum via spin–orbit coupling. Thus, ultrafast changes (during a few femtoseconds, up to a few hundred femtoseconds) of $M(t)$ may occur.

2.5.3. Spin dynamics in nanostructures, magnetization reversal and hysteresis dynamics. For many problems involving magnetization dynamics such as relaxation of the spin order, for example in antiferromagnets (af) and in af film structures after application of an external magnetic field h, one may use the Landau–Lifshitz type equation given by Bloch–Bloembergen [17]:

$$\frac{dM}{dt} = \frac{dM}{dt}\bigg|_{h=0} -\gamma \mu_0 (M \times h) - \frac{\lambda}{M_s^2} (M \times [M \times h]). \tag{54}$$

Here, γ is the precessional torque, λ to a damping factor and M_s to the magnetization saturation. The term $(dM/dt)_{h=0}$ was discussed before. Typically equation (54) describes dynamics (such as magnetization reversal at surfaces, thin films) occurring during times of the order of ps up to 100 ps or more. Equation (54) describes the interplay of h and internal (exchange, dipolar) fields and may be used to study the influence of hot electrons on magnetization dynamics. In particular, hot electrons affect the reorientation transition at surfaces and domain wall dynamics.

Frequently, relaxation of the magnetization towards its equilibrium after the external magnetic field is turned off is controlled by magnetic anisotropy (E_{anis}) or more generally by the interplay of exchange and spin–orbit interaction. Then, one expects relaxation times of the order of

$$t \sim E_{anis}^{-1}. \tag{55}$$

This gives relaxation times of picoseconds or more.

Non-equilibrium magnetic behaviour occurs for nanostructured thin films during growth, for example. For thin, inhomogeneous films with island like structure the varying island anisotropies causing magnetic energy barriers between the islands may impede long range homogeneous magnetization. The relaxation of the magnetization depends then sensitively on the range of the magnetic coupling of the islands, on the film structure in general and on temperature T. For nearly isolated islands (e.g. below the percolation limit) one gets, below the blocking temperature given by (using the Arrhenius–Néel ansatz with observation time τ_m and island magnetization reversal rate Γ)

$$k_B T_b = \frac{NK}{\ln(\tau_m \Gamma)}, \tag{56}$$

a non-equilibrium magnetization. Then alignment of neighbouring island magnetization occurs via coherent island spin flips. The times τ for this are controlled by the magnetic energy barriers between the islands [7]. Approximately, one has

$$\tau = \tau_0 \exp \frac{1}{T} \{aKx - bJx\}, \tag{57}$$

with $\tau_0 \approx 10^{-9}$ s. K and J are the anisotropy and exchange constants and x is the density of islands. Note that for a system of nearly isolated islands one gets for equilibrium

$$M \underset{t}{\to} M_{eq} = 0. \tag{58}$$

Above the percolation limit when islands couple more and more (via exchange or dipole coupling) one has

$$M(t) \underset{t}{\to} \sum_i M_i \exp\left(\frac{-2t}{\tau_i}\right), \tag{59}$$

with the ith island relaxation time

$$\tau_i = \tau_0 \exp\left(\frac{\Delta E_i}{kT}\right). \tag{60}$$

Here, τ_0 is the moment precession time ($\propto 10^{-9}$ s) and ΔE_i the energy barrier for the ith island against magnetization changes. Now, at equilibrium,

$$M \underset{t}{\to} M_{eq} > 0. \tag{61}$$

In general one expects the relaxation of the magnetization to depend characteristically on the atomic structure of the magnetic film and on the range of the coupling between the islands.

Note that magnetic clusters will exhibit characteristic rotation dynamics in an external magnetic field. One expects a resonance like behaviour of the magnetization for $\omega \simeq \omega_{\text{rot}}$. Here, ω and ω_{rot} are the frequencies of the magnetic field and the rotating cluster, respectively. Such dynamics is observed in Stern–Gerlach experiments, for example [61].

In the next section, we present representative results for non-equilibrium behaviour: (a) *lifetimes* of excited electrons, (b) *relaxation* of *magnetization*, (c) ultrafast *structural changes* and (d) *matter* in strong *electric fields*.

3. Results

The study of excited matter in strong electric fields is a relatively young research area. Hence, comparison of experimental results obtained by *pump–probe optical measurements (2PPE, non-linear optics*, x-ray *absorption spectroscopy (XAS)*, for example) and new theory is of vital importance. In particular, XAS may further advance the spatial resolution of non-equilibrium physics and provide information on local processes.

In the following, characteristic results are presented on:

3.1. Lifetimes of excited electrons in metals.
3.2. 2PPE yield.
3.3. Magnetism at non-equilibrium.
3.4. Magnetic relaxation in clusters and nanostructures.
3.5. Dynamics in high T_c superconductors.
3.6. Ultrafast structural changes in covalent crystals due to hot electrons.
3.7. Clusters in strong electric fields: Coulomb explosion.

All results demonstrate that first the electrons absorb, on a femtosecond timescale, the electric field energy and that the hot electrons transfer, then, the energy to the atomic structure during a time ranging from below picoseconds to picoseconds. In particular, non-equilibrium magnetic relaxation is evidently controlled by angular momentum conservation. Then, frequently spin–orbit coupling and magnetic anisotropy control the timescale for changes. This is important for the response time of magnetization to hot electrons, for magnetization reversals in an external magnetic field and for ageing processes in magnetic recording.

In figure 16 we illustrate the generation of non-equilibrium matter due to (laser) irradiation. In the case of a dense system of excited electrons we have to calculate the temperature $T_e(t)$ of the hot electrons which, due to electron–electron interactions, thermalize very rapidly within a time of the order of a few femtoseconds up to 10–20 fs or more. Then excited electrons transfer their energy to the lattice via electron–phonon coupling to the colder regions of matter via diffusion. The maximal temperature $T_e(t)$ of the hot electrons is controlled by the interplay of the electric field intensity $I(t)$ and electron–lattice relaxation and diffusion. Typically $T_e(t) \rightarrow T_{\text{latt}}(t)$ after a few picoseconds. In non-equilibrium ($T_e(t) > T_{\text{latt}}(t)$), the various properties A of matter such as conductivity, absorption, reflectance, structure and magnetization respond to $T_e(t)$ and in general one observes

$$A = A(T_e(t), I(t), t). \tag{62}$$

3.1. Lifetimes of excited electrons in metals

We assume first a diluted gas of excited electrons due to absorption of photons with energy $\hbar\omega$. For small excitation energies ($\mathcal{E} - \mathcal{E}_{\text{F}}$), where $\mathcal{E}_{\text{F}}$ is the Fermi energy, one expects lifetimes τ as given by Fermi liquid theory. (In the case of strong electron–electron coupling one expects deviations from Fermi liquid theory with $\tau^{-1} \sim \omega^2$.) The lifetimes

$$\tau_{\mathbf{k}} \sim (\text{Im}\, \Sigma(\omega))^{-1} \tag{63}$$
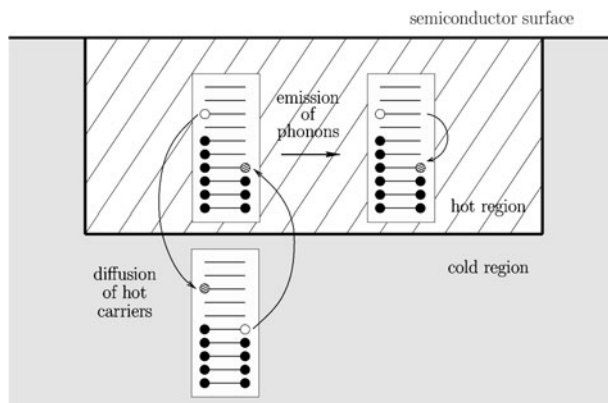
Figure 16. An illustration of two important mechanisms which contribute to the relaxation of the laser excited electronic system: loss of energy to the lattice (emission of phonons) and diffusion of hot carriers into the cold part of the solid.
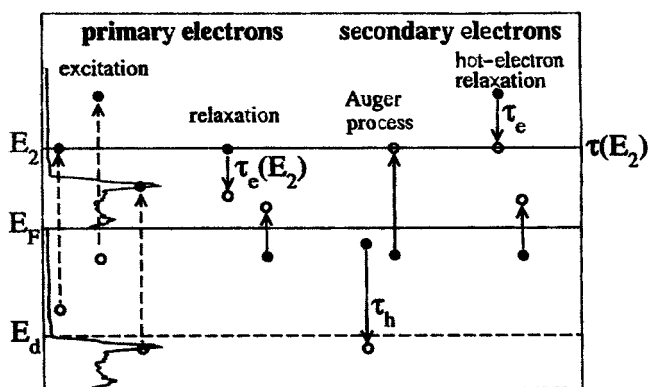

Figure 17. An illustration of secondary-electron generation involved in photoemission (2PPE).

determined using for example 2PPE are in the range of femtoseconds; see the theory in section 2. In view of the excitation processes illustrated in figure 17 one needs to take into account secondary electrons (Auger electrons, for example) to extract from the measured 2PPE yield the lifetimes $\tau_{\mathbf{k}}$. For details, see the review by Knorren *et al* [9].

In figure 18 experimental lifetime results obtained by Aeschlimann *et al* are shown [18]. Note the rather different lifetimes for small excitation energies, $E^* - E_F \to 0$, due to the varying DOS near E_F. Note that, approximately, $\tau^{-1} \propto N(E_F)$. Further experiments might also indicate an interesting dependence on the Fermi surface structure.

In figure 19 we present theoretical results obtained by Knorren *et al* [9, 19] using a Boltzmann type analysis. Also, results of calculations by Campillo *et al* [20] and Keyling *et al* [21] are given. All these theoretical results compare well with experiment. In particular, Ekardt *et al* calculated a very interesting $\mathbf{k}$ dependence of the lifetimes.

Due to the travelling of the hot electrons in the crystal before they escape to the vacuum one expects mean free paths and temperature effects on the lifetime $\tau_{\mathbf{k}}$. This is shown in figure 20 [9]. Note that this dependence is of basic interest, since it shows that 2PPE might provide a very powerful tool for analysing electronic properties of matter, metals, thin films etc.

Of particular interest is the spin dependent excitation of electrons expected for ferromagnetic solids (transition metals etc) and for circularly polarized light. In figures 21 and 22 experimental [22, 23] and theoretical results are given for the lifetimes of excited electrons in Ni, Co and Fe. Comparison of theory and experiment (see Siegmann *et al*)
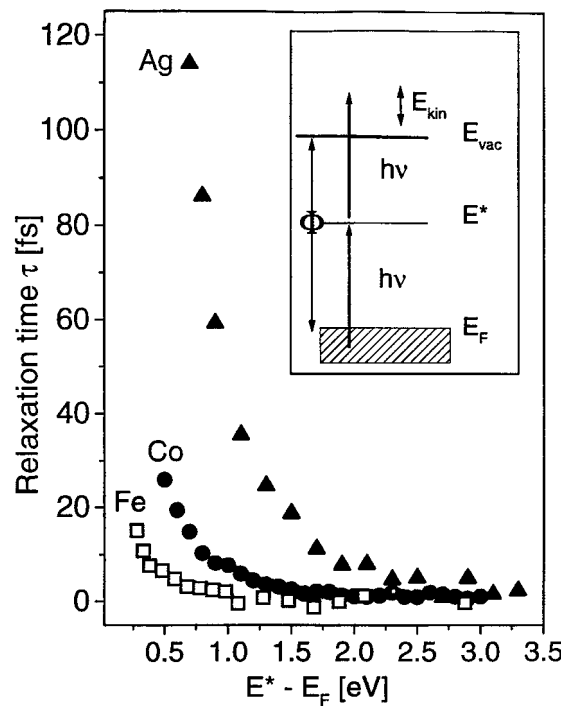
Figure 18. Experimental results for lifetimes of excited electrons at energy E^* obtained by Aeschlimann, Siegmann *et al* (ϕ is the work-function, E_F the Fermi energy).
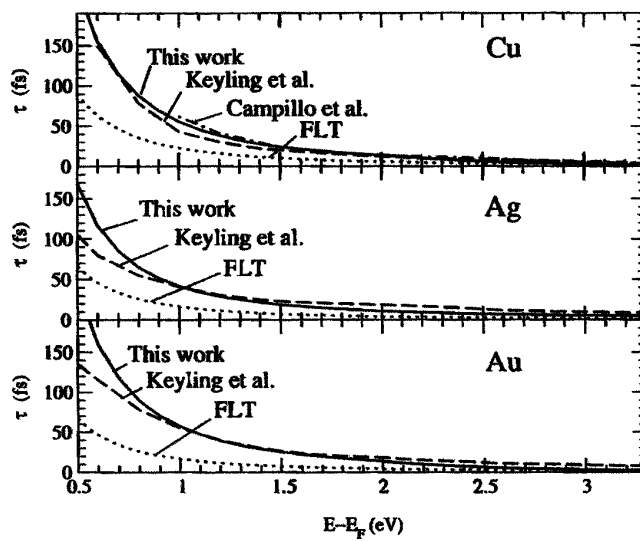

Figure 19. Single-electron lifetimes for Cu, Ag and Au calculated by Knorren *et al* in the random-k approximation. Also results of FLT and of *ab initio* calculations by Campillo *et al* and by Keyling *et al* are shown.

indicates problems as regards the explanation of measurements [9][1]. This is of fundamental interest and needs further study.

In figure 21 we present results for the spin dependent lifetimes of excited electrons in the classical ferromagnets. The dependence of $\tau_{ave} = (\tau_\uparrow + \tau_\downarrow)/2$ on the spin dependent Coulomb interaction is given [9].

---

[1] The parameters needed to get agreement with experiment should be derived from first principles.
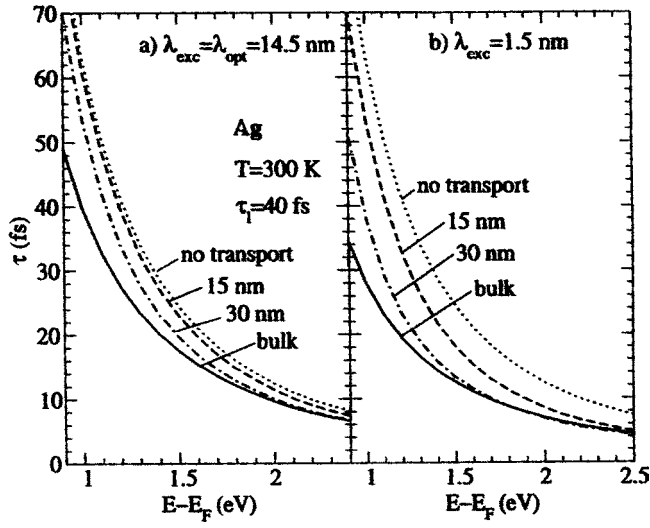
Figure 20. Times of relaxation in Ag films of different thicknesses. Theoretical results obtained by Knorren *et al* for two cases: (a) excitation within the optical penetration depth $\lambda_{opt} = 14.5$ nm; (b) excitation only within $\lambda_{exc} = 1.5$ nm to simulate a surface excitation. The temperature is $T = 300$ K and the laser pulse duration is $\tau_l = 40$ fs.

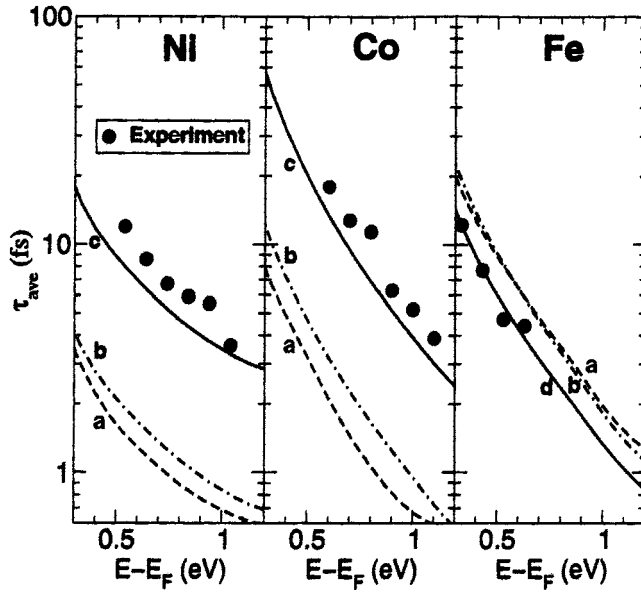**Figure 21.** The spin averaged effective relaxation time for a pulse with 40 fs duration and 3.0 eV photon energy is given. For the calculations, Knorren *et al* used for Coulomb matrix elements (a) $M = 0.8$ eV, $m = M^{\uparrow\uparrow}/M^{\uparrow\downarrow} = 1$, (b) $M = 0.8$ eV, $m = 0.5$, (c) $M = 0.4$ eV, $m = 0.5$, (d) $M = 1.0$ eV, $m = 0.5$.

In figure 22 we present results for the spin dependent lifetimes τ_σ for the classical ferromagnets Ni, Co, Fe [9]. It is important to calculate the matrix elements M, m from first principles. Note that M, m are of fundamental interest for magnetism.
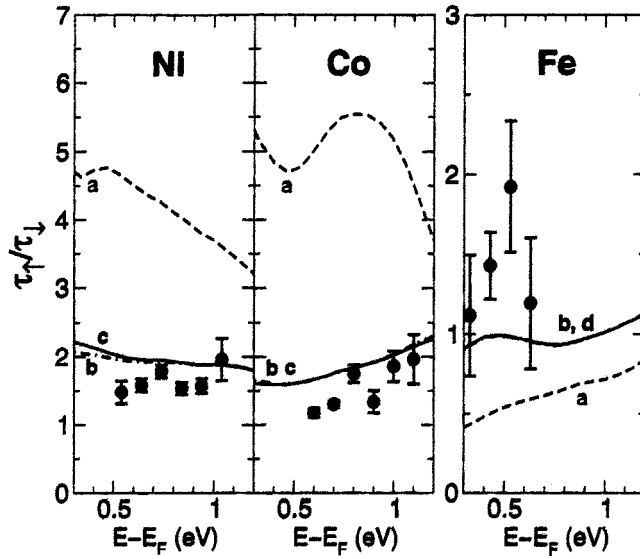
Figure 22. Results for $\tau_\uparrow/\tau_\downarrow$. The photon energy is 3.0 eV and the exciting laser pulse has a duration of 40 fs. For the Coulomb matrix elements we use for the calculations (a) $M = 0.8$ eV, $m = M^{\uparrow\uparrow}/M^{\uparrow\downarrow} = 1$, (b) $M = 0.8$ eV, $m = 0.5$, (c) $M = 0.4$ eV, $m = 0.5$, (d) $M = 1.0$ eV, $m = 0.5$. ($\bar{\Phi}$ = experimental; Siegmann *et al.*)

3.2. 2PPE yield

In figures 23 and 24 we present 2PPE results showing the dependence of the photoelectron yield on the delay time between the two photon absorptions. These results were obtained using the response theory described in section 2 [14]. The interference of the external electric field and the induced field caused by the hot electrons in the intermediate state after one photon absorption reveals, in a characteristic way, the dynamics of the non-equilibrium solid.

The results shown in figure 23 depend on the band structure. The **k** vector is chosen such that the transition frequencies perfectly match the frequency of incoming light. Only results for $\Delta T > 0$ are shown, since the curve is symmetric about $\Delta T = 0$ for identical pump and probe pulses. All curves in this and the following figures are scaled such that the limit for large ΔT is unity. Figure 23(b) shows total SHG yield for single-colour pump–probe SHG as a function of the delay time ΔT, using the same parameters. The inset shows the SHG yield for *flat* bands with transition frequencies that match the light frequency perfectly. Note that for extracting relaxation rates from experimental data the resolution of the photoelectron and SHG light detectors must be taken into account.

The results in figure 24 indicate how the 2PPE yield depends on the lifetime of the excited electrons which have absorbed one photon and which are in the states $|2\rangle$ ($|1\rangle \rightarrow_\omega |2\rangle \rightarrow$ photoelectron). Note that the oscillations reflect revealing physics of the interplay of matter dynamics and the electromagnetic field; for details see [14].

3.3. The response of magnetism (dense excitations)

In strong electric fields a relatively high density of excited electrons with electronic temperature $T_e(t) > T_{latt}(t)$ is obtained. How quickly does the magnetization, for example, respond to $T_e(t)$ now? Angular momentum conservation requires that for a uniformly excited ferromagnet the
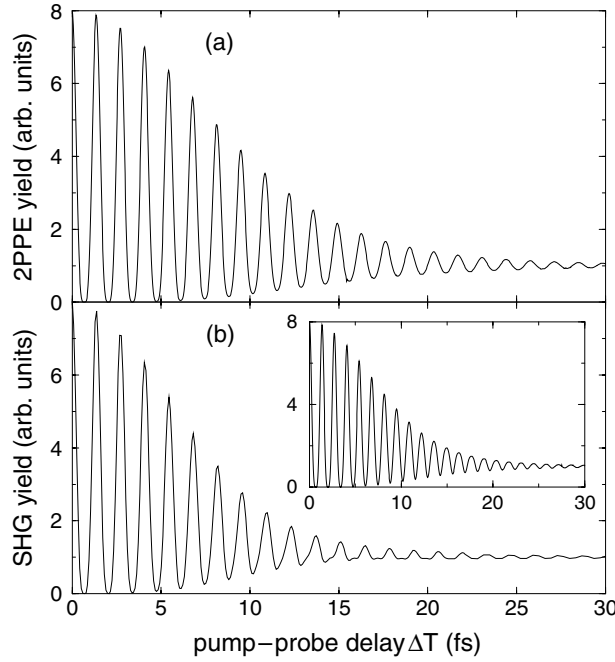
Figure 23. (a) The total 2PPE yield of photoelectrons of momentum **k** for single-colour pump–probe investigation as a function of the delay time ΔT between pump and probe pulses. (b) The SHG yield, using the same parameters. The inset relates to flat bands with transition frequency equal to the photon one. (For calculations, see Timm *et al*.)

spin–lattice coupling controls the time dependent changes of the magnetization $M(T_e)$ to $T_e(t)$. Hence, response times of the order of

$$t \sim \tau_{so} \tag{64}$$

($\tau_{so} \sim$ 100–200 fs or more for transition metals, less for rare-earth metals, for example) are expected. This may yield in general a somewhat slower response of the spin system as compared to the thermalization of the electrons. Such behaviour of the response should be reflected by magneto-optics (Kerr angle: $\phi_K(t) = \phi_K(M(t), \ldots)$, by 2PPE ($j^{2PPE} \sim n_{i\sigma}(t)$) and by SHG with $\chi_{ijl}(M(t))$) [10].

In figure 25 we present results for $T_e(t)$ obtained using typical parameters for transition metals such as Ni [11]. The calculations yield that $M \to 0$ for laser field intensities (fluence F) causing T_e to increase above the Curie temperature T_C. There is a somewhat slower but still ultrafast (sub-ps to ps) response of the spin order.

As shown in figures 26 and 27, experiments by Matthias *et al* seem to support this [5, 10, 11, 24]. Results reflect that δI^- responds to changes in M. Note that for thin films of Ni on Cu one finds that the Curie temperature T_C depends on the film thickness d: $T_c = T_C(d)$. Thus, on varying the film thickness d one expects characteristic changes in the magneto-optical behaviour, since the film changes from paramagnetic to ferromagnetic ordering as d increases. Experimental results reflect this; see the results given by Güdde *et al* shown in figure 27 [5, 10, 24].

The results obtained by Matthias *et al* [11, 24] and the MOKE results obtained by Beaurepaire *et al* [12] show that the magnetization (due to itinerant electron spins) follows, with a certain delay, the electron response to the hot electrons.
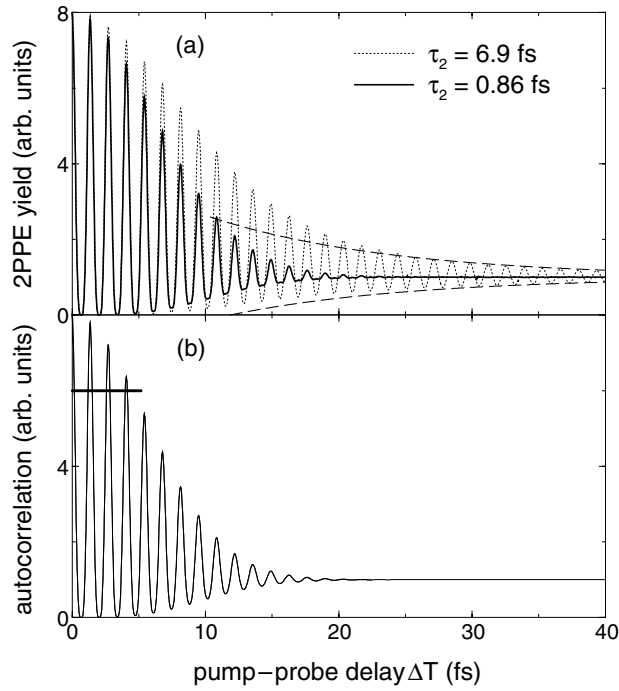
Figure 24. A demonstration of the lifetime dependence of 2PPE. (a) The total 2PPE yield for the same model parameters as were used in figure 23 with a lifetime of states in the intermediate band of $\tau_2 = 6.9$ fs (dotted curve) and with the very small value $\tau_2 = 0.86$ fs (heavy solid curve). The dashed curves show the exponential decay with the dephasing rate $\Gamma_{12} = \tau_2^{-1}/2$ for $\tau_2 = 6.9$ fs. (b) The four-field autocorrelation function of the pump–probe laser field. Note the similarity to the fast relaxation result in figure (a). The black bar denotes half the laser pulse duration.

Similar interesting experiments probing the time dependence resulting from $T_e(t)$ of the magneto-optics and magnetization switching and hysteresis behaviour were performed by Rasing *et al* [25], Koopmans [26], Gerrits [17] and others [27].

In figure 26 we show experimental results obtained by Matthias *et al* for the effect of hot electrons on the magnetization ($\delta I^- \propto I(M) - I(-M)$) [10, 11]. In figure 26(a) the dependence of δI^- on the substrate temperature is given. Note that the Curie temperature T_c depends on the film thickness: $d(T_c = T_c(d))$ and at a temperature 395 K one is above T_c and at 353 and 296 K below T_c. This is reflected by the increase of δI^- for increasing pump–probe delay time. Note that $\delta I^-(t) \to_t M(T_e(t))$ for longer times as $T_e \to T_{latt}$. After the decrease of M due to hot electrons, M increases again, since $T_e(t)$ decreases. Figure 26(b) reflects the dependence of $M(t)$ on the number of hot electrons, which increases with increasing laser fluence (μJ). Correspondingly, one expects a larger decrease of δI^- for increasing fluence and a relaxation of the magnetization according to $\delta I^- \propto M(t)$, $T_e \to T_{latt}$, for longer times. Note that $\delta I^- \to 0$ as $M \to 0$.

In figure 27 we show results obtained by Matthias *et al* for the dependence of the change of the SHG intensity (p $\to$ P polarization; transverse geometry if $M \neq 0$) on the thickness d of Ni films [10, 11]. Note that $T_c = T_c(d)$ and hence for a given film (substrate) temperature T the paramagnetic films become ferromagnetic as d increases ($d \gtrsim 5$ ML). Correspondingly, one expects $\delta I^- \neq 0$ as soon as $T < T_c(d)$. Hence, the results reflect again that $\delta I^- = \delta I^-(M(t))$. It is also indicated that the time τ for $T_e \to T_{latt}$ increases as d increases.
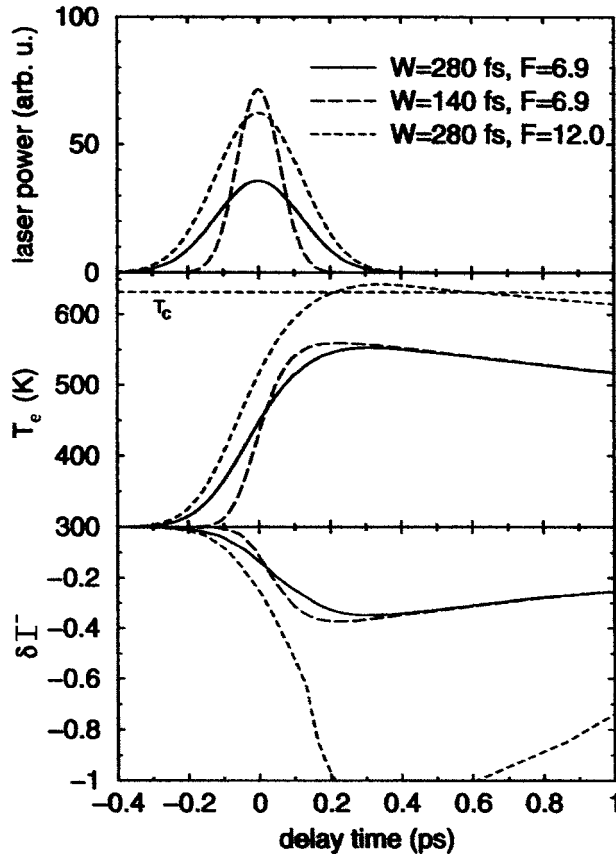
Figure 25. Results obtained by Knorren *et al* for the profile of the pump pulse, electron temperature and SHG difference signal for laser pulses with width W equal to 140 and 280 fs and fluence $F = 6.9$ and 12.0 (mJ cm^{-2}). $\delta I^- \sim (I(M) - I(-M))$ is the magnetic SHG signal.

In figure 28 we show results obtained by Matthias *et al* on time resolved magnetic SHG for p $\rightarrow$ P polarization in Ni [10, 11]. Again the decrease of the SHG yield and of the yields E_{nonmag} and E_{mag}, corresponding to $\delta I^+(t)$ and $\delta I^-(t)$, reflect the increase of T_{e} and decrease of the magnetization. For increasing pump–probe delay time one has $T_{\mathrm{e}} \rightarrow_t T_{\mathrm{latt}}$ and M relaxes according to $M(t) = M(T_{\mathrm{e}} \approx T_{\mathrm{latt}})$. Note that the minimum in $E_{\mathrm{mag}} (\delta I^-(t))$ occurs somewhat later than that in $E_{\mathrm{nonmag}} (\delta I^+(t))$; see the arrows.

Note that the SHG results shown are of basic interest and reflect sensitively the symmetry and the recovery of Ni from the hot electrons. Theoretical analysis by Knorren and Bennemann predicts that $|E_{\mathrm{mag}}| \propto M(t)$ for larger delay times. The recovery of the field $|E_{\mathrm{nonmag}}|$ reflects the hot electron–lattice coupling. Note that $T_{\mathrm{e}} \rightarrow T_{\mathrm{latt}}$ for times of the order of a few picoseconds.

Note that more interesting experiments of this type are needed to understand what happens for very short times (of the order of a few femtoseconds) to $T_{\mathrm{e}}(t)$ and $M(t)$ and what controls angular momentum conservation. For comparison, see also the interesting experimental results obtained by Eberhardt *et al* [63].

In figure 29 results are shown which were obtained by Beaurepaire *et al* for the Kerr effect in Ni [12]. Again these show that $M \rightarrow 0$ as hot electrons occur due to excitations by a laser pulse. The change of the Kerr effect increases as the pump fluence increases, in accordance with $T_{\mathrm{c}}(T)$.
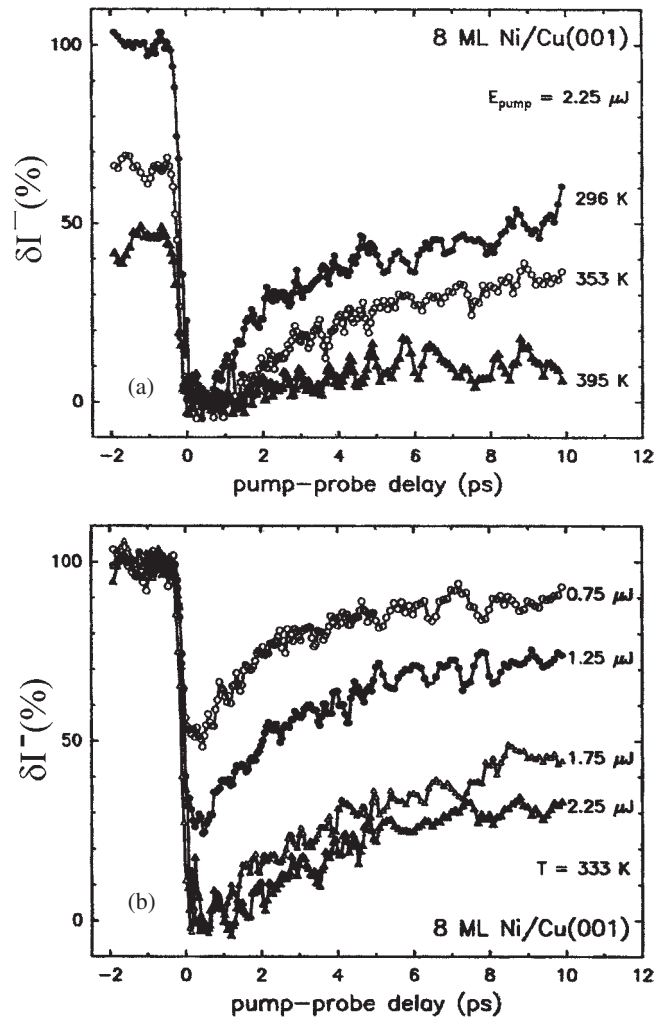
Figure 26. The breakdown of the magnetization for a film of 8 ML Ni/Cu(001) due to hot electrons; see the experiments by Matthias *et al* [10, 15]. Plotted is the relative difference $\delta I^-(t)$ for p–P polarization as a function of pump–probe delay for different (a) substrate temperatures and (b) laser fluences. Here, $\delta I^-(t)$ is calculated for all curves as $I_0^\uparrow - I_0^\downarrow$ for $T = 296$ K. The energy of the p polarized pump light was 2.25 μJ.

Note that the Kerr effect will also reflect possible magnetic reorientation transitions due to $T_e(t)$ ($M_\perp \rightleftarrows M_\parallel$, for example) at surfaces of ferromagnets. Note that SHG (NOLIMOKE— see later) measurements are very symmetry sensitive.

3.4. Magnetic relaxation in clusters and nanostructures

If the magnetization dynamics is controlled by magnetic anisotropy as for magnetic clusters in external magnetic fields [7] and for magnetic nanostructures, then the relaxation, ageing of magnetic structures, occurs during times of the order of nanoseconds to seconds; see the previous discussion and figures for this relatively slow timescale. Note that the relaxation times reflect the atomic structure and the magnetic interactions (such as exchange interaction,
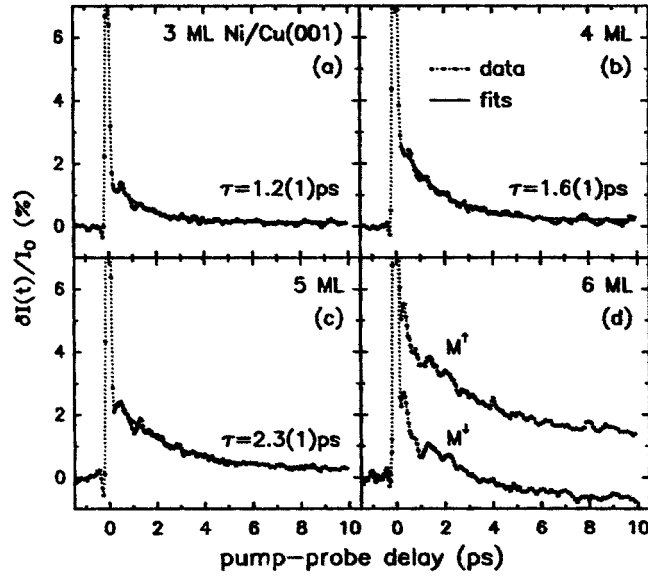
Figure 27. Results obtained by Matthias *et al* [10] for the relative change of the p–P polarized probe SHG signal as a function of the pump–probe delay time for various monolayers of Ni on Cu(001). The substrate temperature is 323 K. For 6 ML the Curie temperature is larger than the substrate temperature, while it is smaller for the case of 3–5 ML films.

magnetic dipole coupling). The relaxation of the magnetization in nanostructures was calculated using a Hamiltonian including exchange, dipole interaction, magnetic anisotropy and Monte Carlo (MC) analysis as developed by Brinzanik *et al* [7, 28].

In figure 30 typical results obtained by Brinzanik *et al* are shown for the relaxation of the magnetization in nanostructured thin magnetic films after the external magnetic field is turned off. (The Monte Carlo time 10^1 corresponds to 1 s, approximately.) The film consists of magnetic islands which are, below the percolation limit ($\ominus \lesssim 0.9$ ML), nearly magnetically isolated from each other and then increasingly coupled as $\ominus$ increases above $\ominus_p = 0.9$ ML. Note that $M \to_t M_{eq} \simeq 0$ for $\ominus < \ominus_p$; the equilibrium magnetization is $M_{eq} > 0$ for $\ominus > \ominus_p$. The interplay of anisotropy and exchange controls the relaxation $M(t) \to M_{eq}$.

Clearly, one expects the relaxation to reflect characteristically the structure of the film and the magnetic interactions. Note that, depending on the average distance between the magnetic domains (islands), a different interaction may dominate. In figure 31 we show MC results obtained by Brinzanik *et al* which support this [28]. Of general interest is the interplay of dipole and anisotropy coupling. The latter is controlling the in-plane versus out-of-plane orientation of the magnetization at the film surface.

The dynamics of rotating magnetic clusters also exhibits characteristic behaviour in an external magnetic field oscillating with frequency ω (see Stern–Gerlach type experiments, Mie scattering, for example). One expects then for an ensemble of clusters that the magnetization (Langevin magnetization obtained from the Bloch equation; see calculations by Jensen *et al*) will show resonance like behaviour (a dip) at

$$\omega \simeq \omega_{rot}, \qquad \omega_{rot} = \delta h_0 p \qquad (65)$$

with $\delta = g\mu_B/\hbar$, $g =$ the Landé factor, $h_0 =$ the external magnetic field, p is the multiplicity of the rotating field axes experienced in cluster magnetization, $p = 2$ for uniaxial and $p = 4$ for cubic lattice anisotropy. Note that for a cluster ensemble one has for ω_{rot} a Gibbs or
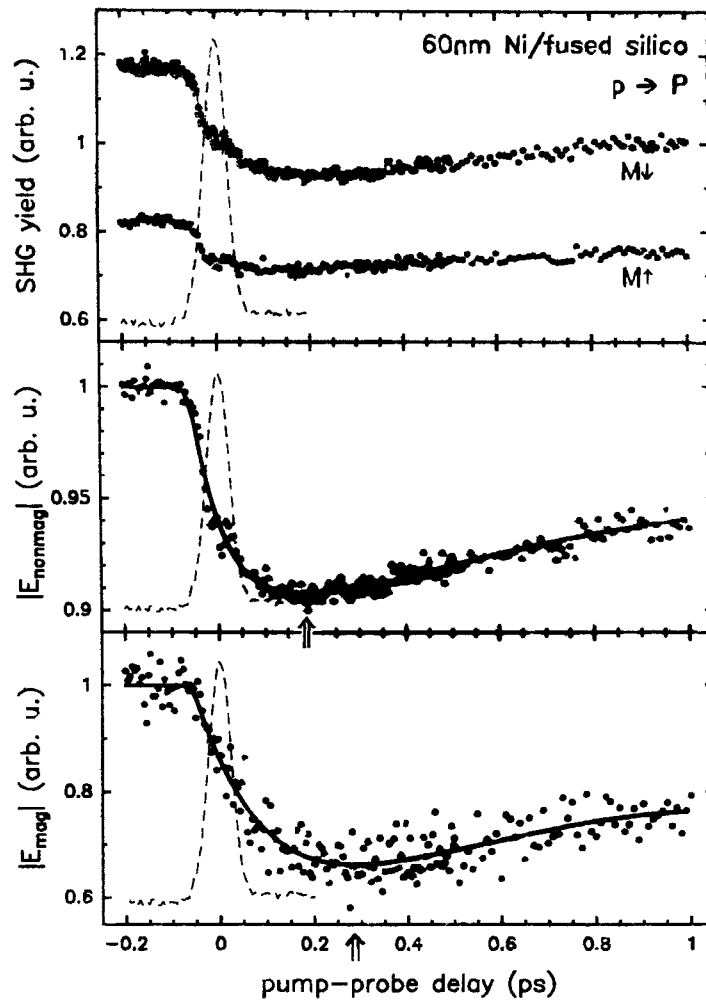
Figure 28. Time resolved MSHG. Experimental results obtained by Matthias *et al* for the breakdown of magnetism in Ni due to hot electrons are shown. (The dashed curve relates to the laser pulse shape [10, 11, 24].) The fluence of the irradiation is such that $T_e < T_c$. The intensities E_{nonmag} and E_{mag} correspond to $\delta I^{\pm} \propto I(M) \pm I(-M)$, respectively. The arrows indicate the minimum.

Gauss distribution. This is in agreement with experiments by de Heer *et al* [51]. Note that the dependence of the resonance on the anisotropy symmetry is characterized by p.

3.5. Short time dynamics in high T_c superconductors

Due to the interesting phase diagram of high T_c superconductors such as YBCO, one expects various characteristic response times reflecting electronic correlations, antiferromagnetic excitations, breaking up of Cooper pair phase coherence and Cooper pairs, for example [6]. In particular, for underdoped cuprates the Meissner effect and the superconducting phase transition occur at the superconducting transition temperature T_c and at temperatures above T_c phase incoherent Cooper pairs might be present [29].
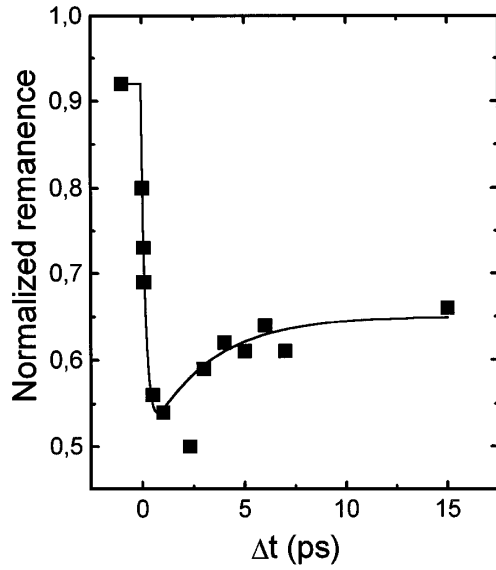
Figure 29. Results obtained by Beaurepaire *et al* for the transient remanent longitudinal MOKE signal of a Ni(20 nm)/ MgF$_2$(100 nm) film and for 7 mJ cm^{-2} pump fluence [12]. The signal is normalized to the signal measured for zero fluence.
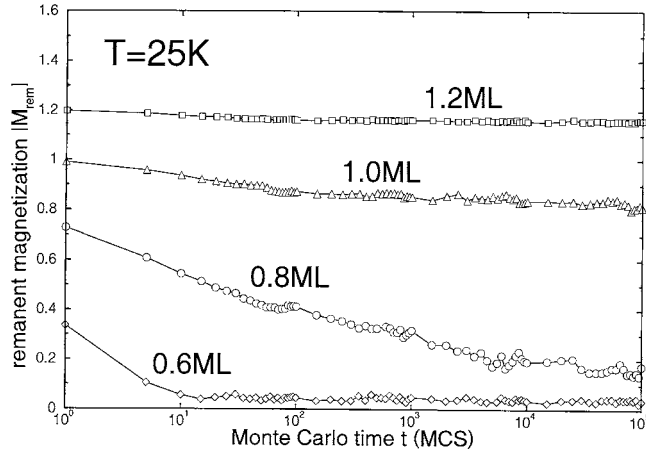

Figure 30. The relaxation of the remanent film magnetization $|M_{\text{rem}}(\ominus, T, t)|$ as a function of the Monte Carlo (MC) time t for different coverages $\ominus$ below and above the percolation threshold $\ominus_p = 0.9$ ML at temperature $T = 25$ K. Within the kinetic MC simulation, the time $t = 1$ MCS corresponds approximately to 0.1 s. The single-island anisotropy $K = 0.01$ meV/atom and the inter-island exchange coupling $\gamma = 5.6$ meV/bond are taken into account. The relaxation of the magnetization towards the equilibrium magnetization $|M_{\text{eq}}|$ is controlled by anisotropy energy barriers. For coverages $\ominus > \ominus_p$ the magnetization relaxes towards $|M_{\text{eq}}| \neq 0$ and for $\ominus < \ominus_p$ towards $|M_{\text{eq}}| = 0$. Here, at lower temperatures T the inter-island dipole coupling can lead to a long range magnetic order with $|M_{\text{eq}}| \neq 0$; for details see Brinzanik *et al*.

In figure 32 we show results for the superfluid density n_s. Note the discrepancy between the theory neglecting Cooper pair phase fluctuations and dynamical Meissner effect measurements at field frequencies ω. Clearly for observation times $t \sim \omega^{-1}$ such that $\omega\tau > 1$, where τ is the characteristic time of a Cooper pair phase fluctuation, this discrepancy should disappear [6, 30]. Results obtained using the Kosterlitz–Thouless (KT) theory are indicated. Note that the phase fluctuations and their lifetimes are of basic interest as regards the nature of the superconducting
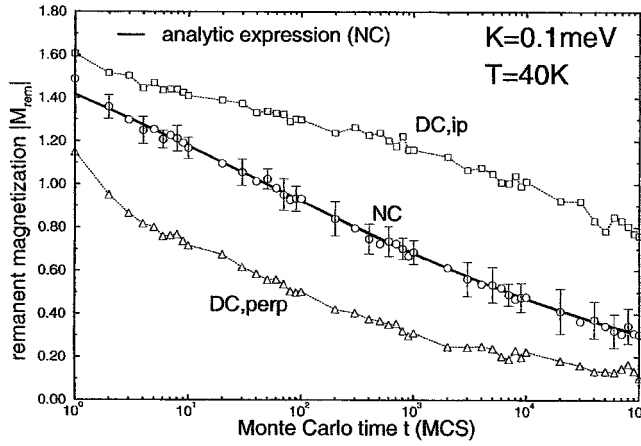
Figure 31. The remanent magnetization $|M_{\rm rem}(T, t)|$ of a nanostructured film is plotted as a function of MC time t for temperature $T = 40$ K and anisotropy parameter $K = 0.1$ meV. The solid curve relates to results obtained for the non-coupled (NC) island system. The MC results are indicated by the symbols. Results for non-coupled as well as dipole-coupled (DC) in-plane (ip) and out-of-plane (perp) magnetization are shown; see calculations by Brinzanik *et al*.

transition (superconductivity of BCS type versus Bose–Einstein condensation etc). Further results obtained by Timm *et al* on the dynamical phase stiffness of $n_s(\omega)$ are shown in figure 33. For breaking up Cooper pairs via photon absorption one expects a recombination relaxation time of the order of

$$t \sim \Delta^{-1} \sim T_{\rm c}^{-1}. \tag{66}$$

Using the results for $T_{\rm c}(x)$ for cuprates we estimate relaxation times of the order of a few hundred femtoseconds to a picosecond. Note that x is the hole doping concentration. Similarly, one may expect a characteristic relaxation time for the breaking up of antiferromagnetic
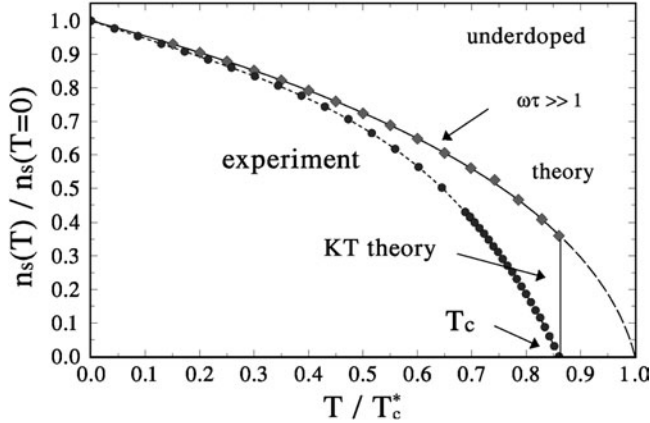

Figure 32. The phase averaged superfluid density for underdoped cuprates [6, 31]. The deviation of experimental (circles) from FLEX results is due to Cooper pair phase fluctuations with lifetime τ. Taking these into account within BKT theory (KT) one gets the results indicated by the vertical line. Note that for the dynamical superfluid density ($t \sim \omega^{-1}$) one expects $n_s(t) \longrightarrow n_s$ (FLEX) if $\omega\tau \gg 1$. (The BCS transition temperature $T_{\rm c}^*$ neglects pair phase fluctuations.)
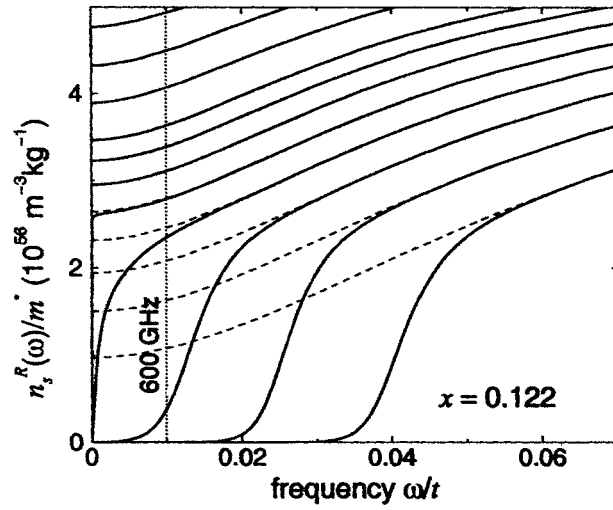
Figure 33. The dynamical phase stiffness $n_s(\omega)/m$ for the same parameters as were used in figure 32, but renormalized by vortex fluctuations. The dashed curves correspond to the unrenormalized stiffness. The vertical dotted line indicates the highest frequency used in the experiments of Corson *et al*.
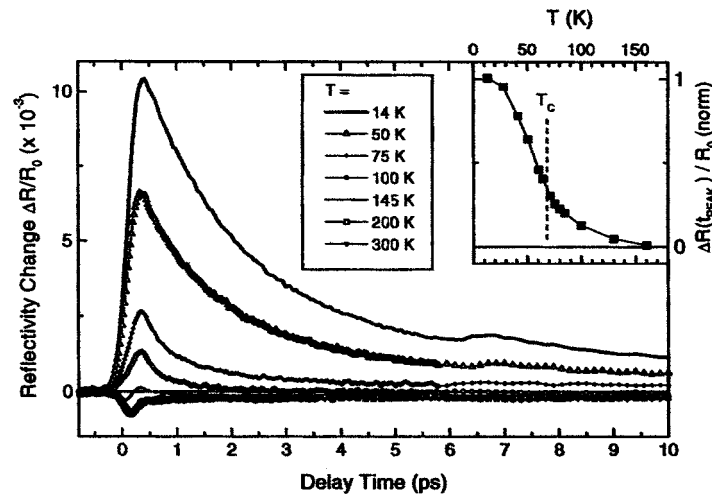

Figure 34. Transient mid-infrared reflectivity changes $\Delta R/R_0$ observed by Elsässer *et al* in underdoped $YBa_2Cu_3O_{7-\delta}$ for different sample temperatures T and the superconducting transition temperature $T_c = 68$ K. (The probe photon energy is $E_{probe} = 90$ meV.)

correlations. It is tempting to relate this time to T^*, at which antiferromagnetic correlations and pseudogap behaviour are observed ($t \sim T^{*-1}$). Further analysis must confirm this, however.

Time resolved infrared reflectivity measurements by Kaindl, Elsässer *et al* have already shed some light on the electron dynamics in high T_c cuprates [32]. Results are shown in figure 34. From this, relaxation times of the order of 1 ps may be analysed. Further such interesting experiments are needed reflecting the pseudogap and structural transition. The inset in figure 34 gives the temperature dependence of the maximum amplitude of the
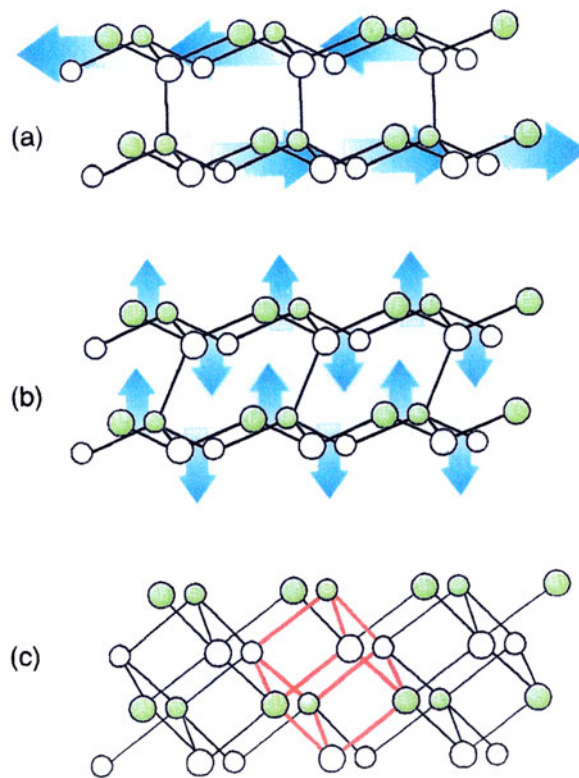
Figure 35. Dominant (a) LO and (b) TA like induced lattice distortions in covalent crystals due to hot electrons; (c) the resultant structure.

positive component in each transient, normalized to the $T = 15$ K value. A definite detailed interpretation of the results probably needs more measurements, but would be of utmost significance as regards identifying the dynamics.

3.6. Ultrafast structural changes in covalent crystals: non-thermal melting

Recently ultrafast structural changes and non-thermal melting during a time of the order of several hundred femtoseconds have been studied and observed. In covalent crystals such as Si, Ge, GaAs, the electronic excitations directly affect the bonding and this causes an ultrafast structural response (to transitions $\text{sp}^3 \rightarrow \text{s, p}$) ranging from about 10 fs to a few hundred femtoseconds.

Theoretically this was first analysed by Stampfli *et al* [2, 3] and then with an improved theory by Garcia *et al* [4, 1]. Particularly interesting problems are the details of the *non-thermal melting* of diamond, *graphitization of diamond*, *ablation* of covalent crystals, *non-thermal transition of graphite to diamond* and optically controlled reversible transitions: *crystalline* ↔ *amorphous*, for example [1]. Using the theory of Stampfli and Bennemann described in section 2, we obtain results for the time dependent response of the Si, Ge, C and GaAs structures to the electron–hole pair plasma created by an intense laser pulse, shown in the following figures. As a control parameter for the structural changes we use the fraction ξ of hot electrons. We allow for longitudinal optical phonon like distortions δ_{LO} and transverse acoustic phonon like distortions δ_{TA} which are expected to be the dominant ones, in accordance with $\Delta V \approx 0$; see figure 35 for illustration of these distortions.

Note that one observes for GaAs a change towards centrosymmetry as a response to hot electrons and this supports our assumptions on the essential distortions [33].
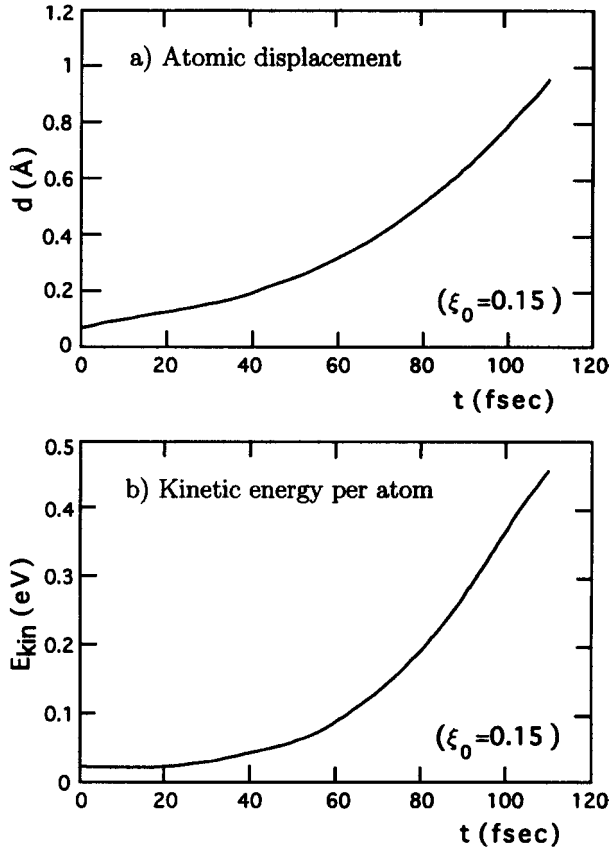
Figure 36. Results for (a) displacements and (b) the atomic kinetic energy of Si with a fraction ξ of excited electrons causing lattice instability ($\xi_0 = \xi(\delta_i = 0)$).

In figure 36 we show how for a plasma characterized by $\xi_0 = 0.15$ the atomic displacement and the kinetic energy of the atoms are affected by the hot electrons ($\xi_0 = \xi(\delta_i = 0)$).

These results are very revealing for the structural changes induced by hot electrons and resulting bond changes. One sees that for a time $\tau \sim 100$ fs the atomic displacements have become very large and so correspondingly has the kinetic energy of the atoms, so the lattice has melted. Of course, for a larger fraction ξ of excited electrons, melting occurs even faster. Note that Ge, C, GaAs and other covalently bonded semiconductors with diamond or zinc-blende structure will behave in the same way. Different atomic masses and bond lengths affect the timescales of the dynamics.

In figure 37 we present results obtained by Stampfli and Bennemann on the stability of the covalent crystal as a function of the (coherent?) distortions $\delta_t(t \equiv TA)$ and $\delta_l(l \equiv LO)$ due to hot electrons, electronic excitations into the conduction band. Evidently the lattice becomes unstable as the fraction ξ of excited electrons increases. For $\xi = 0.15$ the deep minimum in E_b is at $E_b \simeq -0.15$ eV and both distortions δ_t and δ_l are involved. Note that for $\delta_{LO} = 0$ we would obtain only a minimum of $E_b \simeq -0.16$ eV.

It should be noted here that it is of fundamental interest to understand in detail the special distortions involved in the structural changes due to hot electrons. Possibly these can be manipulated by the exciting laser pulse. This is already suggested by the fact that the distortions δ_{LA} and δ_{TO} dominate the non-thermal melting in Si, Ge etc. For further details see the studies by Stampfli, Bennemann on the laser induced lattice instability of silicon.
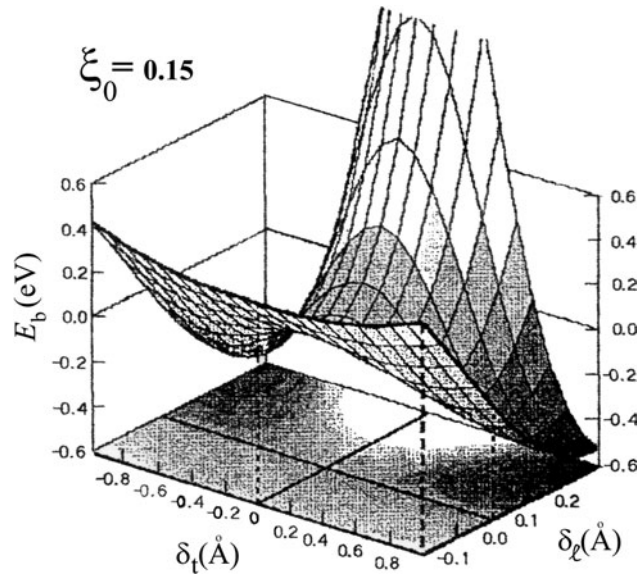
Figure 37. The dependence of the binding energy E_b of Si on the atomic displacements δ_t and δ_l caused by a fraction ξ of excited electrons ($\xi_0 = \xi(\delta_i = 0)$).
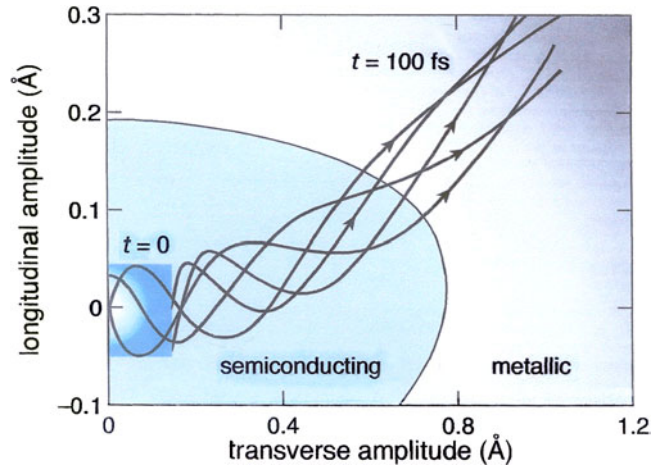

Figure 38. Results obtained by Stampfli and Bennemann for the dependence of the semiconducting and metallic phase ($\Delta = 0$) on distortions δ_{TA}, δ_{LO} due to hot electrons (ξ gives the fraction of excited valence electrons) are shown.

In figure 38 we summarize our results for the induced distortions due to hot electrons. The phase diagram is obtained by calculating the disappearance of the gap Δ_b. Some trajectories $\mathbf{r} = \mathbf{r}(\xi, t, \delta_{LO}, \delta_{TA})$ are shown. Several experiments seem to support these results [34–36]. Indeed, such an ultrafast transition from semiconducting to metallic behaviour has been observed [37]. The timescale depends of course on ξ. The metallic state is characterized by $\Delta_b = 0$ and reached after times of the order of 100 fs.

Note that the symmetry of the semiconducting state might already change upon distortions occurring before the metallic state is obtained. In particular, x-ray analysis (x-ray absorption, XAS, EXAFS, diffraction and Bragg peaks) and SHG should show this.

In figure 38 the trajectories shown are calculated from $M \ddot{\delta_i} = -\partial/\partial\delta_i(E_b(\delta_i, T_e))$ and using slightly different phases for the initial state. The phase diagram should be typical for
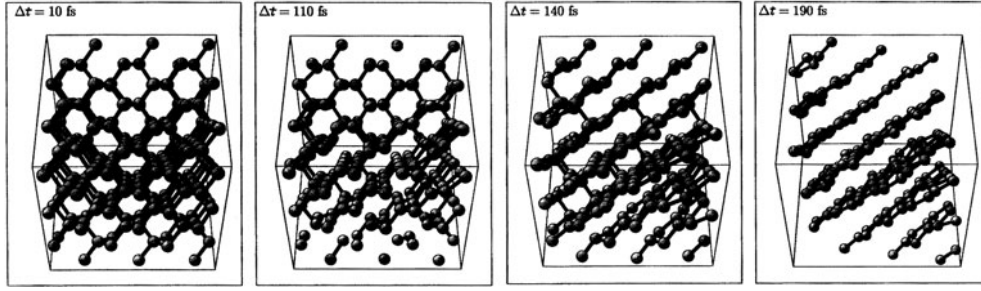
Figure 39. Non-thermal graphitization of diamond due to hot electrons. We show snapshots in the (110) direction of the ultrafast dynamics of diamond upon excitation with a laser pulse of duration $\tau = 20$ fs (Gaussian shape). The MD cell has 216 atoms. Δt is the time delay with respect to the peak of the pulse. The energy absorbed is $E_{abs} = 1.1$ eV/atom. The graphitization of diamond takes less than 100 fs.

covalent crystals and reflects general behaviour. While for conventional metals (fcc, hcp etc) hot electrons may not significantly destroy the lattice structure (symmetry), the case is different for semiconductors and ionic crystals. The electron–hole plasma may cause interesting changes of the magnetic properties for magnetic semiconductors, for ionic crystals strong emission of ions and for mixed covalent systems ($\delta_m S$, VO_2 etc) interesting ultrafast electronic transitions.

Note that the relaxation of the excited electrons should occur typically on a timescale slower than a few hundred femtoseconds. Then dephasing of the hot electrons and induced lattice distortions (coherent phonons) should occur.

Related analysis can also be applied to structural transitions such as crystalline $\rightleftarrows$ amorphous or crystalline $\rightleftarrows$ Peierls distorted lattice. Note that Peierls distortion (in Bi, $Ge_{1-x}Sb_x$ etc) is accompanied by a gap in the electron excitation. In Bi the Peierls distortion can be suppressed by pressure. As a consequence, hot electrons can then reintroduce the Peierls distortion.

For understanding the results shown in figures 36–38 one may use a Ginzburg–Landau type expression for the bond energy:

$$E_{b} \simeq \frac{\omega_{TA}^2 M}{2}(1 - a(\xi))\delta_{TA}^2 + \frac{\omega_{LO}^2 M}{2}\delta_{LO}^2 + c_1\delta_{TA}^4 + c_2\delta_{LO}^4 - \frac{b(\xi)}{2}\delta_{TA}^2\delta_{LO} + \cdots. \tag{67}$$

Here, the frequencies relate to the Γ and L points of the Brillouin zone for $\xi = 0$ and $a = b = 0$ in the absence of hot electrons ($\omega_{TA}(\xi) \simeq \sqrt{1 - a(\xi)}\omega_{TA}(0)$). Note that for $a(\xi) = 1$ the TA mode becomes soft and for $a(\xi) > 1$ the diamond structure changes to a new equilibrium structure ($c_1 \simeq$ constant > 0, $c_2 \simeq$ constant > 0). Assuming for simplicity that the phonon frequencies scale as $\omega \propto d^{-2}M^{-1/2}$ (d: bond length) we find that for a fraction of excited electrons $\xi = 0.15$ the lattice becomes unstable and melts at a time $t_m \sim 200$ fs for GaAs and at $t_m \sim 120$ fs for Si.

The anharmonic term proportional to $\delta_{TA}^2\delta_{LO}$ in equation (67) leads to additional longitudinal optical phonon like distortions.

Note that equation (67) can be extended to describe in general coherent phonons induced by hot electrons:

$$M_i \ddot{\delta}_i = -\frac{\partial}{\partial \delta_i}E_b, \qquad E_b = \sum_{\substack{m,n \\ \alpha,\beta}} a_{m,n}^{\alpha,\beta}(t)\delta_m^\alpha \delta_n^\beta. \tag{68}$$

The time dependent force constants

$$a_{m,n}^{\alpha,\beta}(t) = \frac{\partial^\alpha}{\partial \delta_m^\alpha}\frac{\partial^\beta}{\partial \delta_n^\beta}E_b \tag{69}$$
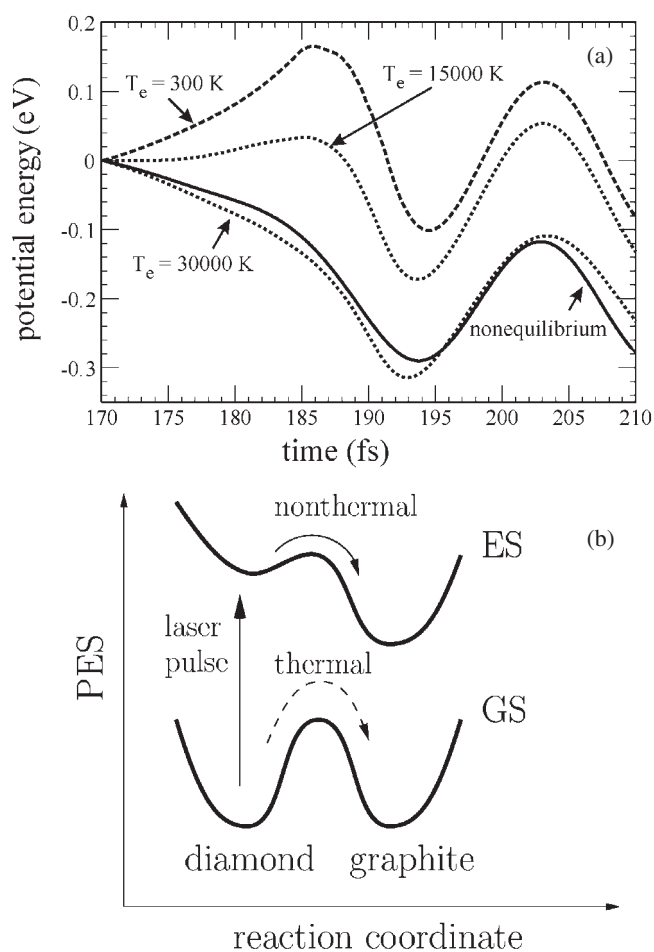
Figure 40. (a) Potential energy as a function of time upon excitation of electrons with a laser pulse of $\tau = 100$ fs and absorbed energy $E_0 = 1.3$ eV/atom (solid line). The dashed curves relate to the potential energy along the same graphitization path but calculated by assuming different electronic temperatures. For $T_e = 300$ K the energy barrier between diamond and graphite is $E_B = 0.17$ eV/atom. (b) An illustration of the mechanism for the laser induced non-equilibrium graphitization of diamond. GS and ES stand for the ground state and excited state respectively. The dashed arrow indicates graphitization occurring for thermodynamical equilibrium.

may be computed from the tight-binding or density functional theory (DFT) expression for E_b, for example. For longer times the anharmonic terms may become more and more important causing phase incoherence of the distortions.

In summary, this simplified theory for laser induced rapid heating can be applied to various problems such as the sublimation free transition from solid to liquid C, continuous switching between the insulating state and metal in thin mercury films with a gap between s and p states, the transition from amorphous solids to crystalline ones ($\omega_{TA}(\xi) \to 0$, reversible (?)), crystalline $\rightleftarrows$ Peierls distorted lattice transitions and creation of coherent phonons by hot electrons.

The theory needs modifications as discussed in section 2, in particular if the response to hot electrons involves volume changes and thus $\Delta V \neq 0$. In several papers by Garcia *et al* [4]
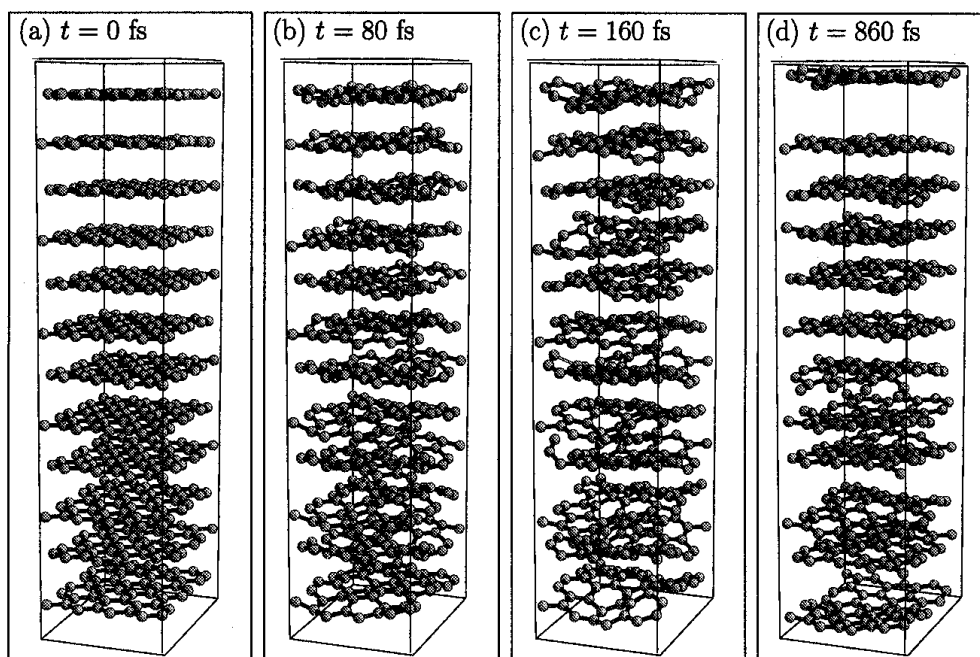
Figure 41. MD results obtained by Garcia *et al* for ablation of graphite under laser pulse irradiation. The absorbed energy amounts to $E_0 = 2.4$ eV/atom which is below the threshold for the destruction of graphite planes. The pulse duration was $\tau = 20$ fs. Apparently the laser pulse induces strong vibrations of the graphite planes which lead to the emission of the planes.

and Jeschke [1] it has been shown how one can extend the above analysis given by Stampfli and Bennemann *et al*. The following results were obtained by Garcia, Bennemann *et al* using molecular dynamics (MD) [4, 39].

In figure 39 we present interesting results on the bond changes and bond breaking: graphitization of diamond within about 100 fs. The *ultrafast graphitization* of diamond (within <100 fs) due to hot electrons [35, 36, 38, 40] arises from bond changes: $sp^3 \rightarrow_t s^2p^2$. One sees clearly the formation of graphite planes. The PES (see figure 40 for an illustration) reflects the bond changes and the non-equilibrium character of the transition.

To clarify the physics behind the ultrafast structural changes (see Jeschke, Garcia *et al* [1]), we show in figure 40 the time dependent change of the PES. Note the temperature dependence of the potential surface (T_e depends on the laser fluence) and in particular the change of the energy barrier for the non-equilibrium transition (see curve ES). This is of interest as regards the possible inverse transition graphite $\rightarrow$ diamond at non-equilibrium. Possibly special pulse forms and polarization could cause $s^2p^2 \rightarrow C^* \rightarrow sp^3$. ($C^*$ = excited C atom.) Reduced dimensions (C aggregates) could support such a transition.

In figure 41 the *ablation* of a graphite film is shown [33–37]. Note the volume expansion, the metastable liquid like state and the emission of planes; see MD calculations by Jeschke, Garcia *et al* [1].

In figure 42 we show MD results obtained by Jeschke, Garcia *et al* for the atomic oscillations induced by the hot electrons for energy absorption close to ablation. These results explain the ablation consisting of emission from the graphite plane; see [1, 4, 13].

In figure 43 we present further results obtained by Garcia *et al* using MD analysis for the interesting ablation phenomena [1]. For layered graphite structure one expects ablation
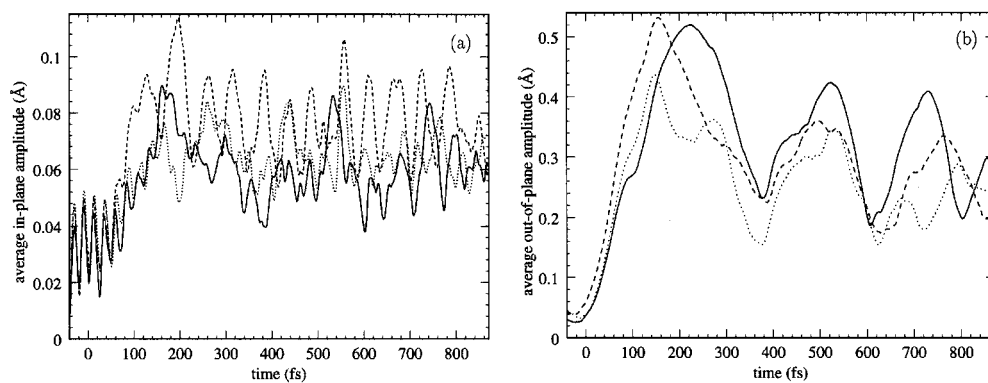
Figure 42. MD results obtained by Garcia *et al* for ablation and melting dynamics in graphite involving (a) in-plane and (b) out-of-plane oscillations of the C atoms. The results relate to various laser fluences around the ablation threshold.
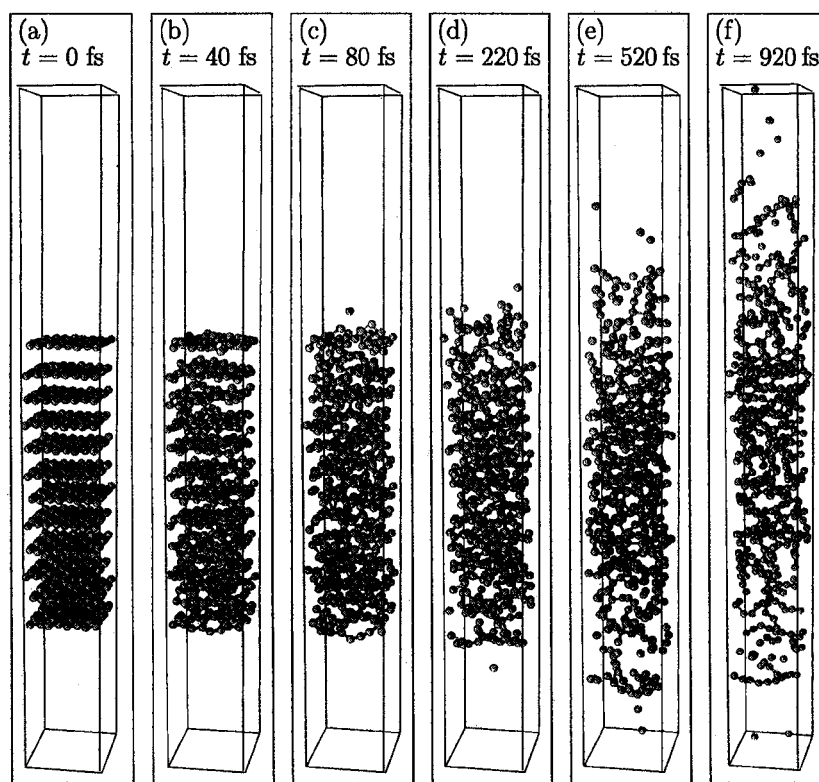

Figure 43. Ablation of a graphite film for an absorbed energy of $E_0 = 4.0$ eV/atom. The laser pulse duration was $\tau = 20$ fs. Note the strong expansion, the formation of a metastable liquid like state and the emission of carbon atoms and chains.

to consist of taking of first whole graphite plane and, for somewhat stronger laser fluences, of emission of C atoms and chains. The results show clearly the emission of whole graphite planes and also of chains and atoms.
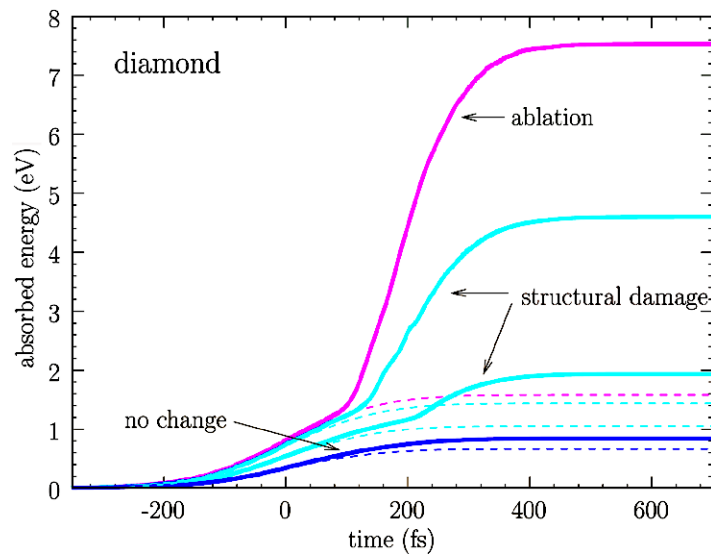
Figure 44. Time dependent absorption in diamond. The laser pulse duration is $\tau = 350$ fs. The absorption (absorbed energy per atom) obtained using MD trajectories with different final states is shown. The dashed curves correspond to the absorption that is expected if no structural changes occur.
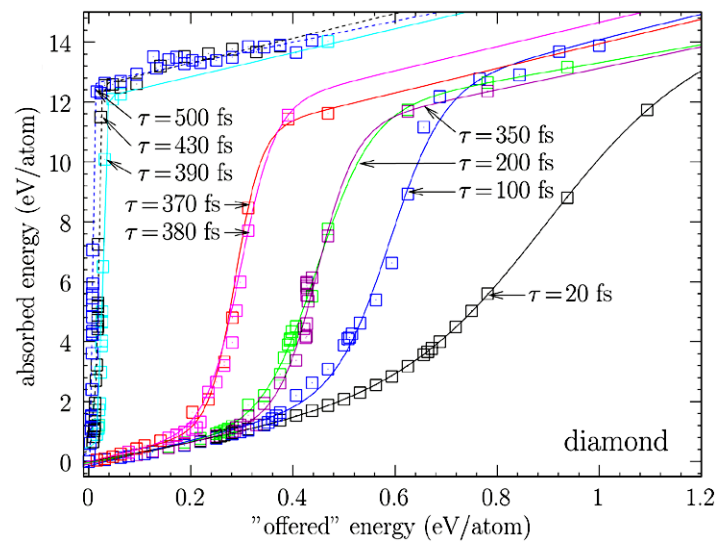

Figure 45. Absorbed energy per atom as a function of pulse intensity ('offered' energy) for diamond. The pulse duration ranges from $\tau = 20$ to 500 fs. The shape of the absorption curves and their ordering with respect to the pulse duration can be understood from the time dependent changes of the DOS. Each of the results ($\boxdot$) corresponds to a calculated trajectory.

In figure 44 MD results obtained by Jeschke, Garcia and Bennemann are shown for the ablation behaviour of diamond in strong laser fields [1]. The damage and ablation thresholds relate to the onset of irreversible lattice damage and evaporation of material (atoms), respectively.
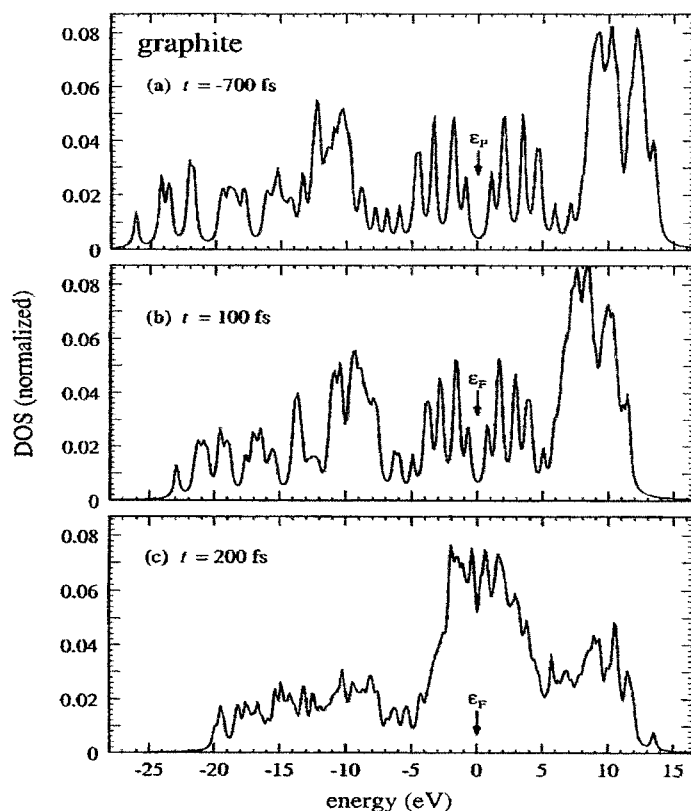
Figure 46. Densities of states for graphite at different times for a pulse duration of $\tau = 350$ fs. This figure corresponds to the trajectory with the highest absorbed energy.

One expects that, during irradiation with a longer lasting laser pulse, the structure will change continuously and thus so also will the various properties of the non-equilibrium matter such as the absorptivity [41, 42]. This is shown in figure 45 for diamond [1, 4]. Underlying this behaviour are time dependent changes of the non-equilibrium electronic structure (DOS).

In figure 46 we present results for the changing electron density of states during irradiation, which explains the absorption behaviour shown in figure 45 [1, 4]. Results are shown for graphite. Those for diamond are similar. This also sheds light on the semiconducting $\rightarrow$ metallic phase transition and the non-thermal melting [2, 3, 37].

The MD ablation results for diamond and graphite are very similar. For lower absorbed energy, bond breaking and distortions cause structural damages. These are dependent on the laser fluence: reversible or non-reversible. For larger absorbed laser energy one gets emission of material due to massive bond breaking. In the case of diamond (Si, Ge etc) the ablation consists mainly of emission of small atomic clusters and single atoms, while for layered structures such as graphite one expects actually two ablation thresholds (as calculated by Jeschke *et al*) involving emission of whole graphite planes and that of C chains and atoms. Note that the related strong increase in the ablation threshold energy as a function of time reflects bond breaking requiring some time.

In general, comparison of theory and experiment yields fairly good agreement. Of course further studies are needed for a better and more definite understanding. *XAS* investigations, *core-level shift* measurements, EXAFS—improving in particular the spatial resolution, showing local features and symmetry of the non-equilibrium behaviour—are promising [43].

3.7. Clusters in strong electric fields: Coulomb explosion

Our theory can also be used to study matter in strong electric fields; see Grigorenko [1] and Grigorenko *et al* [8] for details of the analysis. Of particular interest are systems with reduced dimension such as quantum dots and clusters where the field induced redistribution of the electrons leads to strong effects. For example, such optically induced population changes of the electronic energy can drastically change the conductance of quantum dots and molecules. Then if these are used in tunnel junctions this has interesting consequences as regards ultrafast switches. Clusters strongly irradiated by a laser pulse exhibit various fascinating phenomena (x-ray emission, highly charged and energetic ions). The following results demonstrate this.

We apply the theory described in section 2. For simplicity the cluster is treated like a 1D chain of atoms and we neglect the dependence of the hot electron binding energy on the atomic structure [1, 8]. Thus,

$$M\ddot{R}_j = -\nabla_j H_{\text{ion}}. \tag{70}$$

We use then for the ions the Hamiltonian

$$H_{\text{ion}} = \sum_{j=1}^{N} \frac{p_j^2}{2M} + \sum_{j=1}^{N-1} \sum_{k=j+1}^{N} \frac{Q_j Q_k}{\sqrt{R_{jk}^2 + a^2}} + \int U_{\text{en}} |\psi(x,t)|^2 \, dx - \sum_{j=1}^{N} Q_j R_j A(t) \sin(\omega t). \tag{71}$$

Here, we take for the coupling between the hot electrons and ions with charge Q_j and positions R_j the expression

$$U_{\text{en}} = -\sum_{j=1}^{N} \frac{Q_j}{\sqrt{(x - R_j)^2 + a^2}}. \tag{72}$$

Note that we assume for simplicity for all hot electrons the same wavefunction $\psi(x,t)$, determined by the Schrödinger equation

$$i\frac{\partial \psi(x,t)}{\partial t} = \left(-\frac{\nabla^2}{2m} + U_{\text{en}} + U_{\text{ee}} + U_{\text{xc}} + U_{\text{laser}}\right)\psi(x,t). \tag{73}$$

The Coulomb and exchange–correlation interactions are given by

$$U_{\text{ee}}(x) = \frac{1}{2}\int dx' \frac{|\psi(x',t)|^2}{\sqrt{(x-x')^2 + b^2}} \tag{74}$$

and

$$U_{\text{xc}}(x) = -\frac{3}{4}\left(\frac{3}{\pi}\right)^{1/3} |\psi(x',t)|^{2/3}. \tag{75}$$

Here, a and b are smoothing parameters adopted to avoid the singularity at $x = 0$. $A(t)$ is the envelope of the laser pulse with frequency ω.

Of course, comparison of this simplified theory with experiment must show the validity of the calculations. Physically one may expect, in strong electric fields, the electron and ion dynamics to occur essentially in the polarization direction of the laser field. Thus also all hot electrons may be describable approximately by the same wavefunction $\psi(x,t)$.

As shown in figure 47, upon laser irradiation some hot electrons get emitted within sub-picosecond times (photoemission). Of course, the fraction of emitted hot electrons will depend on the cluster size and laser field intensity.

In figure 48 results are given on the time dependence of the cluster expansion, shedding light on the emission of ions from the cluster.
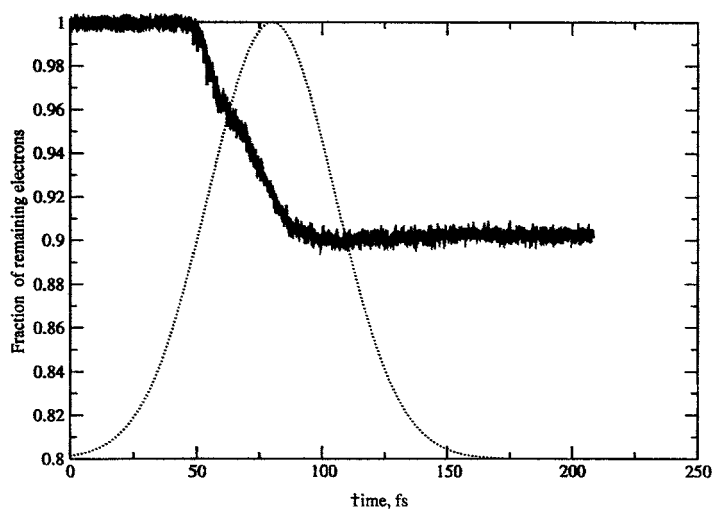
Figure 47. The time dependence of the ionization process. The fraction of the total number of electrons as a function of time in the cluster Xe_5 in the presence of a strong laser field (dashed curve). The atomic coordinates are fixed.
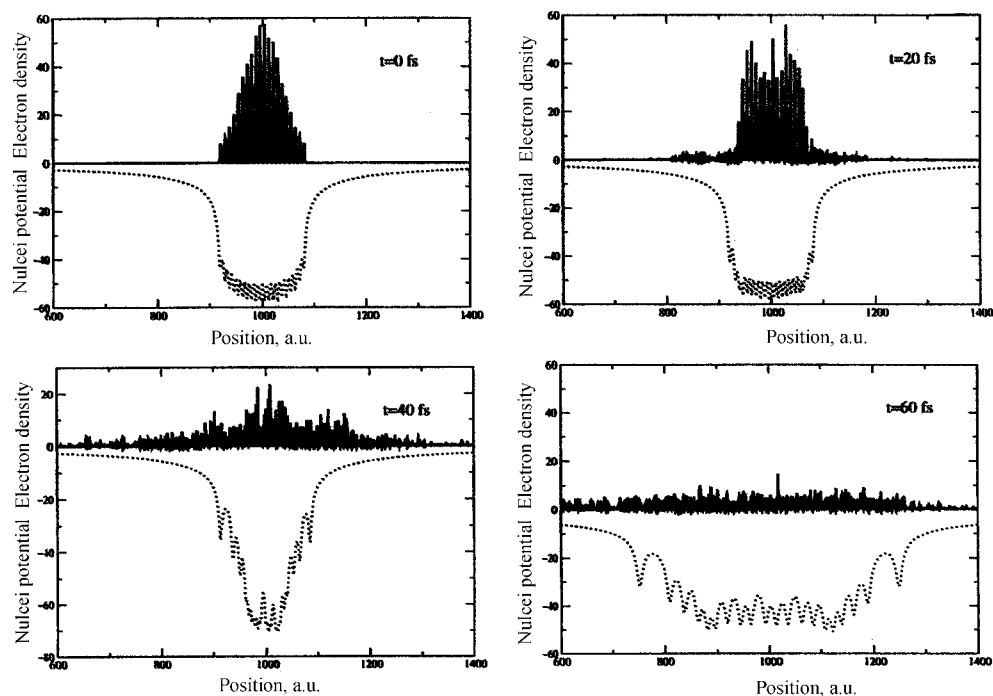

Figure 48. Snapshots of exploding Xe_2 at times $t = 0, 20, 35, 60$ fs for a laser intensity of 3.7×10^{16} W cm^{-2} and pulse duration of 80 fs. The dotted curve relates to the ionic potential. The solid curve indicates the electronic density.

Upon irradiation, the changing electron distribution causes a time dependent dipole moment $d(t)$. Results are given in figure 49. This has a strong effect on the absorption of light energy. Note the resonance like behaviour of the dipole moment $d(t)$.

For direct comparison with experiment [43] we show in figure 50 results for the kinetic energy and charge of the emitted atoms. Despite the simplified analysis one gets fair agreement with experiment (see in particular experiments by Lezius *et al* [44]). This is remarkable. As in
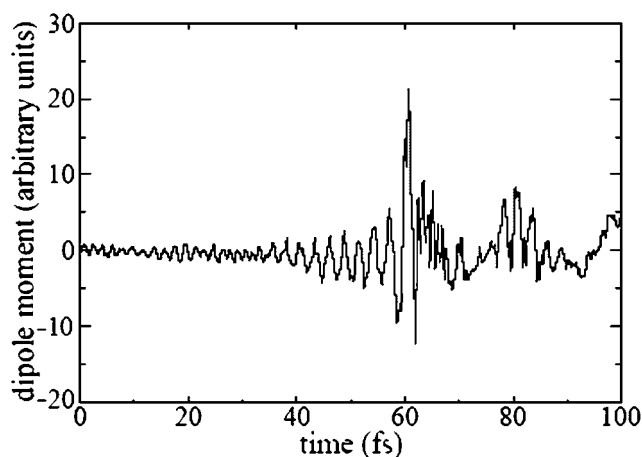
Figure 49. Oscillations of the dipole moment of a cluster with $N = 8$ atoms. Note the resonance like behaviour at a time of about 60 fs (calculations by Grigorenko *et al* [1]).
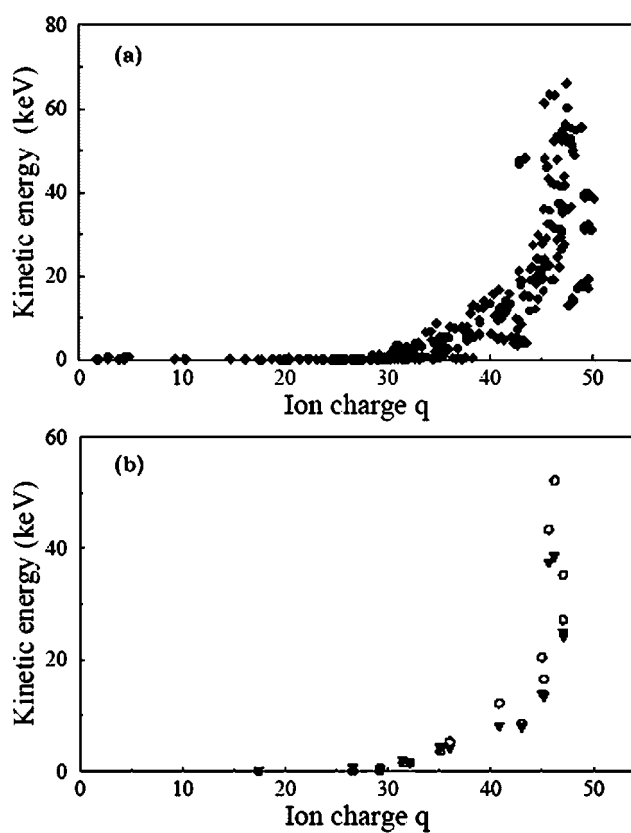

Figure 50. (a) Kinetic energy versus charge q for Xe^{q+} ions emitted upon laser excitation from a distribution of Xe_{16} clusters. (b) The results relate to a full quantum mechanical calculation (circles) and a classical one (pure Coulomb explosion) (triangles) [1]. Note the difference occurring for large q.

the case of non-thermal melting of crystals, we get an ultrafast ($\sim$10 fs) explosion of clusters. Only if the clusters are larger than a certain critical size (2–3 nm, for example) are ions with large charge emitted. One expects that first the ions at the surface of the cluster are emitted when these feel a repulsive Coulomb interaction which overcomes their binding. Our calculations show that an inhomogeneous charge distortion of the ions is present in the hot cluster; see Grigorenko *et al* [1, 45].

The results presented show characteristic features of matter at non-equilibrium. In general, the ultrafast dynamics of the hot electrons controls the subsequent changes, in particular those of the atomic structures. Of fundamental interest is clarifying how *conservation laws (such as energy and angular momentum conservation) and dimensional effects control ultrafast (femtosecond) dynamics.*

4. Summary and outlook

The discussion of solids at non-equilibrium gives an idea of how this field has advanced so far. Intense electric fields serve as a very successful tool for manipulating matter. One may change time related properties selectively. The electronic response to strong electric fields and intense laser pulses can be used to change ultrafast timescale electrical conductivity, magnetism, bonding and chemisorption, for example. This offers scope for many new applications. Depending on the strength, shape and duration of the laser pulse, physical processes can be affected and possibly controlled.

Theory and experiment need further improvements for a better and more definite understanding of non-equilibrium matter. Interesting problems are those of electronic and structural phase transitions, ablation, fragmentation such as cluster explosion and bond breaking including chemisorption bonds. In the future, further advances as regards short time laser pulses and both spatial and time resolution will be important. Thus, in particular, x-ray optics and x-ray absorption spectroscopy (XAS) will play an important role. In the following we specify some interesting problems and present results supplementing those given in section 3.

4.1. Electronic excitations

In particular, at surfaces and interfaces (of film structures, layered systems) hot electron dynamics may exhibit interesting behaviour. A laser pulse could transiently cause an occupation of surface states and with circularly polarized light one may even create a spin polarized occupation. Similarly, one could optically weaken surface bonds and break up chemisorption bonds by causing occupation of the antibonding state. Due to the interplay of the periodically acting laser field (the time between two consecutive laser pulses) and the lifetime of the excited electrons, interesting behaviour patterns will result. By changing, with the help of hot electrons, the distance between neighbouring planes of atoms at surfaces, one may create a coherent phonon (and spin excitation) mode: $d_i = d_i(t, T_e(t))$. Thus one could try to manipulate the surface reconstruction and cause structural transitions at the surface.

Also it is of interest to structure at the surface the electronic temperature,

$$T_e(t) = T_e(x, t), \tag{76}$$

resulting from hot electrons (x is the direction parallel to the surface). The structure could be created by the interference of two laser pulses, for example. The thermalization time $t_{th} \sim 10\,\text{fs}$ of the hot electrons must be such that $t_{th} < t \sim d/v_{hot}$, where v_{hot} is the velocity of the hot electrons and d the distance between neighbouring maxima of $T_e(t)$. Of interest also is a temperature profile

$$T_e(t) = T_e(z, t), \tag{77}$$

where z is the distance perpendicular to the surface ($T_e > T_{latt}$). $T_e(t)$ will decrease due to electron–lattice coupling and diffusion of hot electrons to colder regions. (Note that $v_{hot} \lesssim 1\,\text{Å fs}^{-1}$.)
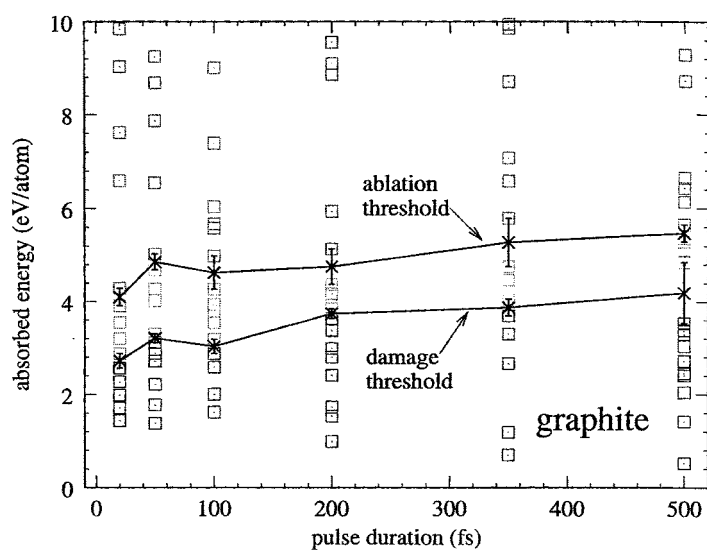
Figure 51. The ablation threshold of graphite as a function of the laser pulse duration. Each result ($\square$) in the figure corresponds to a trajectory calculated for a $N = 64$-atom MD supercell. Note that slightly below the marked ablation threshold, one finds another one at 3–4 eV/atom absorbed energy; see Jeschke *et al* [46].

One expects that, depending on the light polarization, intensity and laser pulse shape (duration, amplitude etc) structural changes, coherent phonon excitation can be manipulated in a special way. Already, the early analysis by Stampfli *et al* [2, 3] on the ultrafast response of semiconductors to hot electrons seems to indicate this; see for example figure 35 for the special modes involved dominantly in Si etc as regards non-thermal structural changes. Recent studies by Garcia *et al* using MD analysis improve on the earlier analysis [61].

4.1.1. Ablation. The interesting features of ablation discussed in the previous section reflect general behaviour. The results obtained by Jeschke, Garcia and Bennemann [1, 4] indicate clearly that lattice oscillations and bond breaking play important roles. Of particular interest are the damage and ablation thresholds. As expected, one finds in graphite for low electric field intensities and above the damage threshold that a first ablation threshold occurs for the onset of the removal of whole graphite sheets, while at the second ablation threshold (absorbed energy 4 eV/atom or more) a strong expansion and formation of a metastable liquid like state exhibiting possibly a low density liquid carbon phase occur. Then, one gets the surface emission of single atoms and carbon chains. Experiments seem to support this [46]. The high ablation threshold (high light intensity) corresponds electronically to occupation of antibonding states by the hot electrons and thus to bond breaking at ultrafast times.

It is expected that x-ray analysis, for example using XAS and diffraction (Bragg peaks) EXAFS and ESCA, will shed further light on ultrafast structural changes and the important ablation phenomena [47, 48][2].

In figure 51 results are shown for the two ablation thresholds obtained by Jeschke *et al* [1]. The results were obtained from MD calculations using a large film, a supercell of $N = 576$ atoms and constant pressure. Above the ablation threshold at absorbed energies larger than 3.3 eV/atom, fast evaporation occurs. The electron–hole plasma density is then about $\xi = 0.14$. A relatively large number of electrons are excited into antibonding states, causing bond breaking and emission of C atoms and chains. The MD results are somewhat larger than but of the order of the experimental ones.

---

[2] Similarly, time dependent EXAFS, diffraction and core-level analysis might become important diagnostic tools.
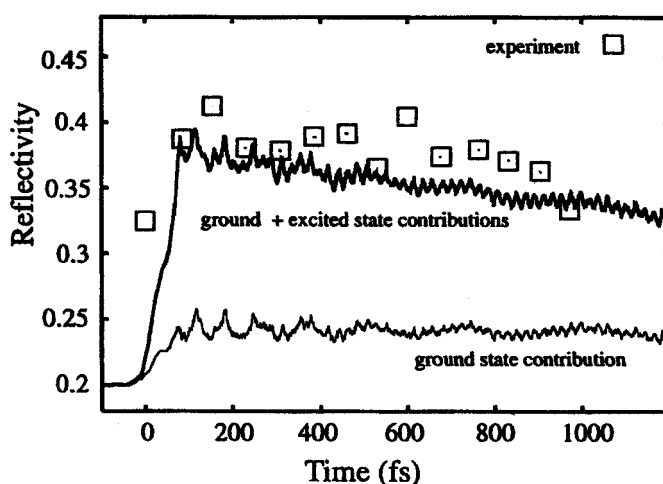
Figure 52. The time evolution of the reflectivity R for photons with $\hbar\omega = 2$ eV, after Jeschke *et al* [1]. Squares correspond to the experimental results. The thick curve was obtained by adding a metallic like term for the excited electrons to the ground state expression for the dielectric function $\epsilon(\omega, t)$. The thin curve corresponds to the ground state contribution. The laser parameters used were $\tau = 50$ fs and $E_{abs} = 1.35$ eV/atom.
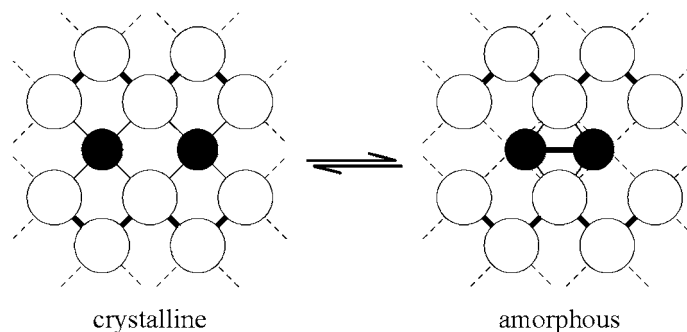

Figure 53. An illustration of a possible reversible crystalline–amorphous phase transition; see Jeschke *et al* [1]. Consider a material containing a majority of atoms A (white circles) and a minority of atoms B (black circles). Two structures are possible: atoms of B can occupy regular lattice sites of material A, or they can form small clusters such as dimers and trimers which may distort the surrounding lattice. The random orientation of such small clusters in the lattice of material A will lead to optical properties like in an amorphous phase. The difference between atomic positions in the crystalline and amorphous structure is especially small if the minority atoms B have a slightly smaller atomic radius than atoms A with the result that no very substantial relaxation of the majority component lattice occurs at the transition between the two phases.

The ultrafast response of the lattice to hot electrons involves in particular the occurrence of *coherent phonons* which eventually become phase incoherent in time due to anharmonic, large amplitude distortions of atoms. Note that in graphite special coherent phonon modes consist of shear motions of neighbouring planes or of motion changing the distance between the planes. Similarly, in general, in the covalent crystals (Si, Ge, . . .) and Peierls distorted crystals (Bi, . . .) coherent phonons result from small amplitude atomic oscillations due to electronic excitations across the band gap and modulation of the latter (for example, $\delta F_b(t) \propto a(\xi, t) + b(\xi, t)q^2 + \cdots$ where approximately $a \sim \xi(t)$, $b \sim \xi, (t)$; dephasing may result also from electron–hole recombination). Coherent phonons are expected to be particularly efficient as regards transfer
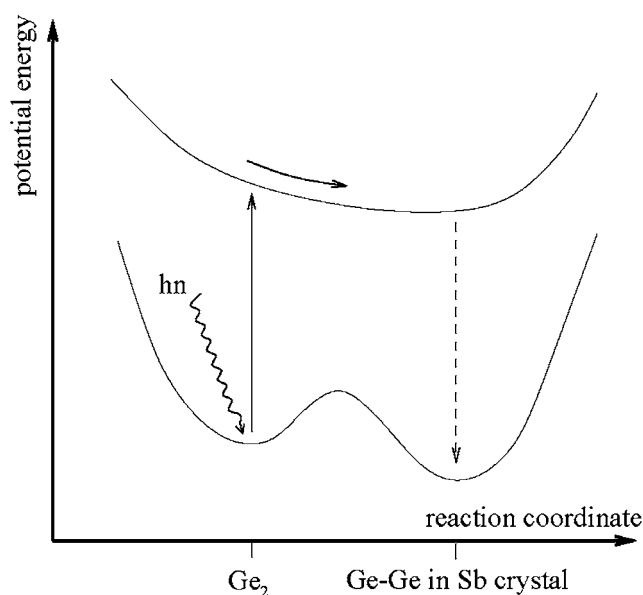
Figure 54. The model of the amorphous to crystalline phase transition in Ge_xSb_{1-x} for $0.06 < x < 0.14$. The potential energy surfaces are sketched for a reaction coordinate which includes the distance between neighbouring germanium atoms and possibly slight relaxations of the antimony lattice. In the amorphous phase the Ge atoms form dimers Ge_2 and possibly trimers Ge_3 with a bond length of $d = 2.4$ Å. An ultrashort laser pulse excites electrons into antibonding states. The excited potential energy surface has only a minimum for the Ge atoms occupying regular antimony sites (the Ge–Ge distance in the antimony lattice $d = 2.9$ Å) as this guarantees maximal distances from both Ge and Sb atoms. The de-excitation process that leads to crystalline GeSb is shown with a dashed arrow, as this relaxation process takes a long time and may be more complicated than suggested here.

of the absorbed energy from the hot electrons to the lattice. Increasing amplitude of the coherent motion leads to damage, fragmentation and ablation.

4.1.2. Reflectivity. In figure 52 interesting results on the *reflectivity* obtained within MD analysis by Jeschke *et al* [1] are shown. Evidently, both non-excited electrons and hot electrons contribute to the reflectivity. This is expected in general for all covalent crystals and other systems.

4.2. Ultrafast transitions

Important further developments would be understanding ultrafast processes leading to

(a) *optically manipulated amorphous $\rightleftarrows$ crystalline transitions* (for example, in $Ge_{1-x}Sb_x$, in Peierls distorted Bi etc);
(b) *non-thermal graphite $\rightarrow$ sp^3 bonding transitions* (for example, formation of diamond from graphite or from C clusters such as C_{60} and C nanotubes).

A possible scenario for such transitions is illustrated in the following.

In figure 53 we illustrate the transition crystalline $\Longleftrightarrow$ amorphous for Ge_xSb_{1-x} ($0.06 \leqslant x \leqslant 0.14$), as an example. This transition may be induced at non-equilibrium, e.g. optically.
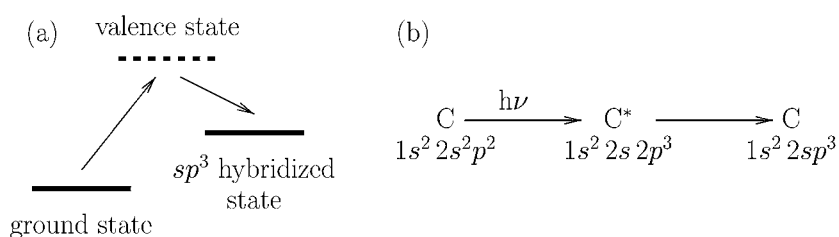
(a)   valence state   (b)
       - - - - - - -

                                            C $\xrightarrow{\text{h}\nu}$ C* $\xrightarrow{\hspace{2cm}}$ C

sp^3 hybridized $1s^2\,2s^2p^2$ $1s^2\,2s\,2p^3$ $1s^2\,2sp^3$
              state

ground state

Figure 55. Formation of sp^3 hybridized molecular orbitals via a valence state.

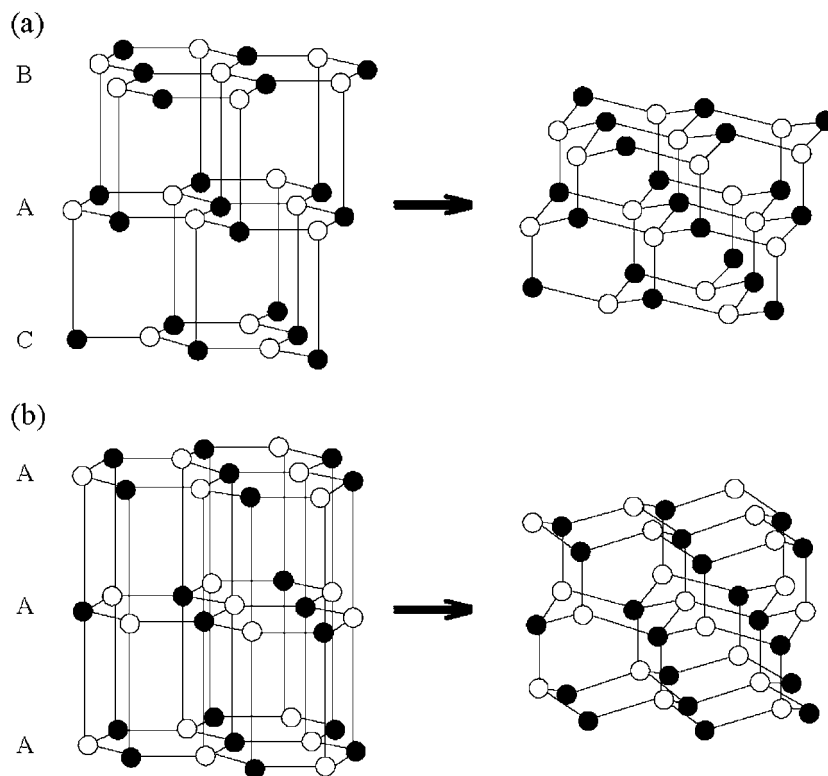**(a)**

B

A

C

(b)

A

A

A

Figure 56. An illustration of the direct transition of graphite to diamond. (a) The transition from rhombohedral graphite with ABCABC layer sequencing to cubic diamond. For this transition, white atoms move downward and black ones upward. (b) The transition from graphite with an AAA layer sequence to hexagonal diamond. For this transition, white atoms move upwards and black ones downward. The AAA sequence must first be formed from the usual hexagonal graphite with ABAB sequencing. Also, in both cases the graphite interlayer bonds in diamond are exactly as long as all other nearest neighbour bonds.

The pulse shape and fluence of the exciting laser light are expected to control the transition [1].

In figure 54 we sketch the PES of such a transition.

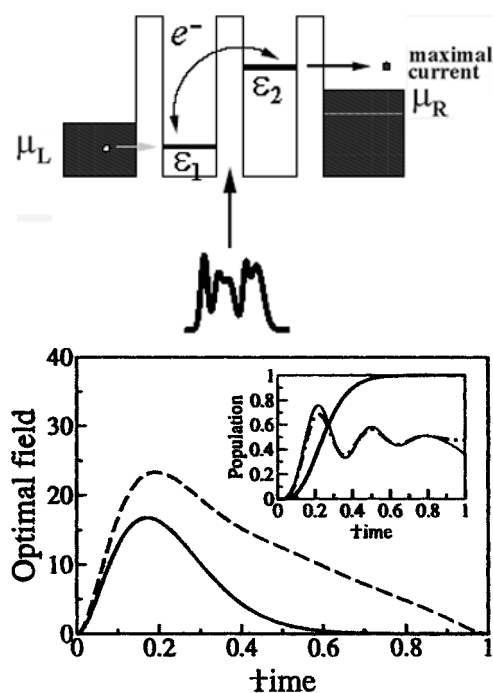In figure 55 we illustrate a possible non-equilibrium formation of sp^3 bonds from s, p states:

$$C(1s^2 2s^2 2p^2) \rightarrow C^* \rightarrow \text{diamond}.$$
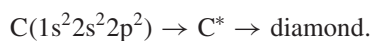
Figure 57. An illustration of an 'electron pump' device: two quantum dots providing electronic states at energies $\mathcal{E}_1$ and $\mathcal{E}_2$ coupled to contacts. Electrons can tunnel from the left contact to the left quantum dot. If the resonant electric control field is applied, the electron can jump to the right quantum dot and it can further tunnel to the right contact. The optimal control field intensity with a pulse energy $E_0 = 4.57$ for the isolated two-level system with zero relaxation (solid curve) and with relaxation $\gamma_1 = 2\gamma_2 = 5$ (dashed) with a pulse energy $E_0 = 11.15$ yielding a maximal current is also shown. A constraint on the curvature of the pulse envelope is required. Inset: the dynamics of the occupation of dot 2 ($\rho_{22}(t)$) for an isolated system (thick solid curve) and with relaxation (dash–dotted curve; the thin solid curve relates to the numerical solution of the Liouville equation).

Note that experimentally one observes graphite $\rightarrow$ melt $\rightarrow$ cooling $\rightarrow$ partial diamond formation [59]. Aggregation of C*, e.g. optically excited C atoms (C*: $1s^2 2s^2 2p^3$), for example present in DC glow discharge, could lead to diamond clusters and subsequent diamond growth [60].

As regards diamond formation at non-equilibrium, our MD results for the change of the graphite layer sequencing ABAB $\cdots \rightarrow$ AAAA $\cdots$ occurring for hexagonal graphite due to an electron–hole plasma are of great interest; see figure 56 [1].

4.3. Ultrafast tunnelling

It will be very important to use optically induced electron excitations to manipulate the electron conductivity in tunnelling junctions, for example. This permits ultrafast switching phenomena. In figure 57 we illustrate an electronic switch device using quantum dots with discrete electronic energy levels $\mathcal{E}_1$ and $\mathcal{E}_2$. The electron transfer depends on the laser pulse shape and can thus be controlled; see Grigorenko, Garcia *et al* [1, 49, 50]. Turning the laser field on and off permits ultrafast conductivity switching.

In figure 58 we present results obtained by Speer, Garcia *et al* on the current flowing through a switch and electron pump (consisting of quantum dots, molecules etc).
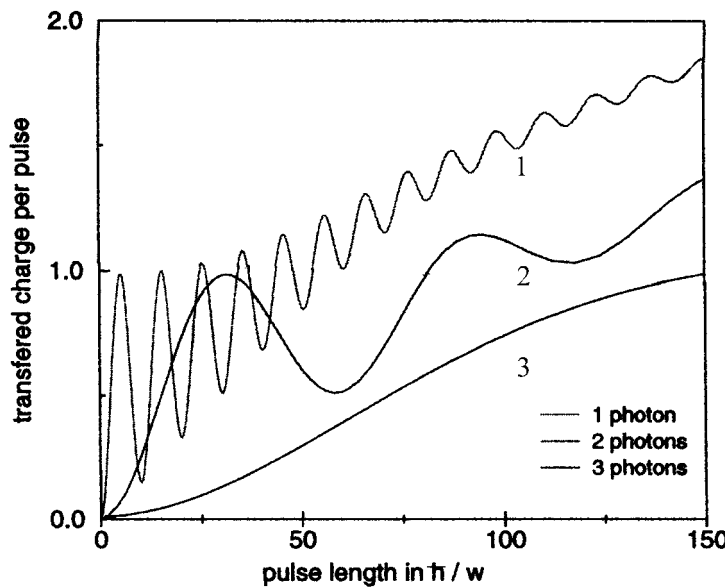
Figure 58. The dependence of the total current (charge transferred during the pulse) on the pulse length τ for different frequencies ω_1, ω_2 and ω_3 which lead to resonant tunnelling by absorption of one, two and three photons, respectively; see the calculations by Garcia *et al*. The Stückelberg oscillations, arising from the spatial Rabi oscillations between the dots during the action of the field, are clearly present for one- and multiple-photon processes. Note that for small values of τ, two photon absorption can lead to a larger current than a one-photon process. τ is given in units of $\hbar/\omega$.

Clearly, the current can be manipulated optically, depending on the pulse form. This can be formulated by a Lagrange formalism using Lagrange multipliers characterizing the optimization; see studies by Grigorenko *et al* [1].

The figure illustrates also what happens in the case of one quantum dot (or corresponding molecule) with energies $\mathcal{E}_1$ and $\mathcal{E}_2 = \mathcal{E}_1 + U n_1$, where U (the Hubbard interaction) is the effective interaction between electrons (with opposite spins σ, $\overline{\sigma}$, for example) in levels 1 and 2. Thus, for example, no electron transfer occurs from left to right if level 1 ($\mathcal{E}_1 \gtrsim \mu_L$) gets optically occupied (and $\hbar \omega < \mathcal{E}_2 - \mathcal{E}_1$), even if $\mu_R < \mu_L$, since left gate electrons must, but cannot, go to $\mathcal{E}_2$. Again, consecutive laser pulses close and open the tunnel junctions for electron transfer.

Due to the interaction of type $U_{\sigma_1 \sigma_2} n_{\sigma_2}$, circularly polarized light can be used to manipulate spin depending on the tunnelling. Note that related effects can also occur using, for optical excitations, a ferromagnet as the tunnelling medium.

The fast photon assisted tunnelling via quantum dots (or corresponding molecules, for example) calculated by Garcia *et al* [63] using $H = \sum_i \mathcal{E}_i n_i + \sum_{i,j} t_{ij} (c_i^\dagger c_j + \text{h.c.})$ demonstrates that Rabi oscillations arise from applying a short electric field pulse. The Stückelberg oscillations are responsible for the result that for certain short pulse durations (lengths), absorption of two photons induces a stronger current than results for one photon absorption. Depending on $\mathcal{E}_2 - \mathcal{E}_1$, usually of the order of about 50–200 meV, the hopping time of the tunnelling electrons can amount to 100 ps or less, requiring that the external field must last that long or longer.

4.4. Magnetic excitations as a response to hot electrons

In view of the previous discussion, it is clear that hot electrons, via affecting $T_e(t)$ and the structure $r_{ij}(t, T_e)$, may have a strong effect on various magnetic properties. Describing magnetism with the help of the Heisenberg Hamiltonian

$$H_{ex} = -\sum_{ij} J_{ij}\big(r_{ij}(t), T_e(t)\big)S_i \cdot S_j + \cdots \tag{78}$$

and the additional terms describing dipolar coupling and magnetic anisotropies [51], one obtains that the exchange coupling J_{ij} between the spins is changed in the presence of hot electrons with temperature T_e. Due to the induced structural changes, $r_{ij}^0 \to_t r_{ij}(T_e)$, the distance between the atomic planes at the surface is changed, for example, and this modulates $J_{iy} = J(r_{iy}(T_e); \ldots)$. This changes the magnitude of the spins (see the Kondo effect, formation of local moments etc) and the spin configurations and magnetization.

Consequences occur for:

(a) the magnetic reorientation transition at transition metal surfaces (for example: $S_\parallel \to S_\perp$) caused thermally via T_e—presumably the reorientation changes are controlled in time by the lifetimes of the hot electrons, electron diffusion and spin–orbit coupling ($V_{so} \lesssim J$);

(b) the easy axis dynamics (affected by T_e);

(c) surface magnetization also via occupation of spin polarized surface states—see Ni surface states;

(d) structural changes, $r_{ij}(t)$, e.g., interlayer distance changes (see oscillations in the case of graphite ablation etc), and these modulate correspondingly $J_{ij}(r_{ij}(t), T_e(t))$—this may form a coherent magnetic excitation at the surface (like the non-thermal coherent formation of phonons at semiconductor surfaces).

Of course, angular momentum conservation controls changes of $M(x, z, t)$. For transition metals and in particular rare-earth metals, $J_{ij}(r_{ij}(t), t)$ induces ultrafast magnetic responses (sub-picosecond to a few picoseconds, for example). Note that the dynamics of quantum well states in thin films is also of interest.

Similar effects due to hot electrons and $J_{ij}(r_{ij}(t), T_e(t))$, also via structural changes, occur at interfaces of films with antiparallel magnetization in neighbouring films; see figure 59 for an illustration [53]. Thus, instead of using pulsating external magnetic films one may manipulate in an ultrafast way via hot electrons the exchange fields $J_{ij}(r_{ij}(t), t)$ and thus switch the spin configuration ($\uparrow\downarrow \cdots \to \uparrow\uparrow \cdots$) and cause, like non-thermal melting, a non-thermal reversal of the surface magnetization. As in the case of optical control of electron transfer between quantum dots (see [49]), one may attempt to control optically, via the shape of the laser pulse, the precessional and (non-thermal) magnetization reversal. This tests the validity of the Landau–Lifshitz–Gilbert equation of motion and its extensions given by Bloch, Bloembergen [17, 54].

Clearly, tunnel current can be manipulated optically depending on the pulse form. This can be formulated via a Lagrange formalism using Lagrange multipliers characterizing the optimization; see studies by Grigorenko *et al* [1].

Of course, spin polarized quantum well states in film structures such as $F_1/NM/F_2$, where F_1 and F_2 are ferromagnets with parallel or antiparallel magnetization and NM is a non-magnetic film with proximity induced spin polarized quantum well states, are sensitively affected by hot electrons and $T_e(t)$; see figure 59. This is also the case for the giant magnetoresistance (GMR) structures ($F_1\uparrow/NM/F_2\downarrow$). Here, the GMR can be manipulated by the laser pulse shape and polarization again, as discussed already for other problems in this section.
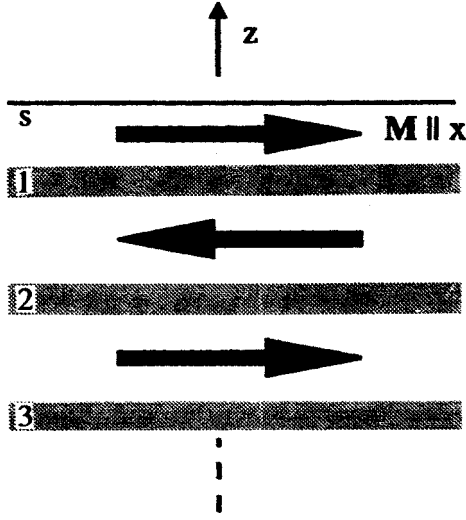
Figure 59. A succession of thin films with antiferromagnetic magnetization of neighbouring films. The shaded regions (1, 2, 3) indicate the interface area contributing to SHG. SHG results also at the surface. Approximately the first two atomic layers at the surfaces will contribute to SHG.

In summary, hot electrons with $T_e(t)$ can be used to manipulate and control the properties of various magnetic microstructures in an ultrafast non-thermal way [10, 62].

Magneto-optics (MOKE; KE: Kerr effect) and *non-linear optics* (SHG, NOLIMOKE) are very sensitive tools for analysing optically induced ultrafast changes of magnetism. Hence, it is useful to repeat briefly the SHG analysis. Note that the SHG intensity is approximately given by $I(2\omega) \simeq |\overline{\chi}|^2 \, I(\omega)$, with the effective response function

$$\overline{\chi}(M) = \sum_{ijk} F_{ijk} \chi_{ijk}(M). \tag{79}$$

In equation (79), $F_{ijk}(2\omega)$ are the non-linear Fresnel coefficients. The response functions may be decomposed as

$$\chi(M) = \chi^e(M) + \chi^o(M). \tag{80}$$

Here, χ^e is even and χ^o odd in M [10, 16]. Thus, reversals of the magnetization give (assuming for simplicity constant Fresnel coefficients)

$$I(2\omega, \pm M) \propto \{|\chi^e|^2 + |\chi^o|^2 \pm 2\,|\chi^e|\,|\chi^o|\cos\phi\}|\,\mathcal{E}|^2. \tag{81}$$

Here, ϕ in the phase difference between χ^e and χ^o [55, 10, 11], since $\chi = |\chi|e^{i\phi}$. The magnetic asymmetry

$$\Delta I(t) = \frac{I^+(M) - I^-(-M)}{I^+(M) + I^-(-M)} = \frac{|\chi^e||\chi^o|}{1 + (|\chi^e||\chi^o|)^2}\cos\phi \tag{82}$$

reflects sensitively the time dependent magnetism caused by the hot electrons.

Clearly, the tensor χ_{ijk} needs be specified in accordance with the polarizations of the electric field $\mathcal{E}(\omega, t)$ which induce the polarization

$$P_i(2\omega, t) = \sum_{jk} F_{ijk} \chi_{ijk} \mathcal{E}_j \mathcal{E}_k. \tag{83}$$

Note that $\chi^o \propto M(T_e)$ and thus becomes zero as $M \to 0$, for example, due to increasing T_e ($\chi^o(M = 0) = 0$: $\Delta I = 0$).

The Kerr angle ϕ_K also involves $\chi^o_{ijk}(M(t))$ and will reflect, as well as hysteresis loops, $M(T_e(t)) \to 0$ due to hot electrons:

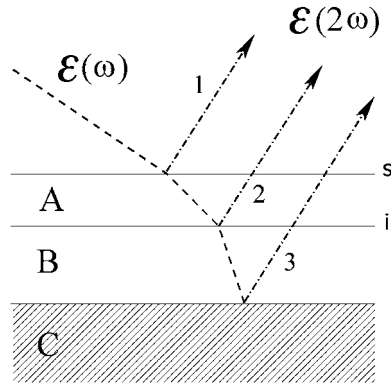$$\phi_K(M) \underset{t}{\to} 0, \qquad M(t) \to 0.$$

Figure 60. An illustration of the interference effects in SHG due to $I(2\omega) \propto |\mathcal{E}_1(2\omega) + \mathcal{E}_2(2\omega) + \mathcal{E}_3(2\omega)|^2$ from the interfaces of a magnetic film structure A/B/C. $I(2\omega)$ reflects magnetism very sensitively, in particular spin-split quantum well states.

The contribution to the SHG intensity $I(2\omega)$ due to spin-split populated surface states will also reflect $M_s(T_e) \to 0$ due to $T_e(t)$ and disappear. (Note that the induced electric field is $\mathcal{E}(2\omega) = \mathcal{E}_s + \Delta\mathcal{E}$, where $\mathcal{E}_s$ relates to the surface SHG and $\Delta\mathcal{E}$ to that resulting from the surface state. In Ni, for example, the surface states are at 2.8 and 2.6 eV away from the majority and minority spin bands.) The interference of $\mathcal{E}_s(2\omega, M_s)$ and $\Delta\mathcal{E}(2\omega, M_s)$ should also depend sensitively on the optical configuration (polar, longitudinal, transverse [10]), the angle of the incident light etc.

The particular sensitivity resulting from such interferences is also expected for SHG from magnetic film structures A/B/C (magnetic trilayer); see figure 60 for an illustration. Depending on the magnetizations M_A, M_B and M_C and $T_e(t)$, interesting and revealing magnetic contributions to $I(2\omega)$ can be seen; see [10, 55]. In particular, the SHG oscillations due to quantum well states (QWS) change for $M(T_e) \to 0$.

As regards interferences due to SHG at the surface and at the interface A/B (see figure 60), one gets within the dipole approximation for example

$$I(2\omega, M_A, M_B, \ldots) \propto 2\sum_{ijk} |\chi_{ijk}^s(2\omega, M_A)|^2 + 2\sum_{ijk} \chi_{ijk}^s(2\omega, M_A)\chi_{ijk}^i(2\omega, M_A, M_B). \quad (84)$$

For simplicity we assume $|\chi_{ijk}^s| \approx |\chi_{ijk}|$ [55]. Here, i relates to the interface A/B.

In summary, magneto-optics (MOKE, MSHG, NOLIMOKE) is well suited for studying non-equilibrium magnetism [62]. In particular, MSHG also reveals sensitively symmetric changes of the magnetization $M(t)$; consider for example the magnetic reorientation transition analysed in the polar or longitudinal optical configuration [10].

4.5. Ultrafast dynamics of excited clusters

As is already obvious from the ionization behaviour of clusters in strong electric fields, ultrafast (femtosecond time range) phenomena of small systems and clusters are of basic interest and supplement our understanding of hot matter and coupling to electromagnetic fields. The dynamics of clusters also helps us to understand that of nanostructures. Different responses of van der Waals and covalently bonded clusters reveal interesting short time dynamics of chemical bonds and of ionization potentials, core-level shifts and dynamics of quantum dots. The interplay between fragmentation and melting is of quite general interest [56].
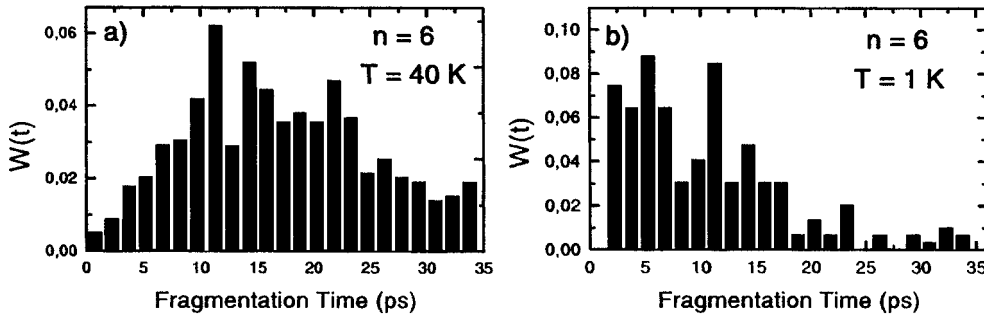
Figure 61. The calculated fragmentation time distribution $W(t)$ for Hg_6^+ clusters at $T = 40$ K before ionization. Note that $W(t)$ represents the probability of fragmentation per unit time [64].

Of particular interest is the dynamics after ionization. The time resolved fragmentation exhibits interesting behaviour reflecting bonding, bond breaking and the phase of the cluster: non-metallic, metallic, liquid state etc. For the analysis of the dynamics of a cluster with n atoms one may use the master equation

$$\frac{dN_n}{dt} = W(t)N_n(t) + \cdots,$$ (85)

where $W(t)$ is the time dependent reaction 'constant' (yielding time dependent non-ergodic dynamics). $W(t)$ is the distribution function and gives the number of clusters which fragment at time t after ionization. Then one may calculate the mean fragmentation time:

$$\tau_F = \int_0^\infty dt \, t \, W(t).$$ (86)

From this one gets by comparison with the (root mean square (rms)) bond length fluctuation (δ) the result

$$\delta \sim \tau_F^{-1}.$$ (87)

One finds as expected that fragmentation occurs only after a certain thermalization process has occurred in the cluster and that it consists mainly of emission of neutral atoms. The timescales depend on cluster size, bond character, temperature. Note that for small times and ultrafast responses one may test also the validity of thermodynamical concepts etc. The distribution function $W(t)$ is calculated using MD and the theory described in section 2.

In the following we show some typical results obtained by Garcia, Bennemann *et al* using the same type of theory as discussed in section 2.

First, van der Waals bonded small Hg_n clusters ($n \lesssim 13$) fragment within ps after exciting electrons to a Rydberg state [57], while larger covalently bonded Hg_n do not fragment after single ionization [8, 58]. In figures 61 and 62 results on Hg_n are shown [8], which compare well with experimental results.

In figure 61 we show a typical fragmentation time distribution $W(t)$. For each member of the cluster ensemble we made calculations using MD analysis fragmentation after ionization; see Garcia [63]. Depending on the form of $W(t)$ versus the fragmentation time t of the clusters, we can get interesting non-ergodic behaviour.

In figure 62 we demonstrate that the average (inverse) fragmentation time τ_F can be related to the solid $\rightarrow$ liquid transition. Actually our results yield $\delta(t) \propto \tau_F^{-1}(t)$, an interesting relationship. The cluster dynamics is in general sensitive to structure (isomerization). Fragmentation occurs after some time required by the time needed for thermalization.
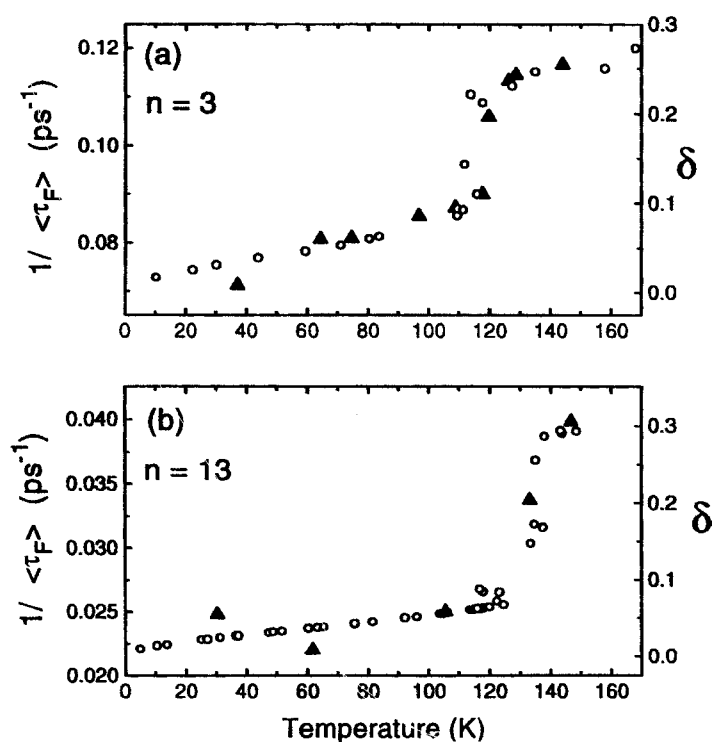
Figure 62. The temperature dependence of the inverse average fragmentation times $\langle\tau_F\rangle^{-1}$ calculated by Garcia *et al* [63] for (a) Hg_3^+ and (b) Hg_{13}^+ clusters ('up' triangles, left axis) and rms bond length fluctuations (open circles, right axis) δ before ionization. Note that the increase in $\langle\tau_F\rangle^{-1}$ characterizes the melting temperature.
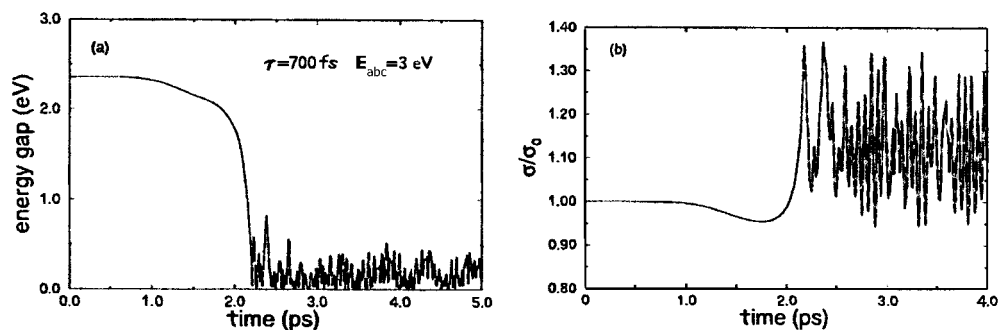

Figure 63. Metallization of Si_n clusters. (a) The time evolution of the energy gap of Si_5 for laser parameters ($E_{abs} = 3$ eV, $\tau = 700$ fs) inducing a stable structural change. When the transition to the new isomer occurs, the gap decreases strongly. (b) The relative Kubo conductivity σ of Si_5 as a function of time for the same pulse parameters as above. σ_0 is the conductivity of the cluster in the ground state. Since the isomerization is volume conserving, the decrease of the energy gap corresponds to a 'true' increase in metallic character; see [56].

In figure 63 we show MD results obtained by Garcia *et al* [63] on the laser induced ultrafast metallization of small Si clusters (closing of the gap between valence and conduction states).
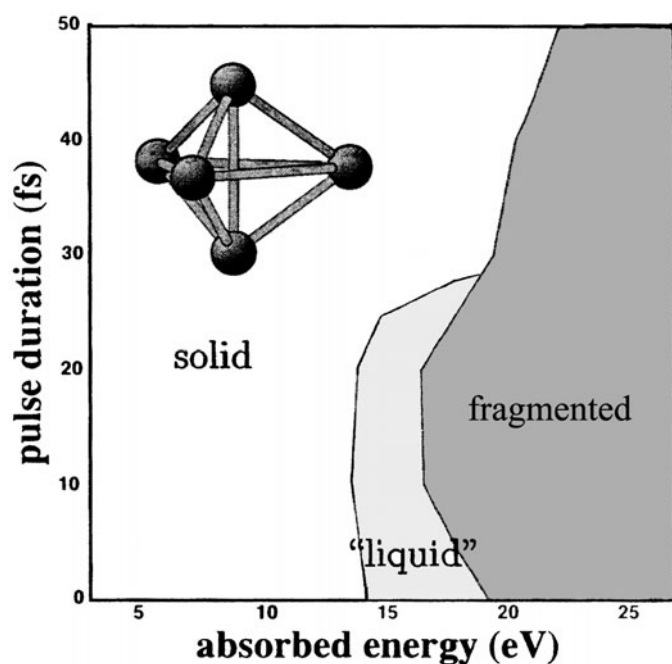
Figure 64. The generalized 'phase diagram' for the products of the laser excitation (solid like, liquid like and fragmented clusters) as a function of the pulse duration and absorbed energy for Si_5; see [56].

The MD results in figure 64 show the very interesting dependence of the non-equilibrium state on the duration τ of the exciting laser pulse. Note that for $\tau < 30$ fs one gets only a liquid like phase and for $\tau \gtrsim 30$ fs only solid $\rightarrow$ fragmentation transitions. For increasing τ, the cluster expands adiabatically. Melting occurs if the pulse duration is shorter than the cluster response time. For longer pulse duration the absorbed energy necessary for fragmentation increases, since the kinetic energy of the atoms gets lower.

The interesting interplay of fragmentation and melting is shown in figure 64 for Si clusters. The 'phase diagram' obtained for small clusters is typical for this material [56].

Figure 65 shows the power spectrum typical for larger non-equilibrium Si_n clusters. The characteristic shift in the spectrum weight to lower frequencies resulting from the electron–hole plasma created by a laser pulse is interesting. This shift can be controlled and 'optimized', for example, by choosing a corresponding laser pulse form. The theory for this has been developed by Grigorenko, Garcia, Bennemann *et al* [1, 49].

In figure 66 results are shown on the ultrafast non-equilibrium dynamics of C_{60} clusters, shedding light on their fragmentation mechanism. Note that after about 700 fs the C_{60} is torn open, with two C chains forming on opposite sides of the cluster [8, 56].

In figure 67 we present interesting results obtained by Garcia *et al* on the time dependent fragmentation of capped nanotubes (CNT). The expected emission of the caps is started by increasing the amplitudes of the corresponding excited coherent phonons [61, 64].

As regards electronic transitions, optically controlled reversibility is very interesting. This may be possible for Peierls distorted lattice structures and valency transitions (in *mixed valence systems*, SmS, V oxides etc), for example.

This completes our review of hot matter and its coupling to electric fields and the resultant ultrafast response. Such non-equilibrium physics is of great interest. One may expect that more results of definite validity due to advances as regards theory and experiment will be obtained in the future—and furthermore, of course, due to exciting new results. Presumably
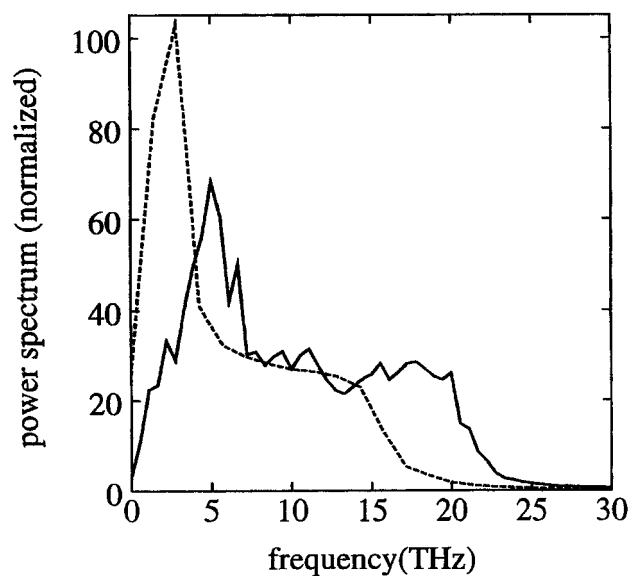
Figure 65. Power spectra of a Si$_{200}$ cluster. The continuous line corresponds to a temperature of $T = 300$ K, while the dashed line represents the spectrum of a cluster that absorbed 1.6 eV per atom during an 80 fs laser pulse. Note the shift of the weight from higher to lower frequencies as a consequence of the electron–hole plasma.
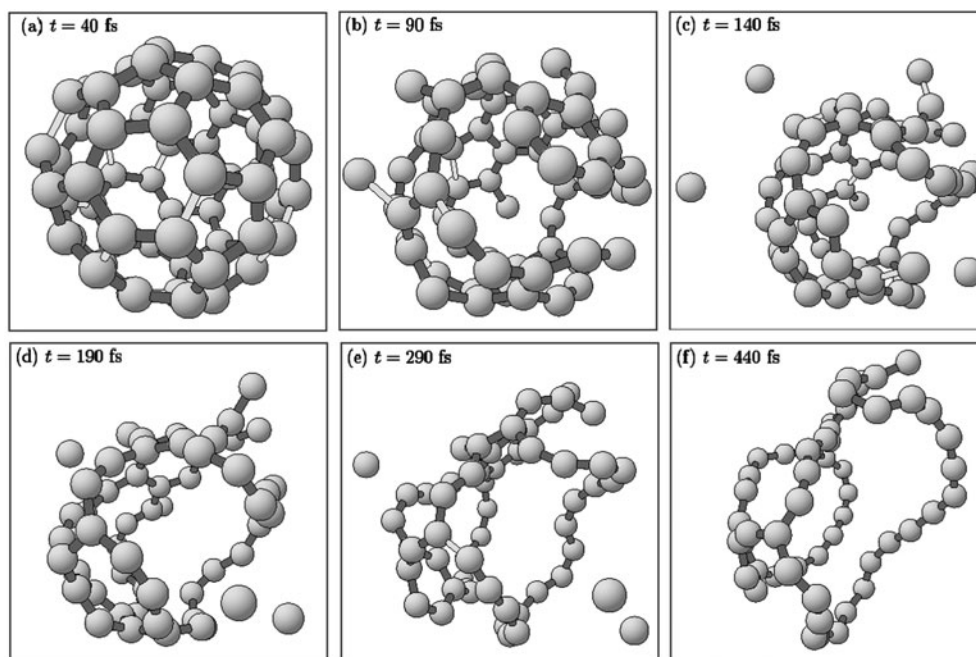

Figure 66. Fragmentation of C$_{60}$ in response to a $\tau = 80$ fs laser pulse; see Garcia. An energy of $E_0 = 3.5$ eV/atom was absorbed. While the cluster is still intact at the time $t = 40$ fs (measured with respect to the pulse maximum), at $t = 90$ fs the cage structure has already been partially destroyed. In (c) we see three ejected monomers. A coil of a linear carbon chain remains at $t = 440$ fs after the emission of a total of six carbon monomers [61, 63].

x-ray analysis, EXAFS etc will become more important. Non-equilibrium physics is reaching a better level of understanding.
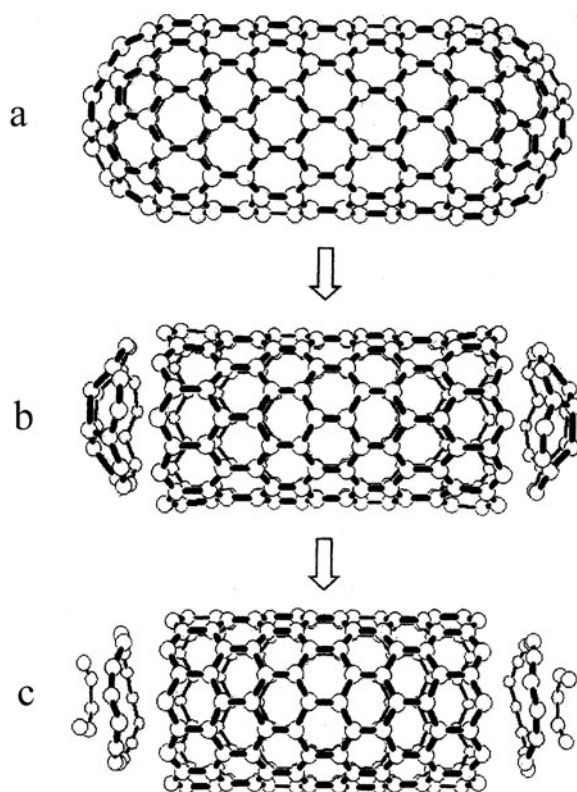
Figure 67. Time dependent ablation (fragmentation) of a (10.0) CNT; (a) 0 fs, (b) 150 fs, (c) 180 fs due to a 10 fs laser pulse and with energy 1.9 eV. The absorbed energy is 2 eV/atom (after Garcia *et al* [64]).

References

[1] Zewail A H 2000 *J. Phys. Chem.* A **104** 5660
    Callan J P 2000 *PhD Thesis* Harvard University
    Knorren R, Bouzerar G and Bennemann K H 2002 *J. Phys.: Condens. Matter* **14** R737
    Bennemann K H 1998 *Rev. Mex. Fis.* **44** 533
    Jeschke H O 2000 *PhD Thesis* Freie Universität, Berlin
    Grigorenko I 2002 *PhD Thesis* Freie Universität, Berlin
[2] Stampfli P and Bennemann K H 1990 *Phys. Rev.* B **42** 7163
    Stampfli P and Bennemann K H 1992 *Phys. Rev.* B **46** 10686
    Stampfli P and Bennemann K H 1994 *Phys. Rev.* B **49** 7299
    Bennemann K H and Stampfli P 1997 *Appl. Surf. Sci.* **109** 11
[3] Stampfli P and Bennemann K H 1995 *Appl. Phys.* A **60** 191
[4] Jeschke H O, Garcia M E and Bennemann K H 1999 *Phys. Rev.* B **60** R3701
    Jeschke H O, Garcia M E and Bennemann K H 1999 *Appl. Phys.* A **69** 49

Jeschke H O, Garcia M E and Bennemann K H 2001 *Phys. Rev. Lett.* **87** 015003

[5] Matthias E and Träger F 1968 *Appl. Phys.* A **68** 287

[6] Manske D 2002 *Habilitation Thesis* Freie Universität, Berlin
Manske D, Dahm T and Bennemann K H 2001 *Phys. Rev.* B **64** 144520

[7] Brinzanik R, Jensen P J and Bennemann K H 2003 *Phys. Rev.* B **68** 174414

[8] Grigorenko I, Bennemann K H and Garcia M E 2002 *Europhys. Lett.* **57** 39
Garcia M E, Jeschke H O, Grigorenko I and Bennemann K H 2000 *Appl. Phys.* B **71** 361

[9] Knorren R 2001 *PhD Thesis* Freie Universität, Berlin

[10] Bennemann K H 1998 *Nonlinear Optics in Metals* (Oxford: Oxford University Press)

[11] Hohlfeld J 1998 *PhD Thesis* Freie Universität, Berlin
Knorren R and Bennemann K H 1999 *Appl. Phys.* B **68** 401
Jähnke V 2000 *PhD Thesis* Freie Universität, Berlin

[12] Beaurepaire E, Merle J-C, Daunois A and Bigot J-Y 1996 *Phys. Rev. Lett.* **76** 4250

[13] Jeschke H O, Garcia M E and Bennemann K H 2002 *Appl. Phys.* **91** 1

[14] Timm C and Bennemann K H 2004 *J. Phys.: Condens. Matter* **16** 661

[15] Rasing Th 1996 *J. Magn. Soc. Japan* **20** 13
Rasing Th 1997 *J. Magn. Magn. Mater.* **175** 35
Shen Y R 1984 *Principles of Nonlinear Optics* (New York: Wiley)

[16] Pustogowa U, Hübner W and Bennemann K H 1993 *Phys. Rev.* B **48** 8607
Pustogowa U, Hübner W and Bennemann K H 1994 *Surf. Sci.* **307** 1129
Hübner W and Bennemann K H 1990 *Vacuum* **41** 514

[17] Callen H B 1958 *J. Phys. Chem. Solids* **4** 256
Gerrits T 2004 *PhD Thesis* University of Nijmegen

[18] Aeschlimann M, Bauer M and Pawlik S 1996 *Chem. Phys.* **205** 127

[19] Knorren R, Bouzerar G and Bennemann K H 2001 *Phys. Rev.* B **63** 125122

[20] Campanillo I, Pitarke J M, Rubio A, Zarate E and Echenique P M 1999 *Phys. Rev. Lett.* **83** 2230

[21] Keyling R 2002 *PhD Thesis* Freie Universität, Berlin
Keyling R, Schöne W D and Ekardt W 2000 *Phys. Rev.* B **61** 1670

[22] Aeschlimann M, Bauer M, Pawlik S, Weber W, Burgermeister R, Oberli D and Siegmann H C 1997 *Phys. Rev. Lett.* **79** 5158

[23] Knorren R, Bennemann K H, Burgermeister R and Aeschlimann M 2000 *Phys. Rev.* B **61** 9427
Aeschlimann M, Bauer M, Pawlik S, Knorren R, Bouzerar G and Bennemann K H 2000 *Appl. Phys.* A **71** 485

[24] Matthias E 1999 private communication
Hohlfeld J, Matthias E, Knorren R and Bennemann K H 1997 *Phys. Rev. Lett.* **78** 4861
Hohlfeld J, Matthias E, Knorren R and Bennemann K H 1997 *Phys. Rev. Lett.* **79** 960

[25] Rasing Th 1999 *Appl. Phys.* B **68** 477
Wieringa H A 2000 *PhD Thesis* University of Nijmegen

[26] Koopmans B and de Jonge W J M 1999 *Appl. Phys.* B **68** 1
Koopmans B and de Jonge W J M 2000 private communication

[27] Straub 2003 *PhD Thesis* University of Halle

[28] Brinzanik R 2003 *Thesis* Freie Universität, Berlin

[29] Bennemann K H and Ketterson J B 2004 *The Principles of Superconductivity* vol 2 (Berlin: Springer)

[30] Corson J, Malozzi R, Orenstein J, Eckstein J N and Bozovic I 1999 *Nature* **398** 221

[31] Timm C, Manske D and Bennemann K H 2002 *Phys. Rev.* B **66** 094515

[32] Kaindl R A 2000 *PhD Thesis* Humboldt Universität, Berlin
Kaindl R A, Woerner M, Elsässer T, Smith D C, Ryan J F, Farnan G, McCurry M and Walmsley G 2000 *Science* **287** 470

[33] Govorkov S V, Schröder T, Sumay I L and Heist P 1992 *Phys. Rev.* B **46** 6864

[34] Sokolowski-Tinten K, Schulz H, Bialowski J and van der Linde D 1991 *Appl. Phys.* A **53** 227
Sokolowski-Tinten K, Bialowski J and van der Linde D 1995 *Phys. Rev.* B **51** 14186

[35] Tom H W K, Aumiller G D and Brito-Conz C H 1988 *Phys. Rev. Lett.* **51** 1438

[36] Govorkov S V, Emelyanow V I, Korotiev N I and Shimay I L 1992 *J. Lumin.* **53** 153

[37] Saeta P, Wang J-K, Siegal Y, Bloembergen N and Mazier E 1991 *Phys. Rev. Lett.* **67** 1023
Huang L, Callan J P, Glezer E N and Mazier E 1998 *Phys. Rev. Lett.* **80** 185

[38] Preuss S and Stuke M 1995 *Appl. Phys. Lett.* **67** 338

[39] Parinello M and Rahman A 1980 *Phys. Rev. Lett.* **45** 1196
Parinello M and Rahman A 1981 *J. Appl. Phys.* **52** 7182

[40] de Vita A, Galli G, Canning A and Carr R 1996 *Nature* **379** 523

[41] Rosé-Petruck C *et al* 1999 *Nature* **398** 310
[42] Rousse A *et al* 2001 *Nature* **410** 65
[43] Lindenberg A M *et al* 2000 *Phys. Rev. Lett.* **84** 111
      Larsson J *et al* 2002 *Appl. Phys.* A **75** 467
      Reis D A *et al* 2001 *Phys. Rev. Lett.* **86** 3072
      Sokolowski-Tinten K *et al* 2001 *Phys. Rev. Lett.* **87** 225
[44] Ditmire T *et al* 1995 *Phys. Rev. Lett.* **75** 3122
      Ditmire T *et al* 1997 *Nature* **386** 54
      Ditmire T *et al* 1997 *Phys. Rev. Lett.* **78** 2732
      Ditmire T *et al* 1998 *Phys. Rev.* A **57** 369
      Springate E *et al* 2000 *Phys. Rev.* A **61** 63201
      Lezius M *et al* 1998 *Phys. Rev. Lett.* **80** 261
[45] Grigorenko I and Garcia M E 2000 *Physica* A **284** 131
      Garcia M E *et al* 2000 *Appl. Phys.* B **71** 361
[46] Sokolowski-Tinten K *et al* 1998 *Phys. Rev. Lett.* **81** 224
[47] Garcia M E, Jeschke H O and Bennemann K H 2004 at press
[48] Johnson S L *et al* 2003 *Phys. Rev. Lett.* **91** 157403
      Cavalleri A *et al* 2001 *Phys. Rev. Lett.* **87** 237401
      Sokolowski-Tinten K *et al* 2003 *Nature* **422** 287
      Glover T E *et al* 2003 *Phys. Rev. Lett.* **90** 236102
[49] Grigorenko I, Garcia M E and Bennemann K H 2002 *Phys. Rev. Lett.* **89** 233003
      Grigorenko I, Garcia M E and Bennemann K H 2002 *ISSPIC-11 (Strasbourg, 2002)*
[50] Speer O, Garcia M E and Bennemann K H 2002 *Phys. Rev.* B **62** 2630
[51] Jensen P J and Bennemann K H 1994 *Z. Phys.* D **29** 67
[52] Melnikov A, Radu I, Bovensiepen U, Krupin O, Starke K, Matthias E and Wolf M 2003 at press
[53] Ju C *et al* 1999 *Phys. Rev. Lett.* **82** 3705
[54] Gerrits Th *et al* 2002 *Nature* **418** 509
      Bauer M *et al* 2000 *Appl. Phys. Lett.* **76** 2758
[55] Luce Th and Bennemann K H 1998 *Nonlinear Optics in Metals* ed K H Bennemann (Oxford: Oxford University
      Press) p 437
[56] Garcia M E 1999 *Habilitation Thesis* Freie Universität, Berlin
[57] Baumert T *et al* 1994 *Proc. R. Netherlands Acad.* **42** 29
[58] Rademann K *et al* 1987 *Phys. Rev. Lett.* **59** 2319
[59] Mechler A *et al* 1999 *Appl. Surf.* **138** 174
[60] Efremenko I *et al* 1999 *J. Cryst. Growth* **198** 951
[61] Garcia M E, Dumitrica T and Jeschke H O 2004 *Appl. Phys.* A at press
[62] Scholl A, Baumgarten L, Jaquemm R and Eberhardt W 1997 *Phys. Rev. Lett.* **79** 5146
[63] Garcia M E 1999 *Habilitation Thesis* Freie Universität, Berlin
[64] Dumitrica T, Garcia M E, Jeschke H and Yakobsen B 2004 *Phys. Rev. Lett.* **92** 117401